

DISSERTATION

OPTIMIZATION OF THE FRONT CONTACT TO MINIMIZE SHORT-CIRCUIT CURRENT LOSSES IN
CdTe THIN-FILM SOLAR CELLS

Submitted by

Jason Michael Kephart

Department of Mechanical Engineering

In partial fulfillment of the requirements

For the Degree of Doctor of Philosophy

Colorado State University

Fort Collins, Colorado

Spring 2015

Doctoral Committee:

Advisor: W.S. Sampath

James R. Sites

John D. Williams

James M. McCamy

Copyright by Jason Michael Kephart 2015

All Rights Reserved

ABSTRACT

OPTIMIZATION OF THE FRONT CONTACT TO MINIMIZE SHORT-CIRCUIT CURRENT LOSSES IN CdTe THIN-FILM SOLAR CELLS

With a growing population and rising standard of living, the world is in need of clean sources of energy at low cost in order to meet both economic and environmental needs. Solar energy is an abundant resource which is fundamentally adequate to meet all human energy needs. Photovoltaics are an attractive way to safely convert this energy to electricity with little to no noise, moving parts, water, or arable land. Currently, thin-film photovoltaic modules based on cadmium telluride are a low-cost solution with multiple GW/year commercial production, but have lower conversion efficiency than the dominant technology, crystalline silicon. Increasing the conversion efficiency of these panels through optimization of the electronic and optical structure of the cell can further lower the cost of these modules.

The front contact of the CdTe thin-film solar cell is critical to device efficiency for three important reasons: it must transmit light to the CdTe absorber to be collected, it must form a reasonably passive interface and serve as a growth template for the CdTe, and it must allow electrons to be extracted from the CdTe. The current standard window layer material, cadmium sulfide, has a low bandgap of 2.4 eV which can block over 20% of available light from being converted to mobile charge carriers. Reducing the thickness of this layer or replacing it with a higher-bandgap material can provide a commensurate increase in device efficiency.

When the CdS window is made thinner, a degradation in electronic quality of the device is observed with a reduction in open-circuit voltage and fill factor. One commonly used method to enable a thinner optimum CdS thickness is a high-resistance transparent (HRT) layer between the transparent conducting oxide electrode and window layer. The function of this layer has not

been fully explained in the literature, and existing hypotheses center on the existence of pinholes in the window layer which are not consistent with observed results. In this work numerous HRT layers were examined beginning with an empirical optimization to create a SnO₂-based HRT which allows significantly reduced CdS thickness while maintaining diode quality. The role of this layer was explored through measurement of band alignment parameters via photoemission. These results suggest a negative correlation of work function to device open-circuit voltage, which implies that non-ideal band alignment at the front interface of CdTe is in large part responsible for the loss of electronic quality. Several scenarios explored through 1-dimensional modeling in the SCAPS program corroborate this theory.

A sputter-deposited (Mg,Zn)O layer was tested which allows for complete elimination of the CdS window layer with an increase in open-circuit voltage and near complete transmission of all above-bandgap light. An additional window layer material—sputtered, oxygenated CdS—was explored for its transparency. This material was found only to produce high efficiency devices with an effective buffer layer such as the optimized SnO₂-base HRT. The dependence of chemical, optical, electrical, and device properties on oxygen content was explored, and the stability of these devices was determined to depend largely on the minimization of copper in the device. Both sputter-deposited alloy window layers appeared to have tunable electron affinity which was critical to optimizing band alignment and therefore device efficiency. Several scenarios explored through 1-dimensional modeling in the SCAPS program corroborate this theory. Both window layers allowed an AM1.5G efficiency increase from a baseline of approximately 13% to 16%.

ACKNOWLEDGEMENTS

My parents have always nurtured my curiosity and supported my educational endeavors. Without them, it is unlikely that I would have made it this far in my education or even considered getting involved in research. I thank them first for helping me reach this point.

I would like to thank Drs. Zhixun Ma and James McCamy of PPG Industries, Inc. for providing the substrates which were the basis for much of this effort and for their deep knowledge about glass and glass coating. Their commitment to the success of the project and valuable insights made an enormous difference. I would also like to thank PPG itself for supporting my research. Funding for this research came from the Department of Energy through the Supply Chain Program and the Foundational Program to Advance Cell Efficiency. The National Science Foundation provided funding for this research through the Industry/University Collaborative Research Center for Next Generation Photovoltaics and the Accelerating Innovation Research program.

Professor Sites has been an invaluable mentor for those of us new to the sometimes-confusing world of research. Dr. Williams is a source of many creative ideas and practical knowledge which I could always count on. Professor Sampath's wealth of knowledge and experience in this area has made this contribution to the body of research possible, but I thank him most for his enthusiasm and sense of purpose, which motivated me to put the effort I did into my work. Professor Sites' students, including Russell Geisthardt, John Raguse, and Andrew Moore, have been very helpful with a variety of measurement techniques. My office mate Drew Swanson and I have shared many interesting discussions about new ideas and experimental results. Many thanks are owed to Kevan Cameron and the undergraduates who have assisted him, whose ability to keep our laboratory running smoothly allowed me to perform much of the following research.

I would finally like to thank my partner Blake. Being able to share the experience of graduate school with her has made the last several years so much happier.

TABLE OF CONTENTS

Abstract	ii
Acknowledgements	iv
List of Tables	ix
List of Figures	x
Chapter 1. Introduction	1
1.1. Solar energy overview	1
1.1.1. The need for clean energy	1
1.1.2. The potential of solar power	1
1.1.3. Photovoltaics: cost and market	3
1.2. Solar cell basics	4
1.2.1. Semiconductors	4
1.2.2. The pn junction diode	6
1.2.3. Photovoltaic energy conversion	7
1.2.4. Limits to efficiency	9
1.3. Thin-film heterostructure solar cells	11
1.3.1. Interfacial band alignment	11
1.3.2. Design of the front contact	12
Chapter 2. Device Processing and Measurement Methods	15
2.1. Thin-film deposition	15
2.1.1. Choosing a substrate	15
2.1.2. The front contact	16

2.1.3.	CdTe thin-film solar cell processing.....	16
2.1.4.	Baseline Device Processing.....	17
2.1.5.	Sputter Deposition System.....	19
2.2.	Device Measurements.....	21
Chapter 3.	High-resistance Transparent (HRT) Layers.....	24
3.1.	Introduction.....	24
3.1.1.	Thickness and coverage of window layers.....	24
3.1.2.	The role of the front contact.....	25
3.1.3.	Band alignment.....	26
3.2.	Experimental.....	26
3.3.	SnO ₂ -based HRT layers.....	27
3.3.1.	Impact of HRT layer on device performance.....	27
3.3.2.	Band Measurements of HRT layers.....	31
3.3.3.	1-D modeling of HRT layer band alignment.....	33
3.4.	ZnO and (Mg,Zn)O HRT layers.....	37
3.5.	Discussion.....	39
3.6.	Conclusion.....	42
Chapter 4.	Oxygenated Cadmium Sulfide.....	44
4.1.	Introduction.....	44
4.2.	Experimental.....	47
4.2.1.	Substrate and window layer.....	47
4.2.2.	Materials and Device Characterization.....	47
4.2.3.	Accelerated Lifetime Testing.....	48

4.3. Results	48
4.3.1. Optical Transmission	48
4.3.2. Variable-angle Spectroscopic Ellipsometry (VASE).....	50
4.3.3. Atomic Force Microscopy	53
4.3.4. Materials Characterization	55
4.3.5. Device Characterization	56
4.3.6. 1-D Device Modeling	60
4.3.7. Stability	61
4.3.8. Efficiency Verification	64
4.4. Discussion	64
4.5. Conclusion.....	67
Chapter 5. Conclusion.....	68
5.1. Evolution of front contact designs	68
5.2. Understanding of the front contact.....	68
5.3. Future Directions	70
Bibliography	72
Appendix A. Photoelectron Spectroscopy Measurements.....	84
A.1. Principle of operation.....	84
A.2. Sample preparation.....	85
A.3. Photoelectron spectroscopy measurements	87
A.4. Ultraviolet source installation	87
A.5. Data analysis	89

LIST OF TABLES

3.1	Summary of UPS measurements on various oxides	33
3.2	Modeling parameters for HRT models	34
4.1	Structural measurements from VASE	53
4.2	Modeling parameters for band offset model	61

LIST OF FIGURES

1.1	Global temperature and atmospheric carbon dioxide concentration.....	2
1.2	The existing cost of electricity compared with photovoltaics.....	4
1.3	A semiconductor band diagram.	5
1.4	Explanation of current density-voltage (J-V) plots	9
1.5	Energy and possible current from solar spectra	10
1.6	A basic band diagram of a CdTe thin-film solar cell.	12
1.7	Conduction band offsets at the front contact	14
2.1	A top-view schematic of the Advanced Research Deposition System (ARDS)	18
2.2	Small area devices made in ARDS	20
2.3	The RF sputter deposition system	22
2.4	J-V Measurement System	23
3.1	A screening experiment for HRT layers.....	28
3.2	Cell efficiency parameters vs. CdS thickness	29
3.3	Optimal cells with and without HRT	29
3.4	Behavior of FTO/CdTe device vs. illumination intensity.....	30
3.5	Work function of TCO and HRT layers vs. device properties.....	32
3.6	XES and XAS of TCO and HRT layers.....	33
3.7	Model results from varying χ of the HRT	35
3.8	Varying χ of the HRT with resistive window layer	36
3.9	Effects of interface charge at the CdTe front interface	36

3.10	Optical transmission and bandgap of (Mg,Zn)O	38
3.11	Parameters for (Mg,Zn)O devices with varying thickness and composition	39
3.12	Parameters of the best preliminary (Mg,Zn)O device	40
4.1	Optical transmission of CdS:O films	49
4.2	Ellipsometric parameters for oxygenated CdS samples	51
4.3	Refractive indices of oxygenated CdS	52
4.4	Atomic force microscopy of oxygenated CdS	54
4.5	Glancing-angle X-ray diffraction of oxygenated CdS samples	56
4.6	J-V results vs. oxygenation and window layer thickness	58
4.7	V_{OC} vs. temperature and oxygenation	59
4.8	Band and device effects of modeled conduction band offset	62
4.9	Accelerated lifetime testing of oxygenated CdS devices	63
4.10	NREL efficiency verification	65
5.1	Evolution of front contact designs	69
5.2	A roadmap for CdTe thin-film PV	71
A.1	Tools for UPS and XPS sample preparation	86
A.2	The UV source attachment to the XPS	89
A.3	Fitting of a UPS spectrum	91

CHAPTER 1

INTRODUCTION

1.1. SOLAR ENERGY OVERVIEW

1.1.1. THE NEED FOR CLEAN ENERGY. With a growing global awareness of the environmental problems associated with climate change, a growing population, and rapidly rising standards of living in many countries, the need for clean energy sources that can meet rising demand without extreme environmental degradation has become more urgent. The Intergovernmental Panel on Climate Change (IPCC) has declared it unequivocal that global temperature has warmed since the mid-20th century. It is “extremely likely” that human causes are the dominant drivers of this change, notably the emission of carbon dioxide and other greenhouse gases [1]. Figure 1.1 shows both the increase in global tropospheric temperature and the increasing concentration of carbon dioxide in the atmosphere. Risks from continued climate change include loss of land to sea level change, ocean acidification, reduced crop productivity, changes in fresh water supply, and extreme weather events such as flooding [2]. To keep the CO₂ concentration below 530 ppm, which will likely keep warming below the 2°C considered necessary to prevent major consequences, scenarios require getting approximately 50% of primary energy from low-carbon sources by 2050, and 90% by 2100 [3].

1.1.2. THE POTENTIAL OF SOLAR POWER. Solar energy is an extremely abundant, sustainable, safe, and well-distributed energy source. The amount of solar energy that reaches earth in one hour is roughly the same as what humanity uses in one year [4]. This energy can be harvested near ambient temperature with no moving parts or emissions using photovoltaics, which convert sunlight directly into electrical power. Every part of the world receives a significant amount of solar energy, with a place such as the U.S. state of Washington receiving over 60% that of New Mexico

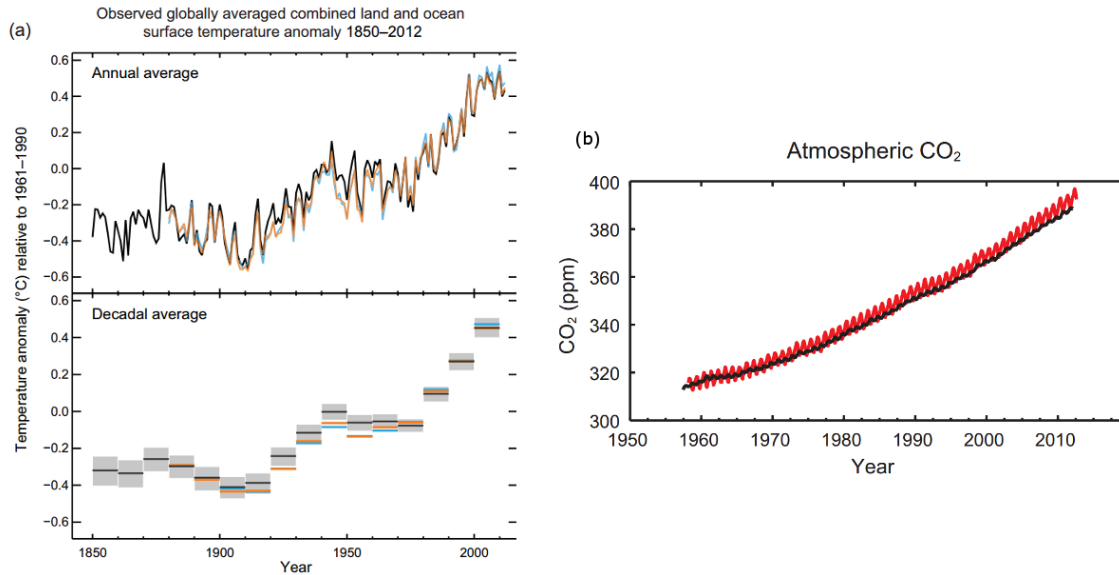


FIGURE 1.1. a) Global temperature since 1850. b) The carbon dioxide concentration in the atmosphere has risen steadily due to human activity. Reproduced from Stocker *et al.* [1].

per unit land area [4]. This distribution of energy is much more equitable than most sources of fossil energy. Water scarcity is a major development issue in many places, and the requirements for photovoltaics are minimal and much less than traditional and other low-carbon and renewable technologies [5]. Many of the best places to collect solar energy are desert lands which cannot be used for agriculture or on the rooftops of buildings, so the tradeoff between human energy and food requirements could be minimized. About 0.6% of U.S. land area covered with photovoltaics could meet all national electricity demand [6]. In short, there is no fundamental reason why humanity could not get nearly all its energy from sunlight.

One issue that makes high penetration of the electric grid by solar power more complicated is *intermittency*. Solar power obviously can only be collected when the sun is above the horizon; this follows a predictable daily pattern. Furthermore, there are seasonal variations with a minimum of energy collected in the winter and a maximum during the summer. Fixed photovoltaics are typically mounted facing south, with the tilt of the panels equal to the latitude of the location. There can also be 1-dimensional tracking systems, which move the panels from east-facing to

west facing during the day, and 2-d tracking systems which point the panels directly at the sun [7]. By following the sun across the sky, these tracking systems allow a more level collection of solar energy throughout the day rather than a pronounced peak at solar noon. Also, when skies are cloudy the amount of power which can be collected is reduced. Despite this intermittency, reaching 10-20% of electricity from photovoltaics without major changes to the grid and 50% with storage and other grid improvements is feasible [8].

1.1.3. PHOTOVOLTAICS: COST AND MARKET. Solar energy has grown rapidly in the last ten years from a niche technology to a major industry that accounts for a significant fraction of global energy installations; the global installed peak capacity of solar panels was 138 GW at the end of 2013 [9]. The price of solar power has fallen dramatically due to increasing scale of production and improvements in technology. The economic attractiveness of solar power depends on the price of electricity and the amount of solar radiation received per year; this relationship is shown in Figure 1.2. In many areas the levelized cost of energy (LCOE) of photovoltaics is lower than the price of electricity, such as northern Europe where electricity is expensive or California which receives a large amount of sun per year. As the LCOE curve in the figure continues to drop with time, more of the world will find photovoltaics economically attractive.

Cadmium telluride thin-film solar cells are an inherently low-cost technology. The lowest cost reported of manufacturing CdTe modules was \$0.53/W in 2013 [11]. Many costs associated with photovoltaic modules and power plants scale with panel area and not power output, such as module raw material costs, land, substructure, maintenance, and installation cost. For module technologies like CdTe that are less efficient than crystalline silicon, substructures to mount the panels account for up to 40% of balance-of-system costs [12]. Currently, one of the biggest drivers to further reduce module and installed system cost is to increase the power output per panel produced, i.e. the conversion efficiency [13, 14]. Based on these realities, research which focuses on improving the

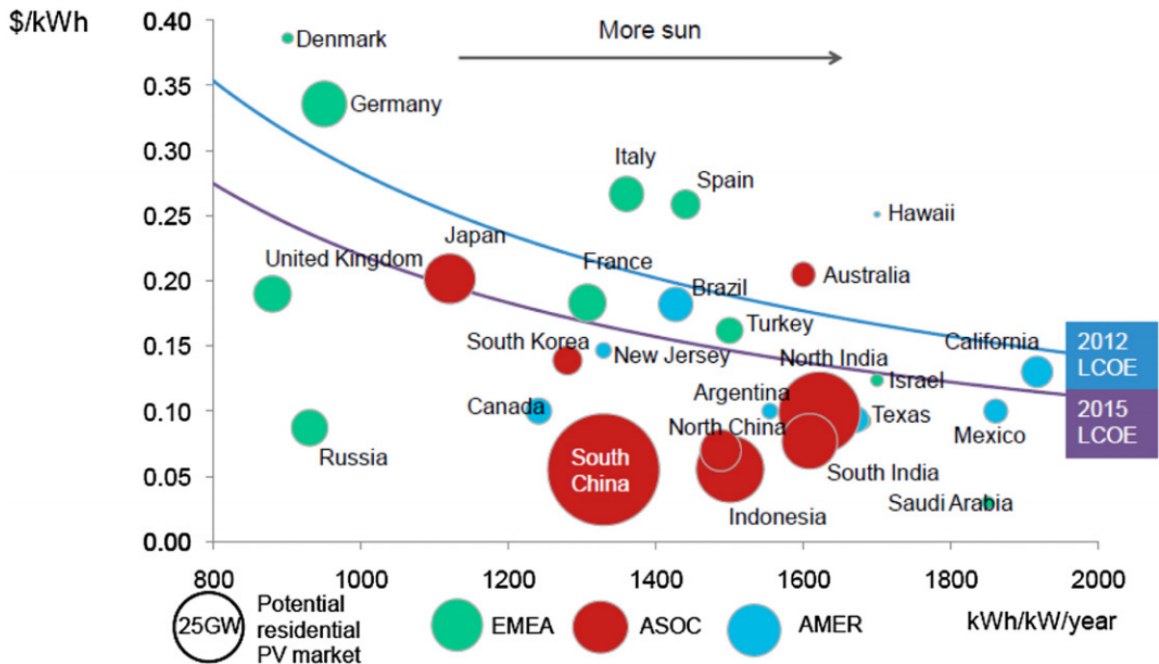


FIGURE 1.2. In areas with more sun or high electricity prices, solar is already competitive, and the decreasing levelized cost of energy (LCOE) is increasing the number of competitive regions. Reproduced from Bazilian *et al.* [10].

efficiency of existing low-cost photovoltaic technologies has the potential to continue the dramatic cost decline of photovoltaics well below that of fossil fuels.

1.2. SOLAR CELL BASICS

1.2.1. SEMICONDUCTORS. Crystalline materials have electronic *energy bands* (electron states that are closely spaced in energy and momentum) due to their repeating lattice structure. The *Fermi level* is the level of energy at which states have a 50% probability of being filled with an electron; there is not necessarily a nonzero density of states at this position. If the Fermi level is in an energy band, electrons can easily move in the material between electronic states and the material is called a metal. If the Fermi level is positioned in energy in a gap where there are no energy bands, the material is called an insulator, or a semiconductor if the gap is smaller than approximately 3 eV.

Since the states in the conduction band of a semiconductor are mostly empty, charge carriers in this band are mobile. Likewise, an empty state in the mostly full valence band is also mobile, and

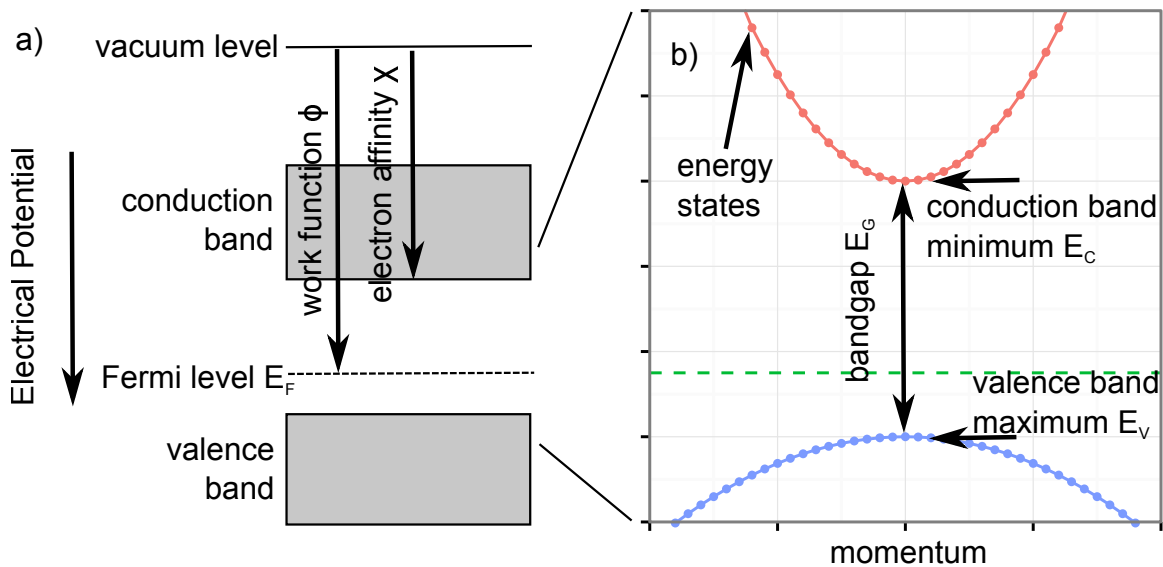


FIGURE 1.3. a) Electrons can occupy bands of energy states which are lower than the energy of an electron in free space (vacuum level). b) The separation between the highest occupied or *valence*, and lowermost unoccupied, or *conduction*, band is the *bandgap*.

can be considered a positively charged pseudo-particle called a *hole*. In thermodynamic equilibrium, the relative concentration of electrons and holes in a material is dictated by the Fermi level. The energetic distance from a state above or below the Fermi level along with the temperature of the material determines its probability of occupation; if this distance is much more than the thermal energy kT , the Boltzmann distribution can approximate the tail of the Fermi distribution. The relationship between Fermi level and carrier concentration is given by Equation 1 for an *effective density of states* N_C and N_V for the conduction and valence bands [15]. For an intrinsic semiconductor the Fermi level will be near the middle of the bandgap. Impurities, or dopants, can be added to the material to move the Fermi level by introducing localized states with energy levels in the bandgap. A *donor* state is occupied with an electron when neutral, and, when a donor state is added within a few kT of the conduction band, it can easily ionize at room temperature and add an electron to the band. An *acceptor* state is unoccupied when neutral and when added within a few kT of the valence band can easily accept an electron, creating a mobile, positively charged hole.

Shallow donors and acceptors (close to the conduction and valence bands, respectively) have the effect of moving the Fermi level up or down in the bandgap.

$$(1) \quad n = N_C \exp\left(-\frac{E_C - E_F}{kT}\right); \quad p = N_V \exp\left(\frac{E_V - E_F}{kT}\right);$$

The bandgap determines the optical absorption properties of the material since only photons with energy greater than the bandgap can excite electrons from the valence band maximum (VBM) to the conduction band minimum (CBM). In a *direct bandgap* material such as CdTe, the CBM and VBM occur at the same wavenumber value of $k = 0$ (where $\hbar k$ is momentum), whereas for an *indirect bandgap* a source of momentum transfer is required for the transition to occur. Photons have effectively no momentum, so a phonon is required. Practically, this means that the absorption coefficient just above the bandgap energy is typically much higher for direct bandgap materials, and therefore the thickness of absorber material needed to absorb almost all the light is thinner compared to indirect bandgap materials.

1.2.2. THE PN JUNCTION DIODE. When acceptor- and donor-doped materials are placed together into a pn junction, a *depletion* or *space-charge* region (SCR) is created. Since the Fermi level must be flat throughout the device in equilibrium (*i.e.*, the device is at constant temperature with no light absorption or voltage bias), electrons diffuse from the n-type material and fill the holes on the p-type side. This results in oppositely charged regions that create an electric dipole. Due to concentration gradients, there is a current of electrons from the n- to the p-type layer and holes the opposite direction. With no bias (equilibrium) this is equal to the recombination of holes and electrons and there is no net current flowing through the junction. In reverse bias the recombination tends to zero and the current asymptotically approaches the saturation current density J_0 .

In forward bias the barrier is lowered and current increases exponentially with increasing forward bias. This behavior is given by Equation 2, referred to as the diode equation. The pn junction model is appropriate for many types of solar cell such as silicon in which the diode is formed within a single material and the SCR is much thinner than the absorber, but it also provides a good basis of understanding for thin-film solar cells. The regions outside of the SCR with flat bands are called the *quasi-neutral* region (QNR) and in the absence of an electric field, transport in these regions occurs by diffusion.

$$(2) \quad J = J_0 \left[\exp\left(\frac{qV}{kT}\right) - 1 \right]$$

1.2.3. PHOTOVOLTAIC ENERGY CONVERSION. Improving solar cell performance requires understanding the loss mechanisms and separating fundamental efficiency limitations from practical non-idealities. The material quality of the solar cell absorber is critical, since the excited electron-hole pairs must be collected before the electron falls back into an empty valence band state, a process called *recombination*. Recombination can be band-to-band directly, which would occur even in a perfect material, in which case a photon is re-emitted and the recombination is called *radiative*. In Shockley-Read-Hall (SRH) recombination, energy states created by defects in the middle of the bandgap capture and emit holes and electrons; because the energy steps are smaller and phonon-mediated, recombination can occur at a much higher rate than band-to-band and therefore SRH recombination is called *non-radiative*. The more defects in a material near the center of the bandgap, and the higher the capture cross-section, the shorter the time electron-hole pairs can survive. Recombination increases the forward current of the diode (J_0), which leads to reduced efficiency in the device; details of efficiency parameters are discussed later. Other sources of electronic loss include parasitic resistances, which could be a series or shunt resistance in the electrode or films.

A photovoltaic device converts light into direct-current electrical energy. For most photovoltaic technologies the light absorber is a semiconductor; mobile charge carriers are photogenerated when a photon excites an electron in the valence band into the conduction band, creating a hole and an electron. When photo-generated carriers are created, they are ideally collected at their respective contacts; because they are separated from within the absorber rather than injected, this is considered a reverse current. A solar cell's behavior is characterized by the current that passes through the cell at each voltage, known as the current-density/voltage or J-V curve. In the dark, the solar cell exhibits diode behavior with an exponential dependence of current on voltage. When the cell is illuminated there is still an exponential increase in forward current with applied voltage, but there is also a reverse current J_L due to collection of photo-generated carriers. The rate of photo-generation depends on the intensity and spectral composition of the incoming light. If non-ideal series and shunt resistances and an ideality factor A greater than 1 are considered, the resulting J-V curve of the cell is described mathematically by Equation 3.

$$(3) \quad J = J_0 \left[\exp \left(\frac{q(V - R_{series}J)}{AkT} \right) - 1 \right] - J_L + \frac{V}{R_{shunt}}$$

The point at which these currents sum to zero is the open-circuit voltage (V_{OC}); the current density at $V = 0$ is the short-circuit current density (J_{SC}) and approximates J_L for devices of reasonable quality. The power produced by a cell at any voltage bias is the product of current and voltage. The maximum power point can be used to determine both the conversion efficiency of the cell defined in Equation 4 as well as the fill factor which is a measure of “squareness” of the curve. Key points are shown in Figure 1.4.

$$(4) \quad \eta = \frac{V_{MP} \cdot J_{MP}}{P_{in}} = \frac{V_{OC} \cdot J_{SC} \cdot FF}{P_{in}}$$

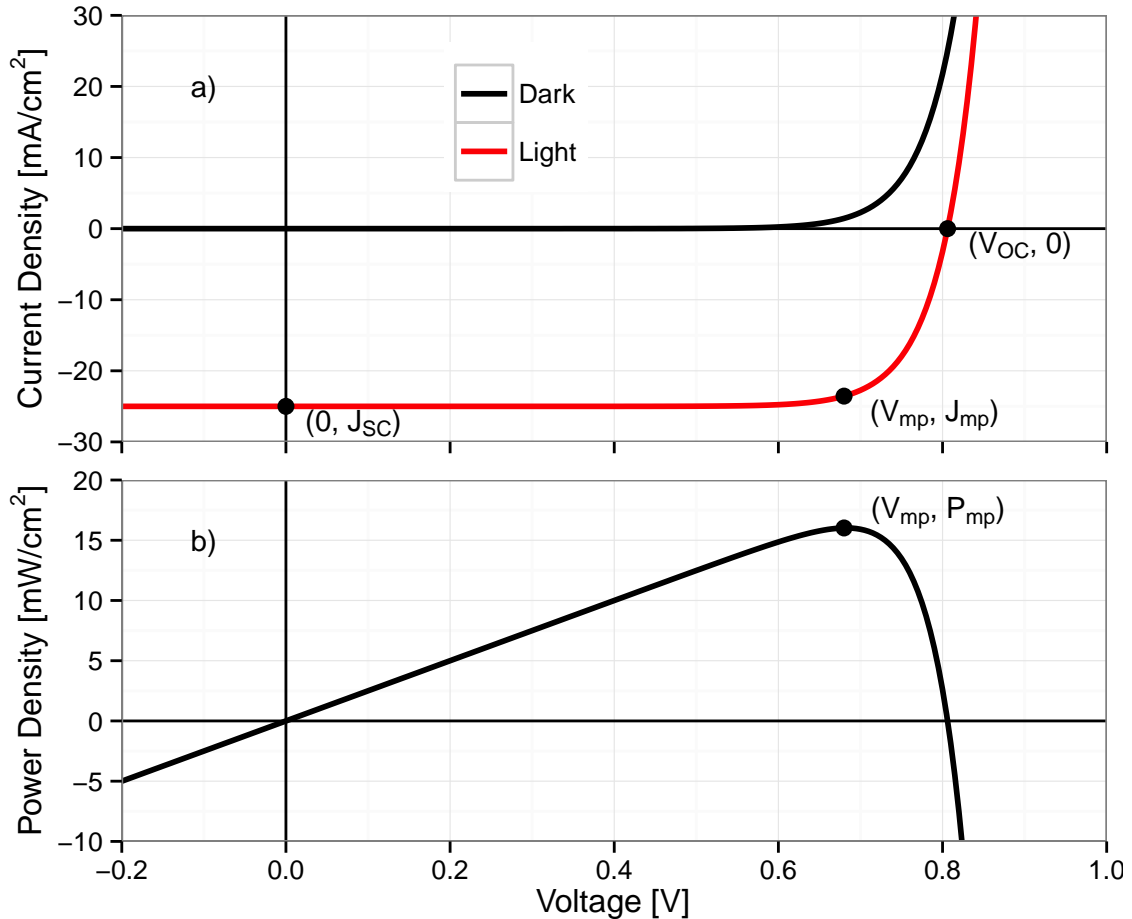


FIGURE 1.4. a) A diode turns on exponentially in the dark, and produces negative photocurrent in the light. b) The maximum power point is used to determine the fill factor and efficiency.

1.2.4. LIMITS TO EFFICIENCY. The amount of current producible by a cell is limited by (1) the bandgap of the semiconductor since only above-bandgap light is absorbed and typically only one electron-hole pair per photon can be created, and (2) the amount of light available from the defined spectrum. Several spectra are typically used; one approximates the light available to satellites in space. This is the light which travels from the sun through the vacuum of space to earth above the atmosphere and closely resembles a blackbody curve. The spectra which approximate light on earth are called AM1.5 which refers to the amount of atmosphere or “air mass” through which the light has to travel. In this air there is some absorption and scattering due to dust, water

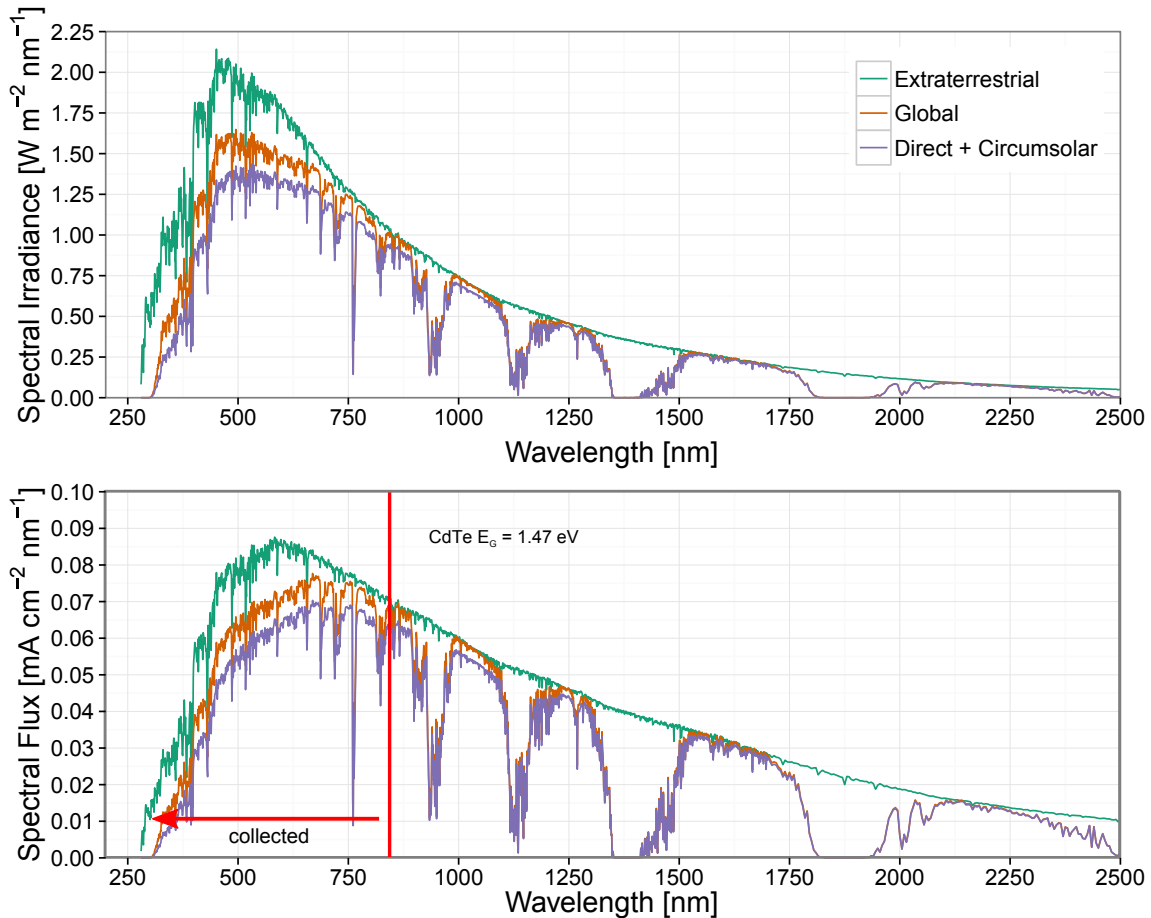


FIGURE 1.5. Various standard spectra show different spectral irradiance (top); the AM1.5 global spectrum is most relevant to photovoltaics. This can be converted to a potential amount of current generated in a solar cell (bottom) if the quantum efficiency reaches unity by integrating the spectral flux. The CdTe bandgap of 1.47 eV is shown as a red line for reference.

vapor, oxygen, etc. For concentrating devices only collimated light directly from the sun can be collected (AM1.5 Direct), but for standard PV diffuse light can also be collected; therefore, AM1.5 Global is the spectrum used for characterizing non-concentrating photovoltaics. Figure 1.5 shows the spectral irradiance, and the corresponding current that could be generated from light at a given wavelength.

An estimate of the maximum theoretical efficiency of a solar cell is given by the *Shockley-Queisser limit*. Assuming all available light is collected gives the maximum current density. The ideal forward current of the cell assumes that only radiative recombination occurs and hence the

ideality factor is 1. This can be used to calculate the open-circuit voltage and fill factor. The amount of energy that can be extracted from each charge carrier is limited by the bandgap, and electrons excited by high-energy photons above the CBM quickly fall back to the CBM in a phonon-mediated process called *thermalization*. For a single junction, the energy bandgap has a broad optimum range between about 1 and 1.5 eV [16]. A higher bandgap would fail to absorb lower-energy photons, leading to reduced conversion efficiency [17]. Common semiconductors chosen for photovoltaics include crystalline or amorphous silicon; III-V materials such as GaAs or InP; and thin-film polycrystalline materials such as Cu(In,Ga)Se₂ and CdTe; all these materials have a bandgap between 1 and 1.5 eV. The theoretical maximum efficiency for a single junction using the AM1.5G spectrum is 31.0% for an optimum bandgap of 1.3 eV [18].

1.3. THIN-FILM HETEROSTRUCTURE SOLAR CELLS

For polycrystalline thin-film solar cells, it is often desirable to build the electronic structure using multiple layers of different materials, called a *heterostructure*. A heterostructure can take advantage of the natural tendency of some materials to be p- or n-type as deposited. In CdTe solar cells, the transparent conducting oxide (TCO) and CdS are naturally n-type, while the CdTe is naturally p-type as processed. Intentionally doping these materials can be difficult due to the high degree of compensated defects in the material and high mobility of some dopant atoms [19]. Materials of different bandgap can be used to control where the light is absorbed in the cell, and electronic properties of semiconductor interfaces can be used to collect holes or electrons selectively at different contacts. Figure 1.6 shows the general structure and principle of operation of a CdTe thin-film solar cell using a band diagram.

1.3.1. INTERFACIAL BAND ALIGNMENT. The use of heterostructures can also aid in the proper *band alignment* of the front and back contact of the cells. When two semiconductors are placed in

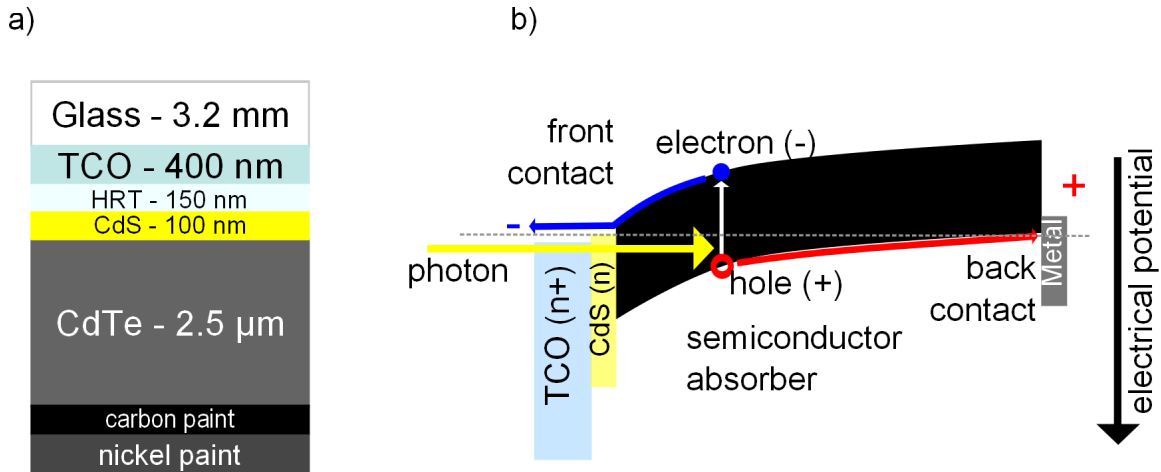


FIGURE 1.6. a) The physical structure of a baseline cell in this work consists of a series of thin films deposited on glass. b) A basic band diagram of a CdTe thin-film solar cell showing that light should be transmitted to the absorber, and charge carriers should be transported out.

contact with one another, their alignment is determined by considering their electron affinity (χ), defined as the energy required to move an electron from the CBM to the vacuum. The vacuum level must be continuous at the interface, and charge transfer may occur between the materials such that the Fermi level is flat in thermodynamic equilibrium. There may also be a net charge at the interface due to interface defects which cause band bending. For a metal, the work function is the important parameter to consider, and refers to the distance between vacuum and Fermi levels; these are shown graphically in Figure 1.3. The more ionic the semiconductor, the lower the influence of surface states; both CdS and CdTe are significantly affected by them, but are less sensitive than materials such as silicon and GaAs [20]. Like interfaces between different materials, grain boundaries within a polycrystalline material can have defects which may have net charge and cause interface recombination. Reasonably passive grain boundaries are considered a prerequisite to produce high-efficiency solar cells from polycrystalline materials.

1.3.2. DESIGN OF THE FRONT CONTACT. The most obvious requirement for the front contact is that there must be a way to transport the charge carriers and use them in an external circuit. A

TCO accomplishes this while still allowing most light through to the absorber. A TCO is a high-bandgap oxide semiconductor that is heavily doped and can be almost as conductive as a metal. As the doping is increased, the mobile charge carrier density increases, causing lower resistivity and higher free-carrier light absorption. The conductivity of the semiconductor is proportional to the product of carrier concentration and mobility, but absorption depends primarily on the carrier concentration. Therefore, optimizing mobility provides a more transparent material for a given conductivity.

Most photogenerated carriers are generated near the front of the device, and as a result the front contact must have minimal interface recombination, and still be optimized to collect electrons ohmically from the conduction band. Put another way, the front contact must preferentially collect electrons while allowing the holes to be transported to the back contact of the device. An n-type semiconductor at the front of the CdTe will create a built-in potential and a depletion layer; if the n-type layer is much more highly doped the depletion layer will be much thicker in the CdTe. This is called a one-sided abrupt junction and creates an electric field in the space-charge region of the CdTe that aids charge collection.

If the conduction band of the window is lower than the absorber, the energy offset between the window conduction band and absorber valence band will be reduced, causing a reduction in V_{OC} and fill factor by encouraging interface recombination. A similar situation can occur if the window is degenerately doped. The Fermi level of the degenerately doped material can be level with the absorber conduction band, but typically accumulation in the semiconductor will not occur [15] because the Fermi level is pinned at the conduction band of the absorber. Since the Fermi level is above the conduction band minimum of the highly doped layer, the window CBM will now be below the absorber CBM. In the other case, if the conduction band of the window layer is above the the conduction band of the absorber, there will be a barrier that the electron must surmount in

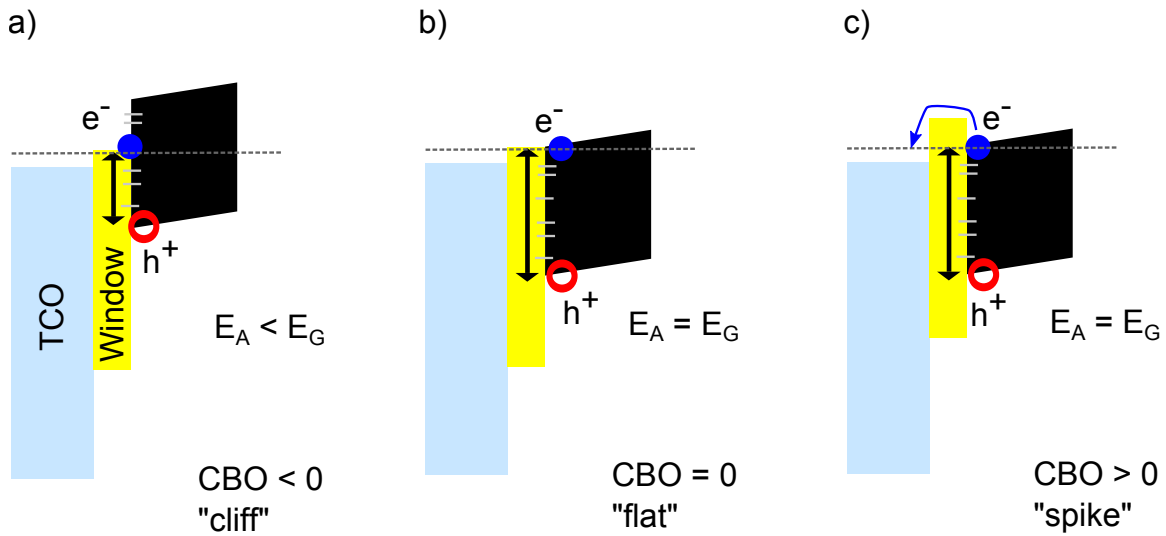


FIGURE 1.7. a) A negative conduction band offset (CBO) creates a reduced primary barrier height which promotes interface recombination through defects. b) A flat to slightly positive CBO will maximize the barrier height and allow collection of electrons. c) A large positive CBO will present a secondary barrier to electron flow. Adapted from [21].

order to be collected. This is referred to as a “spike.” If small, this is not a problem, but if too high, a barrier to current flow or “kink” will form. These situations are shown in Figure 1.7. The approximate maximum height is calculated by setting the saturation current of a Schottky barrier to the photocurrent and is approximately 0.3 eV for typical materials. Therefore, the ideal electronic material for a window layer is non-degenerately doped, and has a flat or small conduction band spike. Optically, the window layer should absorb as little light as possible, which means that a higher-bandgap material and a thinner layer is desired.

CHAPTER 2

DEVICE PROCESSING AND MEASUREMENT METHODS

2.1. THIN-FILM DEPOSITION

2.1.1. CHOOSING A SUBSTRATE. CdTe solar cells are typically built in the superstrate configuration, meaning a transparent structural material such as glass or plastic is coated with a transparent conducting oxide, and the semiconductor structure is grown on this template. For laboratory cells, aluminosilicate glasses are often used due to their transparency and ability to withstand high temperature processing. Soda-lime glass is used exclusively in commercial modules due to its low cost. It is sufficiently strong to withstand outdoor conditions, and can withstand the moderate processing temperatures used here due to its strain point of 511°C [22]. Relative to aluminosilicate glass, soda-lime glass has a lower strain point and higher coefficient of thermal expansion. Sodium diffusion can be a problem with this type of glass, with a significant amount found in commercial TCO [23]. Iron content can cause absorption in the visible spectrum [24]. Nevertheless, TCO-coated glass with low iron content, a sodium diffusion barrier layer, and high transparency is commercially available.

A variety of transparent conducting oxide (TCO) layers can be deposited on the substrate. Fluorine-doped tin oxide (FTO) is the standard TCO for commercial CdTe modules. FTO has the advantages that it can be deposited by atmospheric pressure chemical vapor deposition (APCVD) or spray pyrolysis directly on a glass float line, while the glass is still hot from production, which is a very high-rate and low-cost method. FTO is very stable to moisture and high-temperature processing, and it uses no rare or expensive elements. SnO₂ can survive high-temperature processing

including the CdCl_2 treatment without intermixing with the other layers [25]. This work predominately uses soda-lime glass with APCVD FTO as the TCO material, except when specifically noted.

2.1.2. THE FRONT CONTACT. The front contact consists of one or more layers which are designed to collect photogenerated electrons from the front of the CdTe absorber. As previously mentioned, this region is critical for power conversion because excess carrier generation occurs in a profile exponentially decreasing from this interface.

Various types of high-resistance transparent (HRT) oxide layers can be used; this layer is deposited on the TCO either in-line at the glass float, in a laboratory CVD coating apparatus, or by sputter deposition. The HRT layer is an oxide which is much more resistive than the TCO and is discussed in detail in Chapter 3; empirically the HRT has proven to allow thinner CdS and higher current. A CdS window layer is nearly ubiquitous in reported high-efficiency cells. The window layer can be deposited in a number of ways. Chemical bath deposition (CBD) is common for laboratory cells; this method produces a film that has very small grains and contains oxygen [26]. Sputter deposition and sublimation can also be used to deposit CdS. Baseline cells produced in this work use sublimated CdS. Sputter-deposited, oxygenated CdS films are examined in depth in Chapter 4.

2.1.3. CdTe THIN-FILM SOLAR CELL PROCESSING. The CdTe absorber is typically p-type because it is preferable for the lower-mobility holes to be the majority carriers; the minority-carrier electrons must be collected from the device quickly. Though controlling the carrier concentration is difficult in polycrystalline CdTe, sublimated films are naturally p-type at a hole concentration very commonly near 10^{14} cm^{-3} . Numerous methods have been used to successfully deposit CdTe

films of reasonable efficiency, including close-space sublimation, vapor transport deposition, and radio-frequency magnetron sputter deposition.

The CdCl₂ treatment typically consists of annealing the layers in the presence of a solid layer of CdCl₂ or CdCl₂ vapor in the range of 400°C for at least several minutes. This treatment is critical to making high-efficiency devices and is thought to passivate the device [27], with evidence that chlorine concentrates at grain boundaries [28]. Finally, creating an ohmic contact at the back of the device is non-trivial and typically copper or a copper containing compound is used to dope near the back interface of CdTe; this step is the most likely to adversely affect long-term device stability [29] and the dose is carefully minimized.

2.1.4. BASELINE DEVICE PROCESSING. ¹ The majority of the processing for this work was performed in the Colorado State University Advanced Research Deposition System (ARDS). The system is capable of performing all semiconductor operations for a CdS/CdTe solar cell, including substrate pre-heating, CdS deposition, CdTe deposition, CdCl₂ treatment, and Cu back contact formation via sublimation of CuCl vapor. In this system, an automated magnetic transfer arm moves the substrate into any of nine process positions in any programmed sequence. Each process position consists of a graphite top heater and a bottom graphite heater or shuttered sublimation source, each with an integrated resistive heater [31]. The TCO-coated glass is introduced with the TCO facing down. The purpose of the top heater is to control the substrate temperature by radiatively heating or cooling the high-emissivity, uncoated top of the glass. The bottom heater also contributes to substrate temperature control, but can be filled with sublimation material. The sublimation rate of the material in the graphite pocket is set by the temperature of this source and, given a standard cycle time of deposition, determines the thickness of the layer deposited on the glass substrate.

¹This section was adapted from Kephart *et al.* [30]

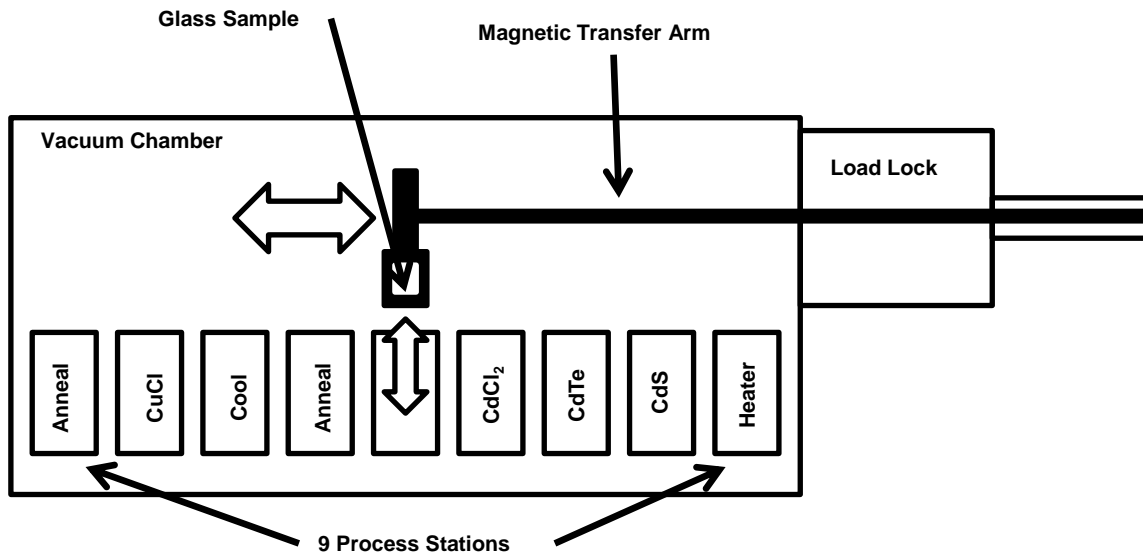


FIGURE 2.1. The Advanced Research Deposition System (ARDS) has a transfer arm which allows automated movement of a substrate between nine process stations in any sequence. A top view schematic shows the movement of the sample via the transfer arm.

For a baseline sample, TCO-coated glass is heated to approximately 450°C (as measured by an in-situ pyrometer), then CdS and CdTe layers are sublimated in sequence using a 2-minute cycle time, with the source bottom temperatures determining layer thickness and the top heater temperatures maintaining proper substrate temperature (480-500°C). Standard thickness values are 120-130 nm for CdS and 2.5 μm for CdTe. The device is placed in the CdCl₂ position where it is exposed to CdCl₂ vapor; near the end of this three-minute step deposition of a thin CdCl₂ layer occurs as the substrate cools below the source temperature of 435°C. The substrate is then left to anneal in a 400°C annealing position for another three minutes. The sample is then allowed to cool radiatively to below 150°C in a room-temperature position before removal from the ARDS and exposure to air.

At this stage the CdCl₂ is rinsed off with deionized water and blown dry with UHP N₂ gas. The sample is re-introduced to the ARDS, heated to 175°C, and exposed to copper (I) chloride vapor for 2 minutes. The temperature of the CuCl source determines the total copper dose. A

temperature of 170°C produces a low dose which does not eliminate roll-over (a reduction in fill factor from a non-ohmic back contact), and a temperature of 210°C produces an ohmic back-contact but poor stability. A temperature of 190°C is considered standard and balances initial efficiency with stability. The substrate is annealed at 200°C for 4 minutes and cooled in vacuum. The sample is again rinsed and blown dry. All ARDS steps are carried out in 2% O₂/98% N₂ at a pressure of 40 mTorr.

The back of the Cu-doped CdTe absorber is contacted with a carbon-filled acrylic paint (Henkel Electrodag 109) followed by a nickel-filled acrylic paint (Henkel Electrodag 440 AS) which has a much lower sheet resistance. Cells are delineated by clamping a cylindrical mask over the painted surface and removing the exposed paint and semiconductor layers with melamine blasting media to expose the TCO/HRT layers. Indium is soldered onto the transparent layers in a ring around the cell for a front electrode. Nine devices with diameter of approximately 1 cm are delineated on each 8-by-9 cm substrate. The appearance of these devices are shown in Figure 2.2.

2.1.5. SPUTTER DEPOSITION SYSTEM. Sputter deposition of window layers is performed in a separate vacuum system from the ARDS, the components of which are shown in Figure 2.3. Sputter deposition is the process of depositing a film on a substrate from mass of material called a *target* using a plasma. In a plasma, electrons are separated from atoms creating positively charged ions which impact the target due to a voltage bias. Magnets are typically used to confine the plasma over the target, greatly increasing the deposition rate for a given amount of power. Targets in this work are flat disks but can also be rectangular or cylindrical. A DC bias can be used to ignite the plasma and create the bias which leads to bombardment of the target; for insulating materials this can cause arcing since charge can accumulate at the target surface. An alternative is to use a radio-frequency power source, which excites a plasma, and also creates a bias on the target due to the difference in diffusivity of electrons and ions based on their drastically different masses.

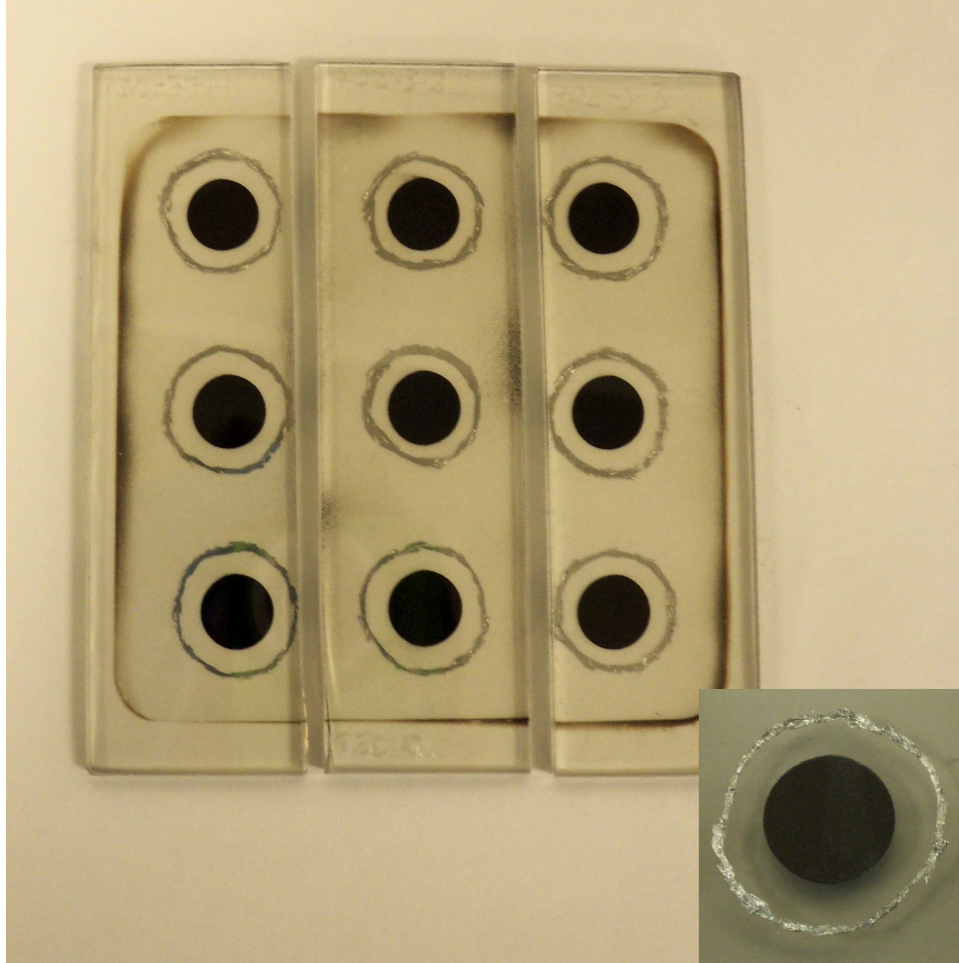


FIGURE 2.2. Nine devices are made on each substrate. The indium solder and painted back electrode can be seen in the inset.

Noble gases are the primary gases used for sputtering, since they do not react with materials being deposited, but reactive gases can be added to affect the chemical composition of the deposited film. The pressure of the gas is an important variable. At very low pressures, below 0.1 to 1 mTorr, it may be difficult to keep a plasma ignited, and as pressure is increased the number of ions getting directly to the substrate are reduced, and reduced diffusion and thermalization of sputtered atoms may cause slower deposition [32].

The system used in this work is pumped via a diffusion pump and can reach a base pressure below $2 \cdot 10^{-6}$ Torr. A 4-inch diameter planar cathode sits in the center of a cylindrical chamber

which has a door for sample exchange; this was recently updated to a full load lock system capable of sample exchange with plasma ignited. The cathode is powered by an Advanced Energy CESAR RF generator connected to a match network using a frequency of 13.56 MHz. The sputter deposition system is capable of substrate heating to 450°C, but all sputter-deposited window layers discussed herein were deposited on room-temperature substrates. The primary gas is argon, controlled by a 100 sccm mass-flow controller (MFC), but a second 1.5-sccm MFC is calibrated to oxygen and the relative flow rate of the gases, along with the chamber pressure, can be controlled as desired using a LabVIEW program. A 10-sccm oxygen MFC is also installed for experiments in which higher partial pressures of O₂ are needed. Typical flow during deposition is approximately 20 sccm and base pressure before deposition is below 10⁻⁵ Torr. Standard conditions for sputter deposition of oxygenated CdS in this system using a CdS target (Kurt J. Lesker) are a substrate-target distance of 9 cm, pressure of 15 mTorr, and real RF power of 60 W. (Mg,Zn)O films are deposited from targets of mixed MgO and ZnO powder (Plasmaterials) at a distance of 15 cm and a pressure of 5 mTorr, with real power of 180 W.

2.2. DEVICE MEASUREMENTS

A measurement system was built based on an ABET Technologies 10500 solar simulator with xenon arc lamp, AM1.5 filter, and uniform illumination accessory (Figure 2.4a) to measure solar cell J-V curves efficiently and accurately. A Keithley 2402 SourceMeter in 4-wire configuration measures current and voltage from the cell. The default measurement configuration is from -0.8 to 1.2 V in 25 mV increments, although any arbitrary set of voltages can be enabled in the settings, along with a limiting current to prevent damage to the cells. A webcam along with an object identification algorithm measures the area of a backlit cell to provide accurate values of current density. This system is capable of measuring each cell in approximately 30 seconds, which allows

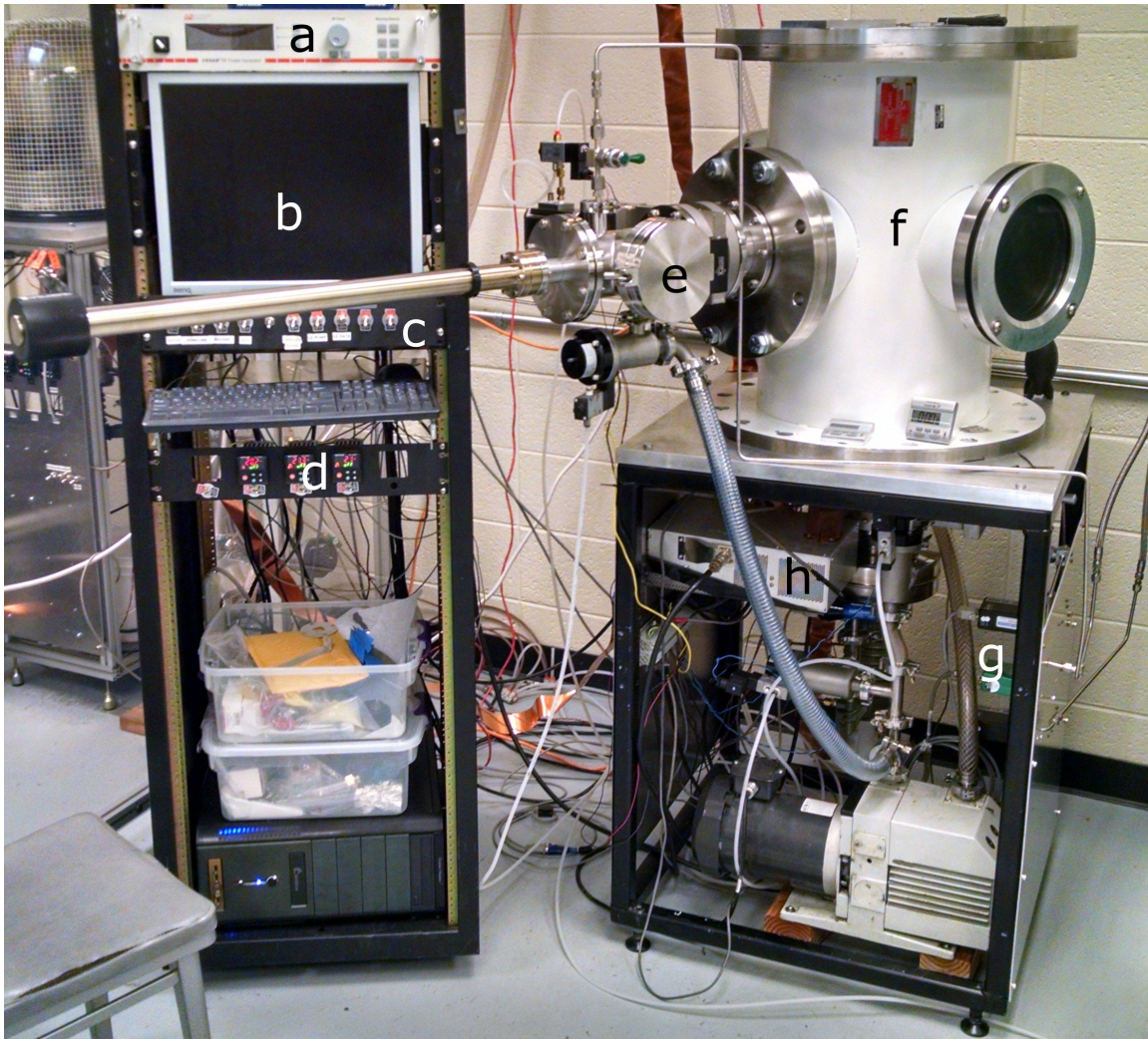


FIGURE 2.3. The RF sputter deposition system with a) RF Generator, b) computer control of pressure and gas composition, c) controls for pumping system, d) up to 3 independent temperature measurements with PID substrate temperature control, e) load lock with magnetic transfer arm, f) stainless steel vacuum chamber, g) independently controlled MFC's for argon and oxygen, and h) an RF match network.

for statistical analysis of large numbers of solar cells. Results are output in plain text, which allows for efficient visual and mathematical analysis of the results using an integrated LabVIEW program, or data analysis in spreadsheet form or a programming language such as R. Several thousand cells were measured on this system for this work.

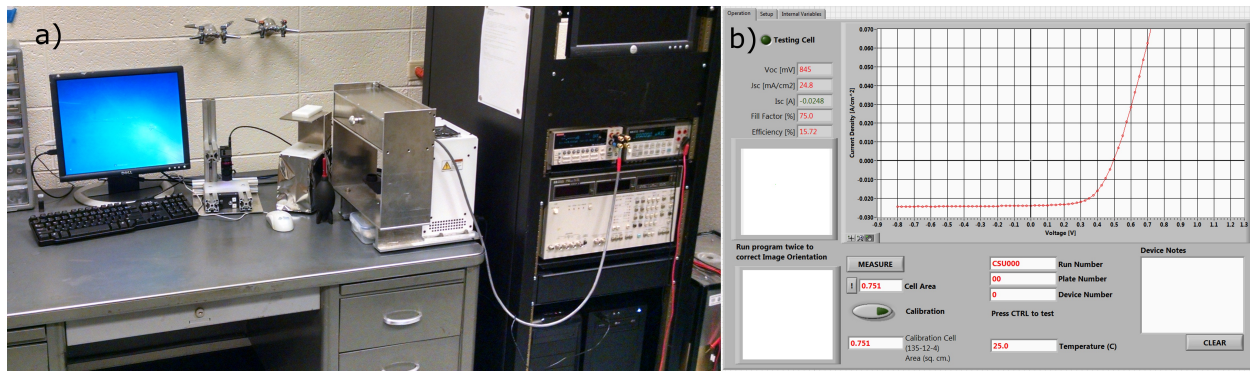


FIGURE 2.4. a) The characterization system consists of computer control, a solar simulator and sourcemeter. b) A LabVIEW program controls measurement parameters and records the data.

CHAPTER 3

HIGH-RESISTANCE TRANSPARENT (HRT) LAYERS¹

3.1. INTRODUCTION

Cadmium telluride thin-film solar cells have recently seen a rapid increase in record cell efficiency up to 21.5% [33]. Part of this increase is due to the high optical collection of this technology [34]. Typically CdTe thin-film solar cells are grown in the superstrate configuration, starting with TCO-coated glass. Another oxide layer, dubbed the *high-resistance transparent (HRT)* or *buffer* layer, is often deposited on the TCO, followed by a CdS-based window layer. It has been shown empirically that the addition of the HRT layer between the TCO and CdS window layers allows for reduced CdS thickness. The oxide layer typically absorbs little to no light, and thinner CdS reduces the absorption and loss of blue photons in the CdS layer, increasing maximum efficiency.

The most commonly used TCO in commercial CdTe cells is fluorine-doped SnO₂ (FTO) because it can be deposited during the glass manufacturing process cheaply and is mostly inert to subsequent processing steps. Still, cells have successfully been made using In₂O₃:Sn (ITO),[35] Cd₂SnO₄ (CTO),[36] and ZnO:Al (AZO) [37]. Many TCO/HRT combinations have been studied, with HRT layers including ZnO [38], In₂O₃ [39, 40], Ga₂O₃ [39], SnO₂ [27, 39–41], and alloys of these materials such as zinc stannate [42, 43]. A universally described feature of these layers is their increased resistivity relative to the TCO.

3.1.1. THICKNESS AND COVERAGE OF WINDOW LAYERS. A commonly accepted explanation of the HRT's role in CdTe solar cells considers the effect of pinholes, or small areas where

¹This chapter was adapted from a manuscript prepared for submission to *Solar Energy Materials & Solar Cells*.
J. M. Kephart: Wrote the manuscript, fabricated all devices, and performed materials and device characterization.
Z. Ma: Designed and fabricated TCO and HRT layers and performed beamline measurements.
J. M. McCamy: Served as Principal Investigator for design of TCO and HRT layers.
A. Ganjoo and F. M. Alamgir: Designed and performed beamline experiments.
W.S. Sampath: Served as Principal Investigator for CdTe device processing.

there is no CdS coverage and CdTe directly contacts the oxide layer. According to this explanation, a diode with high open-circuit voltage will be formed as long as there are no CdS pinholes. The area that contacts the oxide below is a weaker diode with high forward current and low open-circuit voltage [39]. A loss in open-circuit voltage is seen when CdS thickness is reduced, and this is ascribed to an increasing fractional pinhole area across the substrate [41]. This theory assumes that pinhole area increases as overall window layer thickness decreases. By adding an ohmic resistor between the TCO and the CdS, the theory states, less CdS is required because the shunting effect of pinhole area is reduced. In devices made in the CSU ARDS there is little evidence that the existence of pinholes is correlated with window layer thickness. Statistical measurements have not shown an increase in pinhole area with reduced CdS thickness for films made at CSU [44]. Likewise, devices that have both lower pinhole area and reduced CdS thickness nevertheless show lower V_{OC} , indicating that window layer thickness in itself is an important variable [45]. Presently the role of the HRT is not considered clear or completely understood with yet another possibility involving the effects of thermal expansion [46].

3.1.2. THE ROLE OF THE FRONT CONTACT. Key to understanding the role of the HRT is noting the difference between the CdS/CdTe junction and the TCO/CdTe and HRT/CdTe junctions. As a wide-bandgap, n-type semiconductor, FTO can be used directly as the front contact of the solar cell. Commonly used values for the tin oxide electron affinity indicate that this layer has a relatively flat conduction band alignment with CdTe [47]. As reported here and previously [39], a FTO/CdTe junction results in a cell with very low open-circuit voltage.

Key properties of these junctions are interface recombination, carrier concentration of the n-layer, and conduction band offset. To reduce interface recombination, a good crystallographic match is considered important to reduce the interface defect density, and to provide a growth template which minimizes defects in the CdTe bulk. CdS shows a lattice mismatch of 10%, and

only interdiffuses slightly during high-temperature device processing [48]. Another way to reduce interface recombination is to reduce the concentration of carriers at the interface. Modeling suggests that even at essentially complete interface recombination ($S = 10^7$ cm/s), the reduction in V_{OC} and efficiency is limited, particularly for modest bulk lifetimes of a few nanoseconds[49, 50]. Therefore, interface recombination alone cannot account for the dramatic loss of efficiency of an SnO_2/CdTe junction. Likewise, the carrier concentration and thickness of typical TCO and HRT layers is sufficient to deplete the CdTe layer and is not responsible for the drop in efficiency.

3.1.3. BAND ALIGNMENT. The conduction band offset of an interface is determined by the electron affinity of the two materials, net charge at the interface, and the difference in electronegativity (which is usually a minor effect). Charged defects could be caused by a variety of reasons including the termination of the lattice of either material or the accumulation of electronically active species at the interface. To create the maximum built-in potential across the cell, the Fermi level must be pinned near the conduction band at the front CdTe interface, meaning the alignment should be flat or slightly positive (a “spike” rather than a “cliff”) [21]. Therefore, the electron affinity of the HRT, including any effects of surface charge, should be a key predictor of HRT performance.

3.2. EXPERIMENTAL

Commercial low-iron soda-lime glass coated with $10\text{-}\Omega/\square$ $\text{SnO}_2\text{:F}$ TCO (“R10H1” manufactured by PPG Industries, Inc.) was the standard substrate for SnO_2 -based HRT layers. HRT layers were deposited on R10H1 using atmospheric pressure chemical vapor deposition (APCVD) in a laboratory reactor, which simulates the in-line manufacturing process. All HRT layers deposited by PPG Industries were SnO_2 -based, with tin composing a minimum of 80 at% of cations. Complete thin-film CdTe solar cells were prepared in the CSU Advanced Research Deposition System

(ARDS). This system was used for CdS, CdTe, CdCl₂ and Cu process steps; oxygenated CdS and Mg_xZn_{1-x}O window layers were deposited in a separate system by RF sputter deposition. Cell fabrication and oxygenated CdS procedures have been described in detail [30]. Mg_xZn_{1-x}O was deposited using a 10-cm diameter target with a power of 180W, a pressure of 5 mTorr, 1% O₂ in argon, and a target-substrate distance of 15 cm. Solar cell efficiency measurements were performed using a xenon arc lamp with AM1.5 filter; short-circuit current density was calibrated to cells measured by NREL.

Band measurements were performed using a PHI 5800 XPS with a PREVAC UVS40A2 UV source. Samples were cleaned and heated in the ARDS to approximate the condition of the surface prior to semiconductor deposition. Samples were removed from the ARDS under an inert environment and prepared in a glovebox under argon. Air exposure of the samples was less than 10 seconds during loading into the XPS to limit atmospheric contamination of the surface (see Appendix A for further information). Measurements were taken at a take-off angle of 85° and a sample bias of -5 V. Analysis followed the procedure of Helander *et al.* [51]. Synchrotron-based measurements were performed on beamline X1B at the National Synchrotron Light Source at Brookhaven National Laboratory. For XES and XAS measurements a beam energy of 550 eV was used which corresponds to an attenuation length in SnO₂ of 80 nm.

3.3. SnO₂-BASED HRT LAYERS

3.3.1. IMPACT OF HRT LAYER ON DEVICE PERFORMANCE. Many candidate HRT layers were tested with various alloying elements, alloy composition, and thickness. These layers were screened to test quickly which were most effective. For devices with no HRT, a minimum of approximately 100 nm CSS CdS is needed to achieve maximum V_{OC} , so the effectiveness of the buffer could be tested by depositing only 90 nm CdS on the devices. Devices would also be made

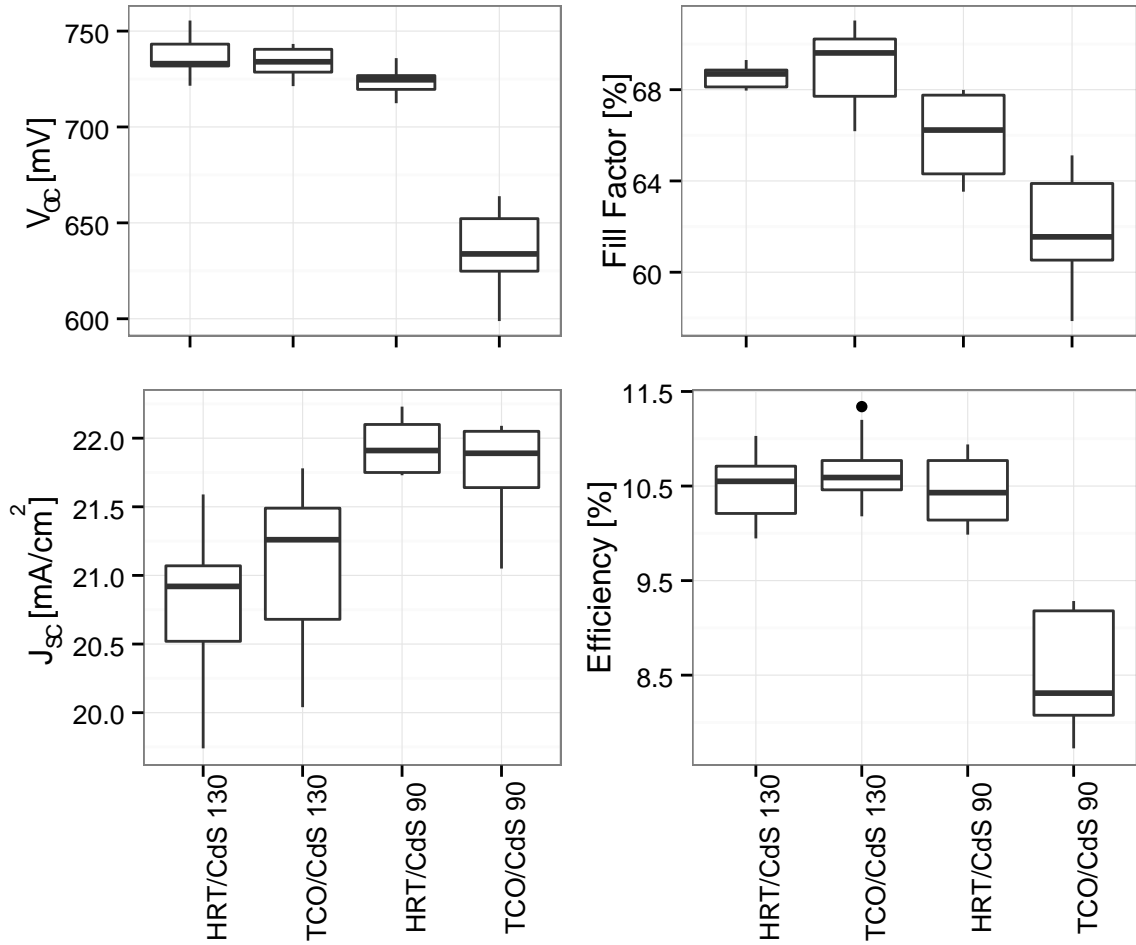


FIGURE 3.1. An effective HRT will produce better devices as the CdS layer is made thinner. Numbers refer to CdS thickness in nanometers.

using the baseline CdS thickness of 130 nm. Typically, the HRT did not affect the devices with thick CdS; with 90 nm CdS, an effective HRT would have higher average V_{OC} and fill factor than its comparison sample without HRT. The thinner CdS would also produce a higher current. A typical result of these experiments is shown in Figure 3.1,

Devices were made at gradually decreasing CdS thickness on the best-performing HRT layer ($\text{SnO}_2:\text{Zn}$, 2.4 at%) with devices made on plain TCO serving as a control (see Figure 3.2). Device quality has little dependence on window layer thickness above a critical value. Below this value, V_{OC} gradually declines and shows a minimum at 0 nm (an oxide/CdTe junction). Meanwhile, current continuously improves with less CdS. Devices with the HRT show both a lower critical

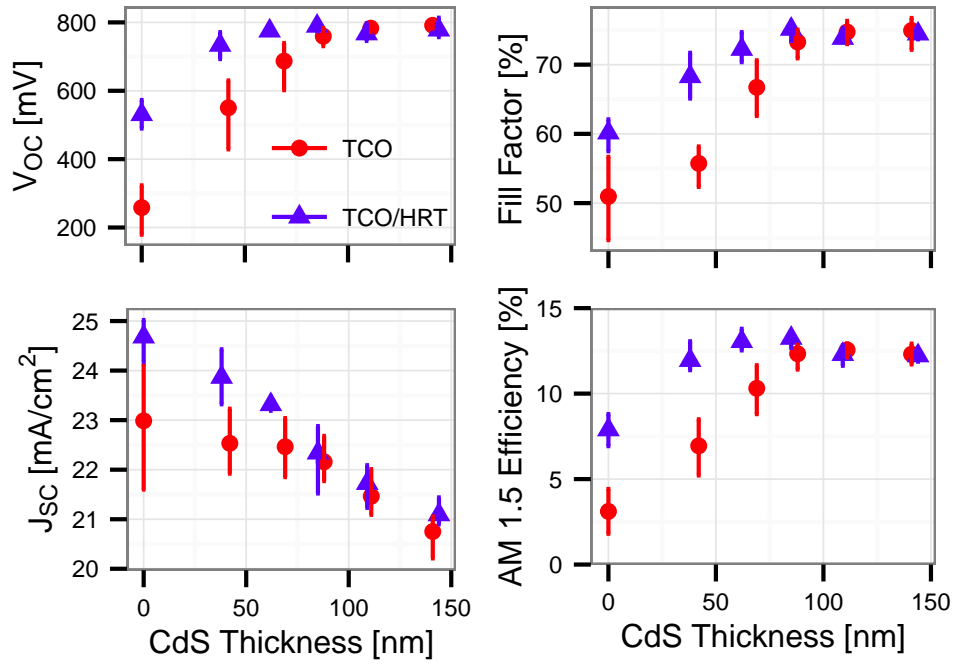


FIGURE 3.2. Efficiency parameters of cells made with varying CdS thickness, adapted from previous work [45].

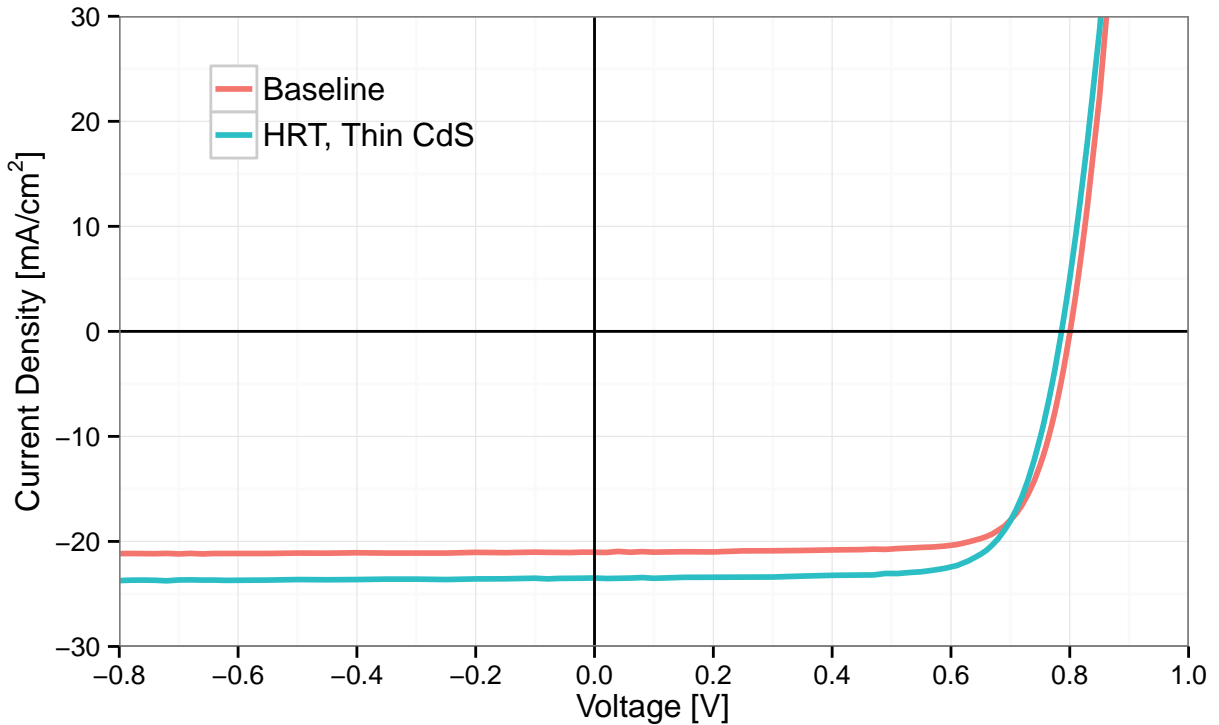


FIGURE 3.3. J-V curve of optimal cells with and without HRT. The HRT allows additional short circuit current from thinner CdS, with minimal loss in V_{OC} . Maximum efficiency was improved from 12.9% to 13.8%.

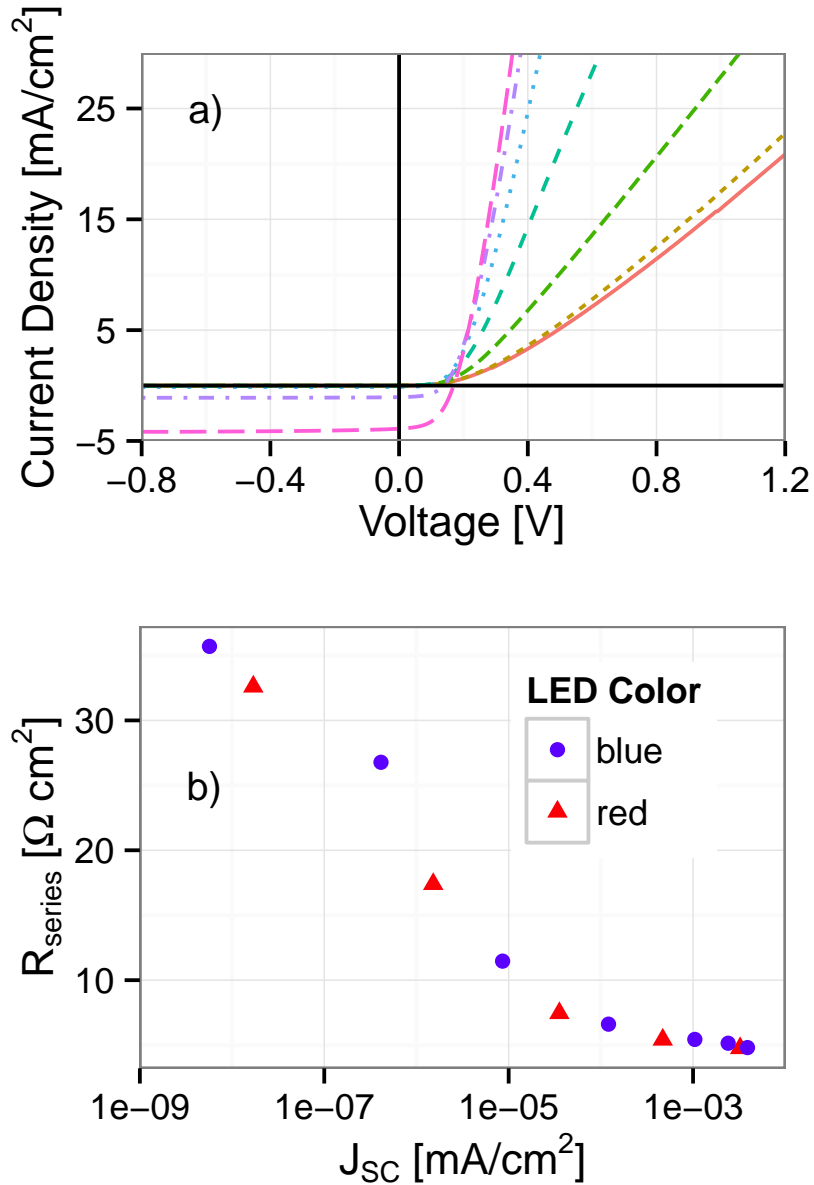


FIGURE 3.4. Series resistance of a FTO/CdTe junction device. a) Series resistance is reduced drastically with illumination. b) The dependence is comparable for illumination with red and blue light.

thickness and a higher V_{OC} with 0 nm of CdS. For all values of CdS thickness, devices with high shunt resistance values exist. The optimal device from this study with and without CdS are shown in Figure 3.3 and highlight the importance of short-circuit current gains as the benefit of the HRT layer.

With reduced CdS thickness, devices show light-dark crossover that increases as CdS thickness decreases. This behavior was examined by illuminating the devices with red and blue light-emitting diodes and varying the supply current by several orders of magnitude. Some FTO/CdTe junctions exhibit strong light-dark crossover, in which low illumination levels cause a large drop in series resistance. As Figure 3.4 shows, the relationship between J_{SC} and series resistance for one device is comparable when red and blue LEDs are used. Without CdS, the presence of light still greatly reduces the barrier to forward electron current. For a variety of front contacts, higher V_{OC} is correlated with reduced light-dark crossover.

3.3.2. BAND MEASUREMENTS OF HRT LAYERS. A subset of all the HRT layers tested were chosen with a variety of alloying element and concentration, all with a standard thickness of 150 nm. Since the CdS deposition rate has some spatial variation and is sensitive to the thermal and surface properties of each HRT, devices were made directly on each HRT layer and the uncoated TCO. A second set of devices also has a 50 nm oxygenated CdS window layer, and the third set has 50 nm sublimated CdS. The selected subset of SnO₂-based HRT layers was measured by UPS. These measurements are summarized in Table 3.1. The work function was extracted as a way to estimate band alignment, since films had carrier concentrations which would place the Fermi level near or above the conduction band minimum. For each combination of parameters, a substrate with nine devices was prepared. The sputtered, oxygenated CdS has very low free electron concentration which was measured at approximately 10^{12} cm^{-3} by van der Pauw method after annealing to process temperatures of 500°C. Figure 3.5 shows that for oxide/CdTe devices, work function is a strong predictor of V_{OC} (as well as efficiency). This dependence becomes somewhat weaker for oxygenated CdS and weaker still for devices with sublimated CdS.

The TCO and optimal HRT layer also characterized via x-ray emission spectroscopy and x-ray absorption spectroscopy at a photon energy of 550 eV. These techniques do not require emission of

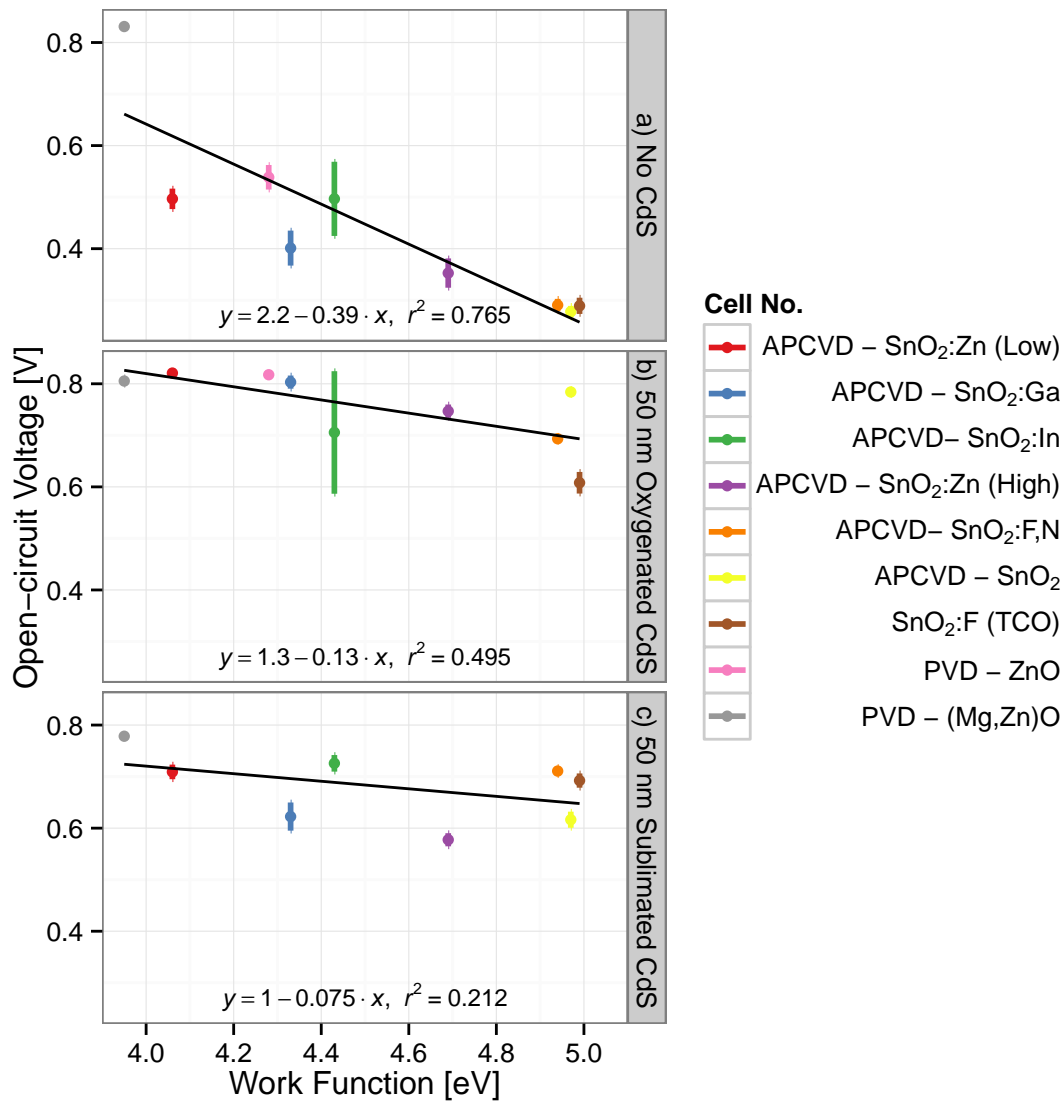


FIGURE 3.5. Comparing UPS measurements of work function with device results, a) there is a strong correlation when oxide/CdTe junctions are made, b) the correlation is somewhat weaker when a resistive oxygenated CdS window layer is used; and c) the dependence is quite weak but present when sublimated CdS was used as the window layer.

a photoelectron and therefore probe more deeply than XPS and UPS, with an attenuation length of approximately 80 nm. X-ray absorption spectroscopy probes the unoccupied states of the material; the grounding current of the sample is measured to determine the extent of absorption. X-ray emission spectroscopy measures the energy of X-rays that are emitted when electrons fall from valence states to core holes created by incoming radiation. These techniques show that both the

TABLE 3.1. Band measurements of various oxides deposited on FTO are summarized. The valence band positions show good agreement with material bandgaps.

Oxide	ϕ [eV]	$E_F - E_V$ [eV]	d [nm]
SnO ₂ :Zn (2.4 at%)	4.1	3.9	150
SnO ₂ :Ga	4.3	3.9	150
SnO ₂ :In	4.4	3.8	150
SnO ₂ :Zn (10 at%)	4.7	3.7	150
SnO ₂ :F,N	4.9	3.9	95
SnO ₂	5.0	3.9	150
SnO ₂ :F (TCO)	5.0	3.9	400
PVD ZnO	4.3	3.3	50
PVD (Mg,Zn)O	4.0	3.8	50

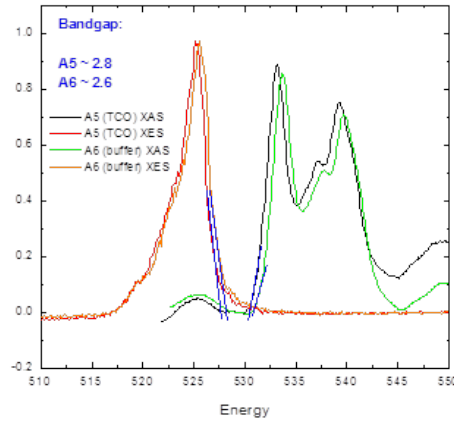


FIGURE 3.6. Using X-ray emission spectroscopy to probe the valence band and X-ray absorption spectroscopy to probe the conduction band, a clear shift to lower binding energy is seen in the HRT versus the TCO. Figure courtesy of F.M. Alamgir.

valence and conduction bands shift to lower binding energy in the HRT versus the TCO as seen in Figure 3.6.

3.3.3. 1-D MODELING OF HRT LAYER BAND ALIGNMENT. Modeling of 1-dimensional structures was conducted in the SCAPS software [52]. This model is a simplification of the actual cell and ignores phenomena related to grain boundaries and complex interfacial effects. The results demonstrate the importance of front contact band alignment parameters and their effect on device performance. The assumed properties of the baseline and HRT cells are shown in Table 3.2. All

TABLE 3.2. 1-d modeling baseline parameters used for SCAPS simulation of HRT and window material property effects.

Parameter	TCO	HRT	Window	CdTe
x [nm]	400	150	50	2500
E_G [eV]	3.6	3.6	2.4	1.5
χ [eV]	4.8	4.5	4.5	4.4
ϵ/ϵ_0	9	9	10	9.4
N_C [cm^{-3}]	$2.2 \cdot 10^{18}$	$2.2 \cdot 10^{18}$	$2.2 \cdot 10^{18}$	$8.0 \cdot 10^{17}$
N_V [cm^{-3}]	$1.8 \cdot 10^{19}$	$1.8 \cdot 10^{19}$	$1.8 \cdot 10^{19}$	$1.8 \cdot 10^{19}$
μ_e [$\text{cm}^2/\text{V}\cdot\text{s}$]	30	1	100	320
μ_h [$\text{cm}^2/\text{V}\cdot\text{s}$]	25	25	25	40
τ_n, τ_p [ns]	0.1	0.1	0.1	2
n or p [cm^{-3}]	n = $5 \cdot 10^{20}$	n = $1 \cdot 10^{18}$	n = $1 \cdot 10^{17}$	p = $2 \cdot 10^{14}$
	Window/CdTe	CdTe/Back		
S_n, S_p [cm/s]	10^5	10^7		

parameters were taken from commonly used values [47] apart from an equal hole and electron lifetime of 2 ns in the CdTe absorber.

The first parameter examined is the electron affinity of the HRT layer. If this property can effect the open-circuit voltage, even with the CdS window layer present, then this supports the experimental correlation of electron affinity to device results. Figure 3.7 shows that this is indeed the case. For a very low electron affinity of 4.2 eV, there is a small kink due to a conduction band spike; this device has the same V_{OC} as the baseline case. At higher than ideal electron affinity, the V_{OC} is at first unaffected and then drops as χ approaches 5.0 eV. An offset at the HRT/window interface causes the Fermi level to move away from the CBM in the window layer; however, due to the carrier concentration of 10^{17} cm^{-3} in the window, there is enough transfer of electrons into the HRT to reduce this effect at the window/CdTe interface. The effect on device performance is not noticeable until quite a high electron affinity of 5.0 eV; here, the loss of efficiency is fairly modest with the maximum power voltage moving approximately 150 mV lower. This modeled device also has a pronounced barrier to forward current shown as a horizontal line just below the x-axis. This

is due to the barrier at the TCO/HRT interface, and in reality this effect would not occur since electrons could easily tunnel through the narrow TCO-HRT depletion region.

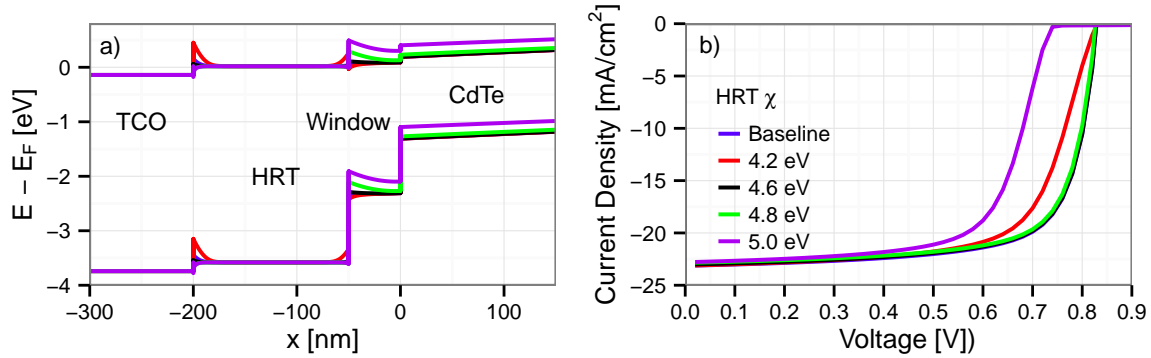


FIGURE 3.7. a) The band diagram of the front contact region shows that the higher electron affinity HRT causes the Fermi level to move down and away from the conduction band minimum at the front interface of CdTe. b) An HRT layer with high electron affinity leads to reduced efficiency.

From this model, the cadmium sulfide window layer was changed to have a much lower carrier concentration of 10^{12} cm^{-3} . This is comparable to the carrier concentration of oxygenated CdS using Hall effect measurements made by the van der Pauw method. It is hypothesized that this material, because of its lower carrier concentration, is not capable of fixing the Fermi level near the conduction band minimum at the front interface of CdTe as effectively as the standard window. This causes the layer to “transmit” any unfavorable band alignment due to high electron affinity of the poor-performing HRT or TCO through to the CdTe interface. As Figure 3.8 shows, there is no visible band bending at the HRT/window interface due to the long Debye length of the material. Thus, a high electron affinity causes a reduced built-in potential across the CdTe. The device with an HRT electron affinity of 4.8 eV now shows comparable degradation to the previous sample at 5.0 eV; the 5.0 eV device with resistive window layer has a maximum power point approximately 300 mV below baseline. Again, there is a barrier to forward current, this time at the HRT/window interface. A less pronounced version of this rollover has been seen in actual devices.

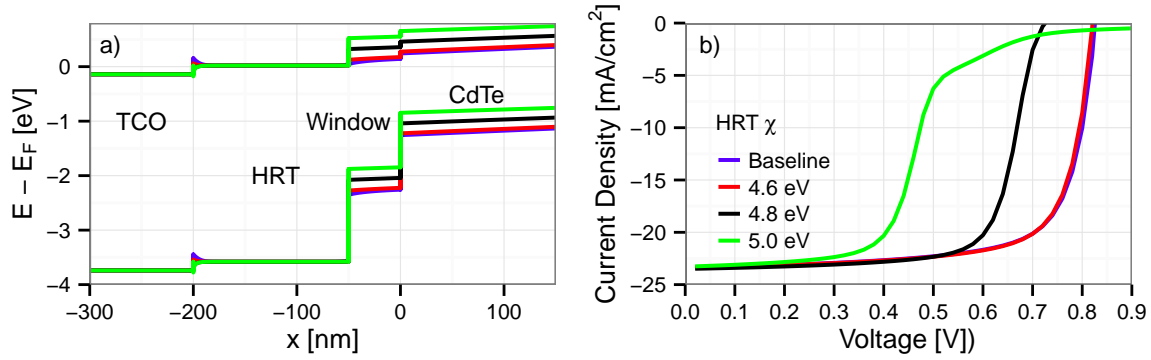


FIGURE 3.8. a) With a window layer that has very low carrier concentration, band bending in the window layer does not occur, and b) device performance becomes more sensitive to HRT electron affinity.

To test the effect of negative charge at the TCO interface, $2 \cdot 10^{13} \text{ cm}^{-2}$ acceptors were placed 0.5 eV above the CdTe valence band. At the interface, acceptor-like defects that are well below the Fermi level are negatively charged. These results are shown in Figure 3.9. These were given a small cross section of 10^{-19} cm^{-2} to have a minimal effect on surface recombination. With the HRT this amount of charge had no effect. With the standard CdS ($n = 10^{17} \text{ cm}^{-3}$) some band bending is induced, but the contact with CdTe is unaffected. Only with the low-carrier-concentration window layer ($n = 10^{12} \text{ cm}^{-3}$) representative of oxygenated CdS (discussed further in Chapter 4) was there an effect on the device properties. Overall surface charge due to acceptor-like states have similar effect to changing the electron affinity.

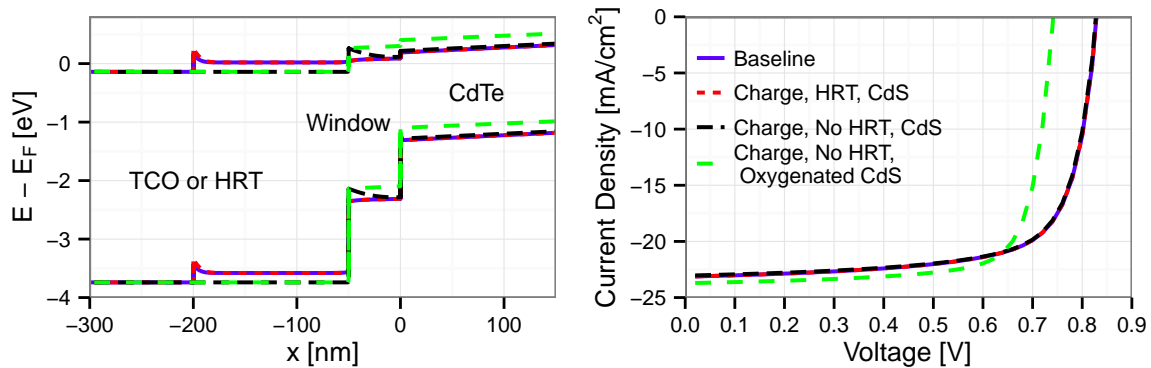


FIGURE 3.9. Charge at the TCO interface affects the band alignment. For the density of charge modeled here, only the device with no HRT and resistive CdS was affected.

3.4. ZNO AND (MG,ZN)O HRT LAYERS

ZnO has been used as an effective HRT. When CdTe is deposited directly on sputtered ZnO, V_{OC} of typically 500-600 mV is produced. Band alignment measurements indicate that a negative conduction band offset with CdS exists; alloying with MgO to produce $Mg_xZn_{1-x}O$ with a composition of $x = 0.15$ can produce a flat conduction band alignment with CdS [53].

In Cu(In,Ga)Se₂ thin-film solar cells, this material has been shown to have superior performance to ZnO when used as a window layer [54]. This material has the added benefit of increasing the optical bandgap of the layer [55] for better UV light transmission. Varying the magnesium content from $x = 0$ to $x = 0.30$ allowed researchers to tune the conduction band offset between a “cliff” and a “spike,” with both open-circuit voltage and fill factor improving with magnesium addition [56]. Over this range, the films remain in the wurtzite crystal structure with the lattice constant reducing from 0.522 nm to 0.515 nm for films deposited on glass at 300°C[57].

In this work $Mg_xZn_{1-x}O$ was examined as an HRT layer by RF sputter deposition using hot-pressed, mixed-powder targets (Plasmaterials, Inc.) with compositions of $x = 0.15, 0.20,$ and 0.25 (MgO weight percentages of 8, 11, and 14% with the remainder ZnO). Films made from these targets exhibited the expected increase in optical bandgap relative to ZnO; measurements by XPS of the 11% film shows the magnesium content x is higher in the film than in the target, about 0.23, in agreement with Hariskos *et al.* [54]. At each composition, a thick film with measured thickness about 500 nm was deposited on uncoated glass for optical measurements. In Figure 3.10 the transmission is shown over a wide range of wavelength along with the optical bandgap calculated from Tauc plots of the data. The films are transparent from their bandgap in the range of 350-400 nm all the way to long wavelengths up to 2 μm . The bandgap increases as expected with increasing magnesium composition.

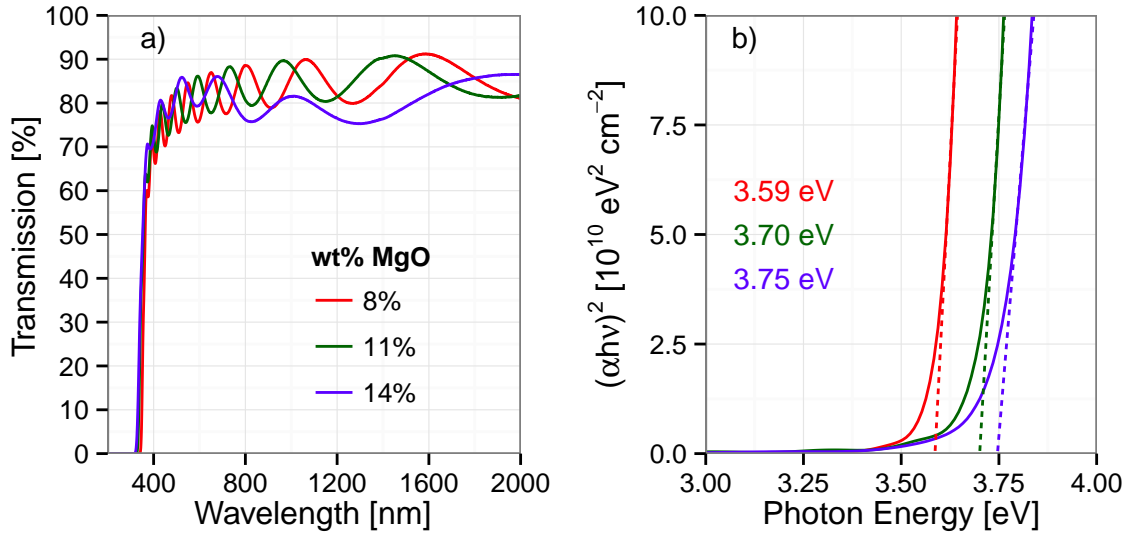


FIGURE 3.10. a) The transmission of the films remains high over a wide wavelength range. b) The Tauc plot shows increasing optical bandgap with magnesium content.

Films approximately $1 \mu\text{m}$ thick at each magnesium concentration were deposited on low-alkali Eagle XG glass (Corning) in order to limit the potential electronic effects of sodium diffusion. Small 1-cm square samples were prepared with soldered indium contacts at the electrodes, and Hall measurements were attempted using an Ecopia HMS-3000 van der Pauw system. The samples were too resistive to measure, implying a resistivity of $10^7 \Omega\text{-cm}$ or greater.

Layers from 25-400 nm thick were deposited on FTO-coated glass and standard devices with no other window layer were subsequently fabricated (shown in Figure 3.11). Almost all the devices show excellent V_{OC} near 850 mV; however, some layers thinner than 50 nm show reduced V_{OC} . The window layers with higher magnesium produce a very strong kink in the J-V curve with only 100 nm thickness. At the optimal point of 50 nm, made with the 11 wt% magnesium oxide target, numerous devices with efficiency values of over 15% have been fabricated with no other HRT or window layer. This demonstrates use of a thin, resistive oxide layer which functions both as HRT and window layer when band alignment of the structure is preliminarily optimized. Like sputtered, oxygenated CdS (see Chapter 4), MZO is highly resistive and can create a conduction band spike,

and layers thicker than 50 nm cause a kink in the current-voltage curve; however MZO does not require a separate HRT layer and can be directly deposited on fluorine-doped tin oxide. The J-V curve of the best device in this limited optimization study is shown in Figure 3.12

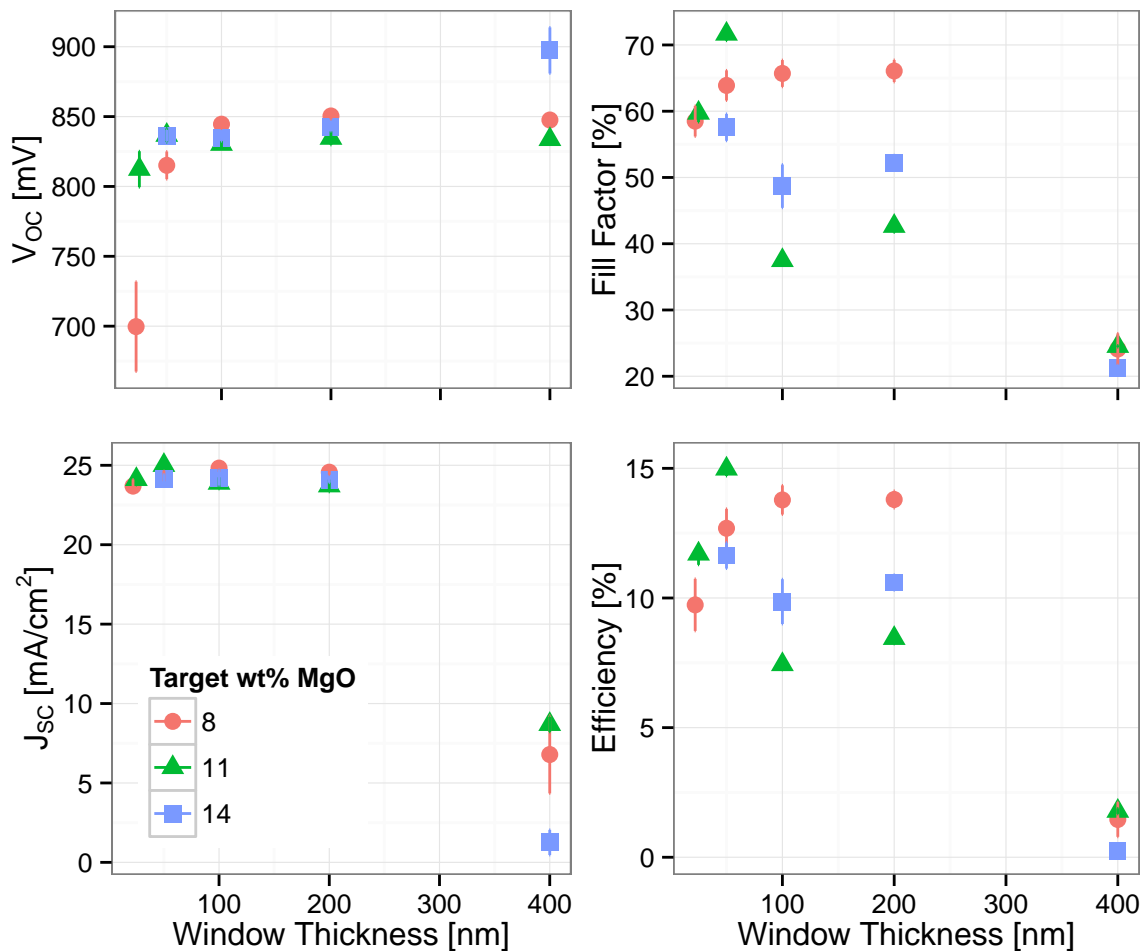


FIGURE 3.11. Device parameters are shown for devices made with (Zn,Mg)O window layers on NSG TEC 10 glass with no other window layer. The high-magnesium window layers see more of a kink with higher thickness, corresponding to a drop in fill factor.

3.5. DISCUSSION

A commonly mentioned but incomplete theory is that pinholes leading to oxide/CdTe junctions cause weak diodes which “shunt” current away from strong CdS/CdTe diodes. This theory has not been justified by experimental evidence at CSU since cells have not shown increasing pinhole area

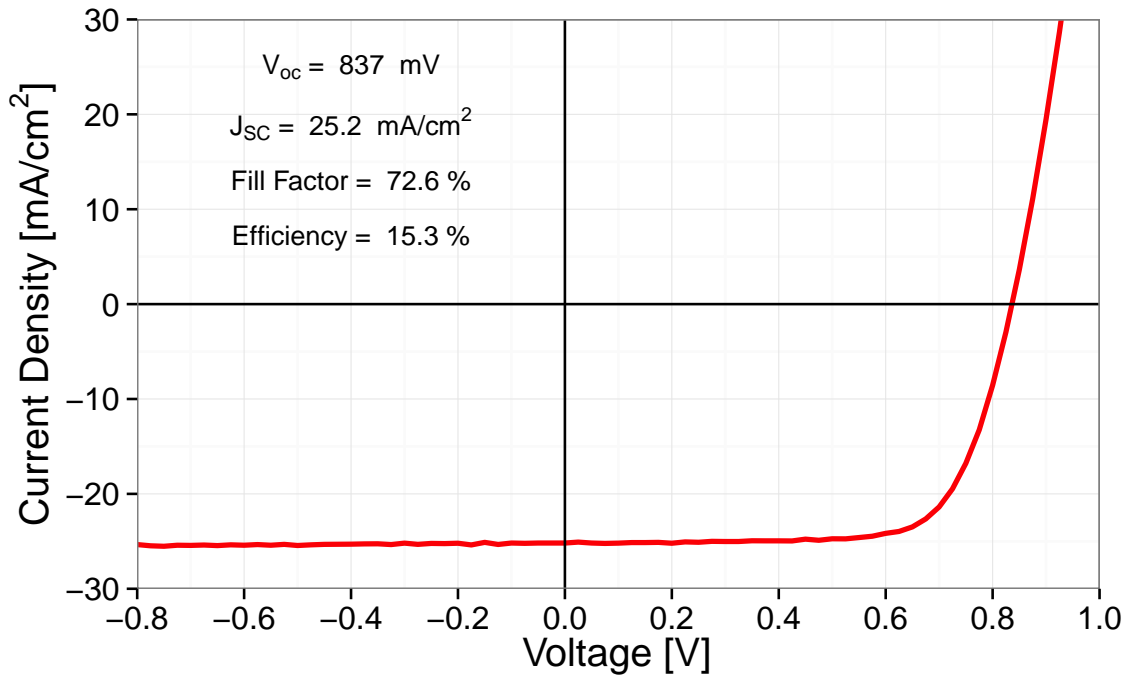


FIGURE 3.12. The J-V curve and device parameters of the best device shown in the (Mg,Zn)O thickness-composition optimization.

with thinner window layers. Furthermore, pinholes do not seem to have as large an effect on device efficiency as a naïve parallel diode model would suppose [45]. This theory also does not explain *why* the oxide/CdTe junctions are weak.

One theory that holds true for single crystal, epitaxially-grown devices is that the lattice constant between the absorber and underlying material must match closely in order to provide a good growth template, which will minimize defects in the material. In single crystals, strain due to mismatch is relieved by the creation of threading dislocations which continue through the entire thickness of the material. In polycrystalline materials, there is already a relatively high concentration of interface defects, and strain can be relieved at grain boundaries. Since (Zn,Mg)O has a much lower lattice constant than CdS (and the same crystal structure), it possesses greater mismatch to CdTe and would not produce a high-quality device if lattice matching were a paramount

consideration. Thus, the lattice constant of a material does not seem to be the driving concern of front contact quality in these polycrystalline thin film devices.

As an alternative, understanding begins by considering the poor quality of a TCO/CdTe junction, and what is necessary to correct the problems with this junction. The band alignment and interface recombination velocity of a semiconductor interface are in general very complex and difficult parameters to predict perfectly from theory. The evidence collected by fabricating numerous devices, extensive device and materials characterization, and modeling, suggests that band alignment is a key consideration in the design of CdTe thin-film solar cells. Like a conduction band cliff, degenerate doping of the TCO reduces the activation energy for interface recombination between the window and CdTe layers.

Failure of light-dark superposition is a fairly common phenomenon seen in thin-film solar cells. This has been explained as a conduction band “spike” between the absorber and CdS that is slightly reduced due to photoconductivity in the CdS layer [58]. This explanation does not suffice for a cell in which an oxide contacts CdTe directly; also the front contact does not show spectral dependence between red and blue light. Under this theory, window layer photoconductivity is increasing the depletion width in the absorber and therefore affecting the charge in the window layer. Without any window layer, charged defects at the TCO/CdTe interface rather than charged defects in the CdS can explain the effect.

The band alignment of the SnO₂/CdS interface has been investigated both by progressive growth of CdS [59] and by sputter depth profiling [60]. It was reported that the offset at this interface was $\Delta E_C = -0.1$ eV. This was measured after the full thickness of CdS was deposited and not immediately at the interface. The authors observed the Fermi level to be well below the conduction band in the CdS resulting in a total barrier height of 0.4 eV. Klein reports that there is a wide variation of more than 1 eV in the work function of SnO₂, which cannot be accounted

for by a difference in doping [61]. An effect similar to that of an HRT has been demonstrated simply by plasma treatment of the TCO, which only effects a few nanometers of the surface [62]. An earlier study by Niles *et al.* reported a flat conduction band at the interface [25]. However, recent studies of fluorine-doped tin oxide report a much higher work function than previously used in CdTe thin-film modeling, up to 5 eV [63]; if true, then a CdTe heterojunction with FTO would create a “cliff” alignment. Furthermore, because FTO is degenerately doped, the conduction band minimum is reported up to 0.6 eV below the Fermi level [63], and pinning of the CdTe CBM at the TCO Fermi level would further reduce the energetic barrier to interface recombination.

3.6. CONCLUSION

Pinholes do not seem to be the primary cause of effects seen relative to window layer thickness. The existence of a wurtzite (Mg,Zn)O window layer that can produce a high open-circuit voltage without CdS, but has a larger lattice mismatch with CdTe, implies that lattice matching is not a key factor for producing an effective front contact to CdTe—the interfacial defect density likely entails much more than this.

While sparsely explored in CdTe literature, the importance of band alignment at the front contact has been well explored and confirmed in Cu(In,Ga)Se₂ thin-film solar cells. The weakness of the TCO/CdTe diode appears to derive from high electron affinity of the TCO, in large part to charged defects at the TCO surface. These cause a strong light-sensitive barrier to form in addition to the poor device properties in TCO/CdTe junctions. HRT layers, which are not degenerately doped, can have a wide range of effectiveness in improving contact properties. The SnO₂-based HRT layers shown here may themselves have varying densities of surface charge that can be mitigated with certain alloying agents but not others. This effect shows up both in processed devices and band alignment measurements of the clean free surface by photoelectron spectroscopy. In the

case of very poor band alignment between oxide and CdTe, CdS-based window layers that are very thin or have low carrier concentration do not produce high-efficiency devices; however, the ability of a thin, 50 nm layer of (Mg,Zn)O with very high resistivity to correct all the problems with the TCO/CdTe interface implies that this material can passivate the charged defects. In short, band alignment concerns appear to explain interface phenomena where existing theories based largely on window layer pinholes or lattice matching fall short.

CHAPTER 4

OXYGENATED CADMIUM SULFIDE¹

4.1. INTRODUCTION

CdTe thin-film photovoltaics have achieved a multi-gigawatt/year level of production due to low manufacturing cost. A large portion of installed photovoltaic costs go to direct materials and balance of system costs [14]. Many of these costs scale with the number of panels and not the total power output, so improving module efficiency is an important way to reduce overall system cost. A major conversion loss in laboratory cells as well as commercial modules is due to absorption of blue light in the CdS window layer [64]. The CdS layer strongly absorbs photons with energy greater than its bandgap of 2.4 eV, and light absorbed in this layer is not collected.

Numerous approaches have been examined to reduce this loss. Blue conversion losses can be reduced by decreasing the thickness of the CdS window layer; when too thin, the open-circuit voltage and fill factor are reduced [39]. The minimum CdS thickness required for optimum cell efficiency can be reduced via addition of a high-resistance transparent (HRT) layer [65] between the TCO and window layer. This effect has been optimized using a SnO₂-based material that can be deposited in a float glass manufacturing line [45]. A similar approach uses surface modification of the transparent conducting oxide (TCO) [62]. Using the thinnest possible CdS layer requires a compromise between current collection and other device parameters for highest efficiency. With these approaches, the optimal thickness of CdS still results in significant optical losses. Another completely different approach is to apply a polymer sheet to the front surface of the cell or module

¹This chapter was adapted from a peer-reviewed journal article: J. M. Kephart, R. M. Geisthardt, and W. S. Sampath. "Optimization of CdTe thin-film solar cell efficiency using a sputtered, oxygenated CdS window layer," *Prog. Photovolt: Res. Appl.*, 2015.

J. M. Kephart: Wrote the manuscript, designed experiments, fabricated devices, and performed materials and device characterization.

R. M. Geisthardt: Performed device characterization and edited the manuscript.

W.S. Sampath: Served as Principal Investigator.

which contains a luminescent downshifting dye [66]. This converts high-energy photons to an energy lower than the CdS bandgap, some of which are absorbed by the CdTe. To date, this approach has only improved blue response by 16% [67]. Other limitations of luminescent downshifting include an addition to the module bill of materials and stability concerns related to placing polymer film on the front surface of the module.

The loss from window layer absorption can also be reduced by using a window material with increased band gap. Alloys such as (Cd,Zn)S have been tested but have thus far resulted in low open-circuit voltage, and phase segregation issues have been reported [68, 39]. In an MOCVD process, Kartopu *et al.* were able to increase the voltage and current of devices with addition of Zn to the window layer, but open-circuit voltage remained low at 710 mV [69].

Radio-frequency sputter deposition of cadmium sulfide in the presence of oxygen has been shown to produce an alloy material with a greatly increased bandgap. Wu *et al.* first produced this material, and measured structural, optical, and electronic properties of the material. Oxygenation results in a reduction in grain size to create a nanocrystalline or amorphous film. The resistivity was observed to increase drastically with increasing oxygenation [70–72]. X-ray absorption fine structure analysis (NEXAFS/EXAFS) on this material has shown that the oxygen is largely bonded to sulfur as SO_3 and SO_4 but it is claimed that there are oxygen-free CdS nanocrystals [73].

Oxygenated CdS produced for this work has similar properties to those reported by Wu *et al.*, as reported in previous work [74]. XPS measurements indicate that SO_3 and SO_4 peaks are present. Asaba *et al.* saw amorphous films and XPS peaks were attributed to CdSO_4 , CdO_2 , and CdS [75], and Gupta *et al.* saw glancing-angle x-ray diffraction (GAXRD) peaks disappear as oxygenation increased [72]. Material produced at CSU shows that peaks disappear in GAXRD as higher oxygen flow is used, and peaks do not appear when the films are annealed to 500°C , in agreement with others' previous work [74].

Wu *et al.* reported devices using oxygenated CdS with AM1.5G conversion efficiency of 15.5% using a cadmium stannate/zinc stannate TCO/HRT stack on borosilicate glass. CTO/ZTO layers lead to devices with reduced stability relative to tin-oxide based front contacts [76]. These studies provide information about the film material properties and prove the feasibility of making high-efficiency CdTe solar cells with this window layer. Gupta *et al.* made an initial attempt to apply this material to commercial-type substrates but could not produce an increase in current density without a corresponding drop in open-circuit voltage and fill factor [72]. Little information regarding the key considerations of incorporating this material into a device structure has been published, and this work expands on previous research by systematically exploring the process space for repeatable device performance using commercially relevant substrates.

A cell must not only demonstrate high efficiency in the laboratory but also withstand environmental stress to maintain field performance. Accelerated lifetime testing (ALT) simulates years of stress in the field due to elevated temperature, light exposure, and bias conditions. At open circuit and under illumination the electric field in the device is weakened, and high temperature accelerates diffusion [77]. In CdTe cells, copper migrates primarily through the CdTe grain boundaries, to the CdS/CdTe interface, and into the CdS [78]. A primary degradation mechanism identified in CdTe solar cells is due to transient ion diffusion of copper from the back contact. Controlling the total dose of copper in the devices is vital to achieving proper stability [29]. No published information on stability issues of oxygenated CdS window material in CdTe devices exists. Due to the large change in material properties relative to typical CdS window layers and the role of the window layer in copper-related stability issues, this is a key consideration in studying oxygenated CdS.

4.2. EXPERIMENTAL

4.2.1. SUBSTRATE AND WINDOW LAYER. Substrates are 3.2-mm soda-lime glass (PPG Industries, Inc.) coated with $10 \Omega/\square$ fluorinated tin oxide; this coating was deposited in-line at the glass factory. A SnO_2 -based HRT layer was deposited with a laboratory coater by PPG Industries using a float-compatible process. Glass was cleaned by sonication in a 1% solution of Micro-90 followed by deionized water. Because the window layer was deposited at room temperature, substrates were thermally cleaned by heating to approximately 600°C prior to sputter deposition and allowed to cool under vacuum. Without this thermal cleaning step, delamination at the oxide/window interface is observed after the CdCl_2 treatment.

Small-area devices were made using oxygenated CdS window layers with different levels of oxygen incorporation. Radio-frequency sputter deposition of CdS took place at 15 mTorr using 60 W of power on a 10-cm diameter planar magnetron CdS target. The target-substrate distance was 9 cm. Oxygen was controlled as a percentage of argon flow during deposition by two mass flow controllers. The substrate was not heated during deposition. The sample was moved directly to the ARDS without storage. Because the sublimated CdS process step is omitted, the substrate is heated to the typical CdTe entrance temp of $480\text{-}500^\circ\text{C}$. Other than this, processing of cells with sublimated CdS and oxygenated CdS is identical.

4.2.2. MATERIALS AND DEVICE CHARACTERIZATION. Transmission measurements of coated substrates were performed on a Cary 500 spectrophotometer. XPS measurements were performed on a PHI 5800 with a monochromated Al $K\alpha$ source. Current-density/voltage (J-V) curves were measured using a Keithley 2420 SourceMeter and one of two solar simulators using a high-pressure

xenon arc lamp. Current was calibrated to a cell measured at the National Renewable Energy Laboratory (NREL) and one cell was sent to NREL for efficiency verification. Procedures for measuring quantum efficiency have been previously described [74].

4.2.3. ACCELERATED LIFETIME TESTING. Various cells were held at 65°C for 1000 hours at open circuit with an illumination of approximately 0.7 suns. These conditions are used by industry [29, 79]. While under stress conditions, cells were sealed in air with desiccant. Some cells had been stored for up to two months in laboratory conditions (25°C, room light, open circuit, in a sealed container of desiccated air) between the initial measurement and beginning of stressing. The devices were removed weekly and tested at room temperature, then returned to the test apparatus. Afterward the devices were stored in the dark at room temperature for several hundred hours to examine the reversibility of degradation.

4.3. RESULTS

4.3.1. OPTICAL TRANSMISSION. Films were deposited with varying oxygen content onto substrates, and steps were etched, then measured by profilometry to establish deposition rates. A second series of samples was produced with deposition times adjusted to produce a thickness of 100 nm, and the optical transmission was measured. The films were then heated to the maximum device processing temperature of 500°C in the ARDS, cooled, and measured again. Transmission over the relevant wavelength range is shown in Fig. 4.1 for as-deposited and annealed films. As deposited films show a steady increase in band gap, and above 2.0% no absorption edge can be seen out to 300 nm. For oxygen flow at or below approximately 2.0% of argon, the band gap is comparable to that of CdS. Films made at a setpoint above 2.0% do not show this drop in band gap, and no absorption onset can be seen out to 300 nm wavelength. Since films must be annealed in the device manufacturing process, the behavior of annealed films is of most interest. The sudden

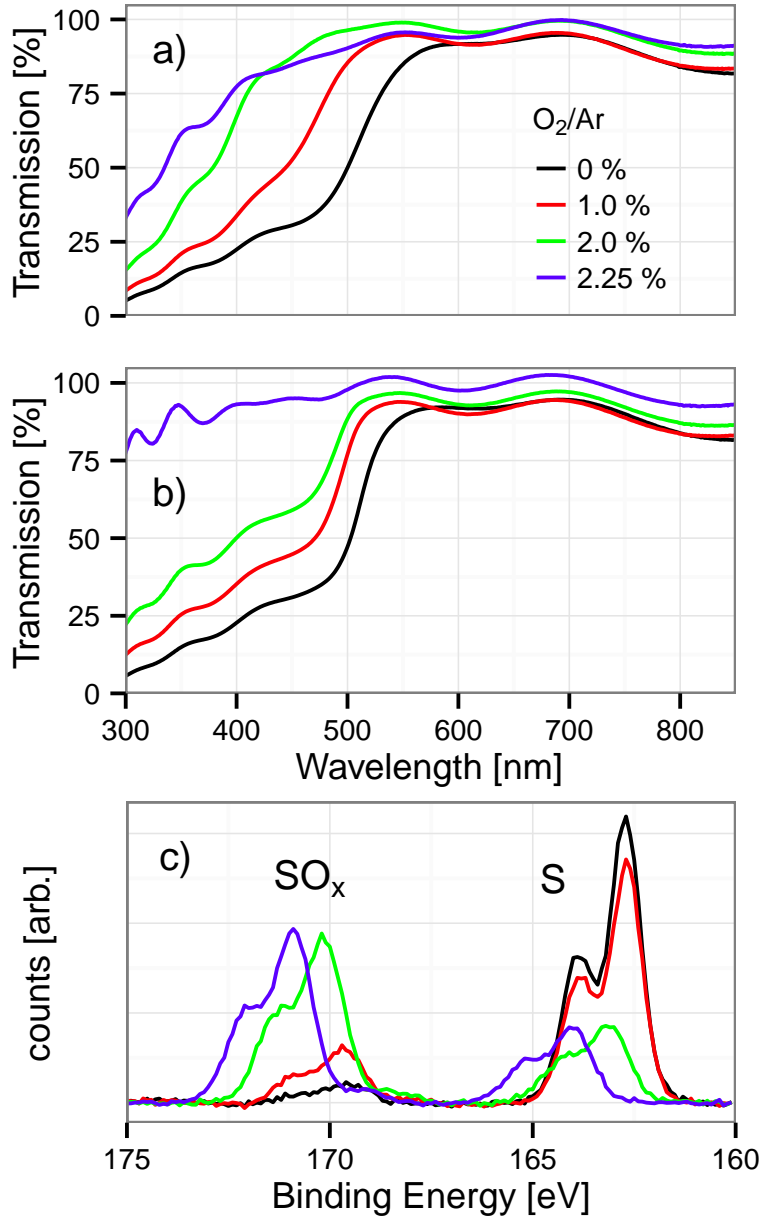


FIGURE 4.1. Transmission is shown with the SnO₂:F-coated glass substrate as a 100% reference. a) Transmission below 500 nm improves with oxygenation for as-deposited films. b) The same films annealed at 500°C below a critical oxygenation value gain CdS-like absorption. c) XPS measurement of the S2p peak for annealed films show this transition is not accompanied by a drastic change in SO_x content.

change in transmission with oxygenation means that the band gap of this material as a function of oxygenation is not readily determined.

4.3.2. VARIABLE-ANGLE SPECTROSCOPIC ELLIPSOMETRY (VASE). Spectroscopic ellipsometry is a highly sensitive optical measurement technique that allows for measurement of the complex refractive indices of a thin film given its structure, or vice versa. Variable angle spectroscopic ellipsometry (VASE) measures the change in polarization of light reflected off a substrate which may be coated with one or more thin films. The light reflects off of each interface and interferes with itself in a way that is dependent on both the wavelength of light and the angle of incidence.

An ellipsometer consists of a source of polarized light, a detector capable of determining the polarization state of reflected light, and a goniometer which controls the angle and orientation of source, sample, and detector. The reflected light consists of two components r_s and r_p , which are parallel and perpendicular (*senkrecht*) to the plane of reflection. These components can also be in different phases to one another. The state of polarization of light can be completely described by an ellipse with the angle parameters ψ and Δ , thus the term *ellipsometry*. Since the data gathered from this technique is complex and not in itself meaningful, a model is generated using a series of thin films with their complex indices of refraction (with real component n and imaginary component ik , the extinction coefficient).

For well-understood films these can be taken from reference values, or can be modeled using a number of different oscillators. Some models such as Cauchy and Sellmeier are designed for transparent dielectrics, and work well for these types of films. These assume that $k = 0$ over the entire wavelength range. Other oscillators model the above-bandgap absorption of semiconductors, and n is calculated by the model using the Kramers-Kronig relations.

To measure the complex refractive indices of oxygenated CdS, layers were deposited on uncoated soda-lime float glass, which has a very small roughness of less than 1 nm. The target thickness of layers at each composition was 100 nm, and actual thickness was measured by profilometry

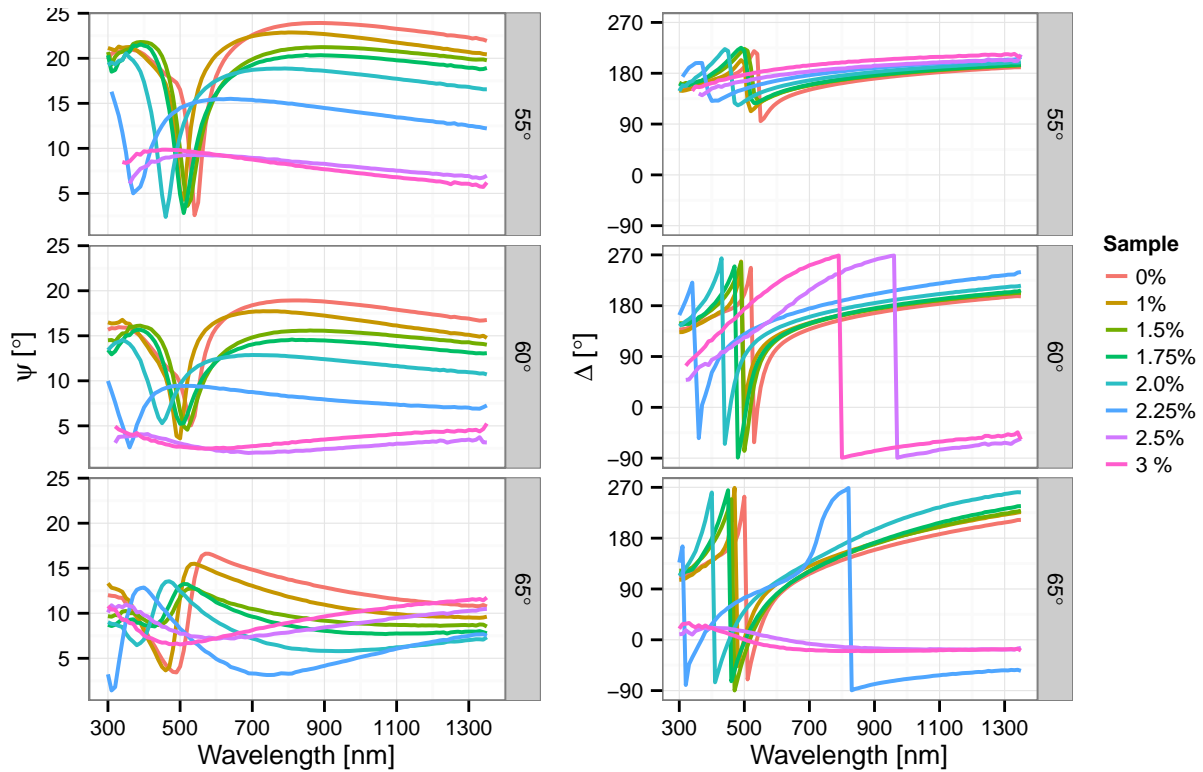


FIGURE 4.2. The parameters ψ and Δ are shown as function of wavelength at an angle of incidence of 55, 60, and 65° from normal. A trend with oxygenation is apparent.

of an etched step in the layer near to where the optical measurement was taken. Measurements were made at wavelengths of 300-1350 nm and angles of 55, 60, and 65° using a VASE instrument (J.A. Woollam Co.). Figure 4.2 shows the unprocessed output of the ellipsometry measurements, which exhibit a clear trend with oxygen content.

To process the raw data into an estimate of the refractive indices, an oscillator model was developed in the WVASE32 software (J.A. Woollam Co.) to reduce the number of free parameters and create a physically realistic model. For soda-lime glass, a Cauchy model fit to reference optical parameters [24] was used and remained fixed for all samples. The interface between glass and oxygenated CdS was assumed to be smooth. The CdS material used several oscillators which matched n and k of reference CdS data. An effective media approximation was used to model a roughness layer. Initially, the thickness was fixed at the physically measured value, and the optical

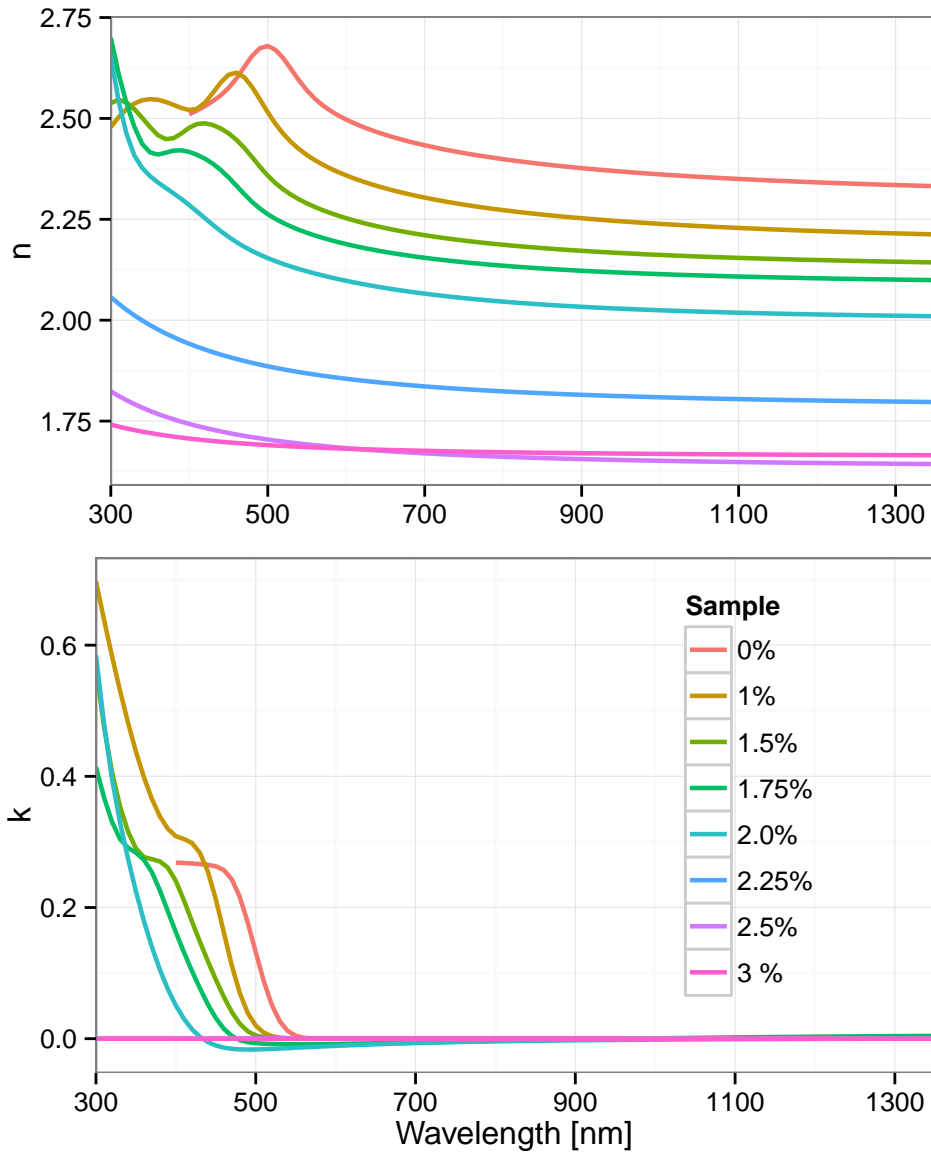


FIGURE 4.3. A fit of an optical oscillator model to ellipsometric data shows a reduction in optical absorption with increasing oxygenation, as well as a drop in real refractive index n

properties were fit. Then, film and EMA thickness values were allowed to vary. For high oxygen content films, it was found that for films made at 2.25, 2.5, and 3.0% O_2/Ar , a Sellmeier model produced good fits to the data, since there was no significant optical absorption over the spectrum examined.

The results of the fit in Figure 4.3 show a clear pattern. First of all, the 0% sample shows typical direct-gap semiconductor dispersion properties, with a sharp rise in extinction coefficient k above

TABLE 4.1. Layer thickness results from a model fit to VASE data show that layer and EMA thickness measurements are in general agreement with profilometry and AFM measurements, respectively. The 3.0% film shows a large discrepancy. AFM peak-to-peak roughness is shown for reference

% O₂/Ar	Profilometry [nm]	VASE [nm]	VASE EMA [nm]	VASE EMA void [%]	AFM [nm]
0	105	101	18	25	13
1.0	110	105	10	50	21
1.5	105	120	2	50	4.8
1.75	120	122	2	50	5.6
2.0	110	113	3	50	2.5
2.25	125	108	6	50	4.3
2.5	100	115	0	-	2.0
3.0	138	83	0	-	2.2

the bandgap (below 500 nm wavelength), and a gradual increase in k at lower wavelengths. The real refractive index n shows a peak at the bandgap. With increasing oxygenation, the bandgap moves to lower wavelengths; the slight negative values of k are probably not physical. With a decrease in optical density of states n steadily decreases with oxygenation, and this becomes more pronounced above 2.0%. At these high oxygenation values the material has very typical dielectric-like dispersion properties. In general, the thickness values of best fit are approximately correct within the error of film uniformity, profilometer precision, and simplifying assumptions in the ellipsometry model. The 0%, crystalline sample had higher roughness and the percent of void in the EMA layer had to be allowed to vary to produce a good fit. The 3.0% sample had a large discrepancy in thickness between the physical and optical measurements, and did not show the continuing decrease in n ; it is possible this is due to the similarity in refractive index between the film and the glass substrate, which would make accurate measurement and modeling much more unlikely. The structural measurements are summarized in Table 4.1.

4.3.3. ATOMIC FORCE MICROSCOPY. A group of characterization techniques known as scanning probe microscopy use small probes with extremely sharp tips to interact with the surface of a

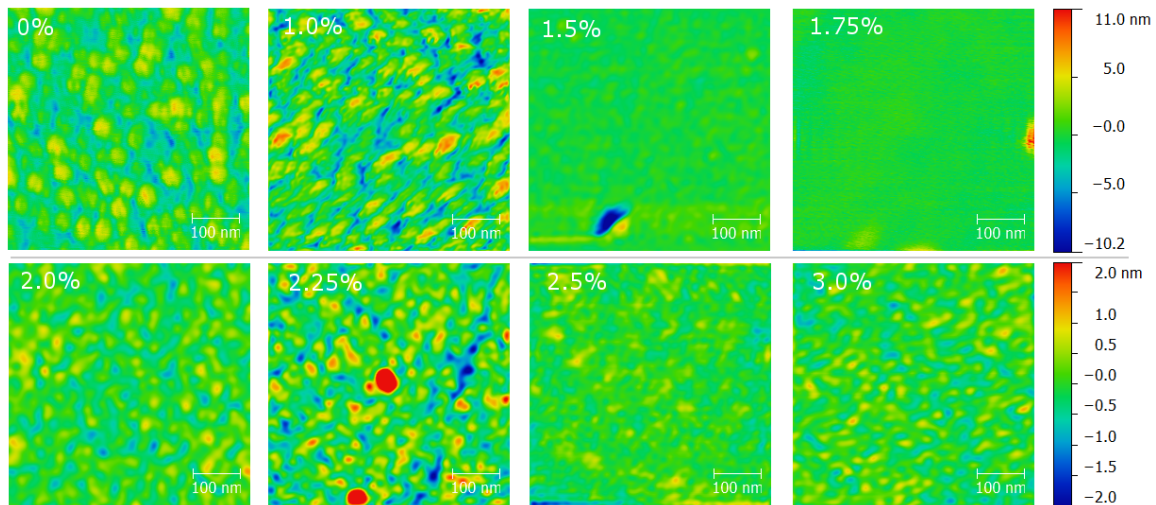


FIGURE 4.4. Atomic force microscopy shows the polycrystalline nature of non-oxygenated CdS. With increasing oxygen the films become smoother, with some isolated asperities. Note that each row has its own height scale.

material. In atomic force microscopy (AFM) the tip is placed on a cantilever beam made via micro-fabrication of silicon. As this tip is moved near contact with the surface under study, a deflection is measured with high precision via the reflection of a laser off the cantilever. This technique is very sensitive to ambient vibration and the apparatus is placed on an isolation table with a cover to keep the air inside still.

AFM was performed on the same oxygenated CdS samples that were used for ellipsometry measurements in order to corroborate roughness results. For each ellipsometry sample several 500 x 500 nm scans were recorded until a good quality image was produced for each sample using an EasyScan 2 (Nanosurf). Lateral resolution is approximately 2 nm. Noise for the depth dimension was below 1 nm, but many samples had RMS roughness values only slightly larger than this. Leveling, scar correction and low-pass filtering were used in the Gwyddion program to create a clearer image. Figure 4.4 shows the reduction in roughness with increasing oxygen concentration. In the region of interest for devices, the films are all very smooth and appear to have no visible crystalline structure. Roughness values are all small and agree qualitatively with ellipsometry data.

These data support the physicality of VASE measurements and the amorphous nature of the films with higher oxygen content as evidenced by GAXRD.

4.3.4. MATERIALS CHARACTERIZATION. Materials analysis indicates that the material is primarily an alloy of CdS and CdSO₄, with smaller amounts of CdSO₃ and CdO [80]. XPS clearly shows that the S2p sulfide peak is reduced and a higher binding energy state is increased with oxygenation; the authors have attributed this to the presence of CdSO₃ and CdSO₄ [74]. XPS results shown in Fig 4.1c do not indicate a sudden change in $[\text{SO}_x]/([\text{S}] + [\text{SO}_x])$ composition between the 2.0% and 2.25% setpoints. Though little optical information has been published about these sulfate and sulfite materials, they are ionic salts with very high band gap; alloying of these materials with CdS could explain the increased band gap relative to CdS. Soo *et al.* interpreted the material as sulfur-oxygen complexes with oxygen-free CdS nanocrystals. A possible explanation for the reduction in band gap of intermediate-oxygen films upon annealing is that oxygen-free domains segregate upon annealing, which does not happen for higher oxygenation levels.

Measurements were performed on samples before and after heat treatment using a Bruker D8 Discover Diffractometer at an angle of $\alpha = 0.5^\circ$. Fig. 4.5 shows that the two films lowest in oxygen show clear peaks, indicating a crystalline material. The 1.0%, 1.5%, and 2.0% O₂/Ar films show very weak, broad peaks, indicating very small grains. The film with highest oxygen incorporation shows no peak.

Upon heat treatment, films with intermediate oxygen incorporation show a slight increase in peak height, which could indicate partial crystallization of the wurtzite phase from amorphous material. It is known that SO₃²⁻ and SO₄²⁻ ions are present in this material [73]. CdS electrons have an exciton Bohr radius of 6.8 nm and grain sizes must be below this to see significant confinement effects [81]. It is thought that alloying of CdS with CdSO₄ stabilizes the amorphous phase, which has a higher bandgap than CdS. A similar phenomenon has been observed in room-temperature

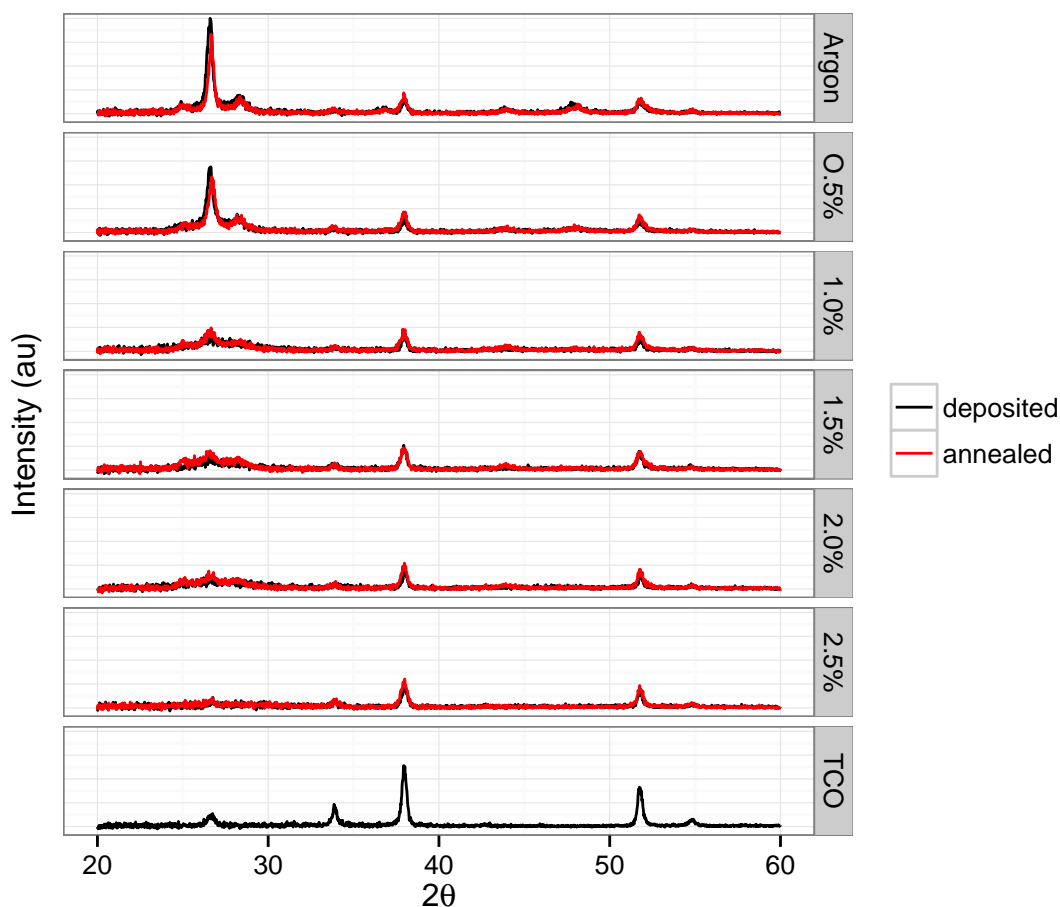


FIGURE 4.5. GAXRD shows a decrease in crystallinity with increasing oxygen incorporation. Films do not recrystallize significantly upon high-temperature annealing. Adapted from Reference [45].

sputter deposition of the $\text{In}_2\text{O}_3\text{-ZnO}$ and $\text{SnO}_2\text{-ZnO}$ systems, where crystal growth is inhibited by the presence of two components that crystallize in different phases [82].

4.3.5. DEVICE CHARACTERIZATION. Devices made in the ARDS with sublimated CdS are typically made with 3.2 mm NSG TEC 10 substrates with no HRT layer. Initial attempts to use oxygenated CdS on these substrates resulted in devices with good current collection but poor open-circuit voltage. An HRT layer made by PPG Industries was optimized to maximize the efficiency of a device made with sublimated CdS [45]. This layer was found necessary for high V_{OC} with

oxygenated CdS window layers. The necessity of the HRT was repeatedly verified, with comparable devices made directly on FTO showing a typical V_{OC} of 500-600 mV and consistently greater than 810 mV with HRT. The optimized HRT layer was used for further window layer optimization.

Devices were made starting with standard 130-nm window layers. Oxygenation was varied from 0% to 3.0% O_2/Ar , and two clear, consistent trends emerged (curves are shown in Fig. 4.6a). From 0 to 2.0% O_2/Ar , the diode properties improve, with higher V_{OC} and less voltage-dependent current collection, which leads to improved fill factor. In general, CdS deposited at room temperature with no oxygen produces poor devices. Layers with less than about 1.5 to 2.0% oxygen all produce a quantum efficiency similar to the 0% device as shown in Fig. 4.6b. At 2.0% O_2/Ar , the blue collection increases dramatically, which corresponds to an increase in short-circuit current. There appears to be an optimum in efficiency between 1.5% and 2.5% O_2/Ar . The improved quantum efficiency agrees with optical transmission of the window layers as well as short-circuit current; as with transmission measurements of annealed samples, a steady increase in window layer band edge is not observed. Rather, the quantum efficiency suddenly changes from CdS-like to highly transparent in the blue region, although at a slightly different O_2/Ar value than seen for the transmission data.

The second trend occurs above 2.0%, as a kink appears around V_{OC} leading to reductions in fill factor. As the kink becomes more pronounced the fill factor is reduced dramatically and short-circuit current is affected. This causes the quantum efficiency to drop across the entire spectrum. Choosing the ideal process parameters of the window layer requires a sufficiently high oxygen setpoint for improved transmission and V_{OC} , while minimizing the kink in the J-V curve. One way to attain high current and voltage without a kink is to use a very thin, high-oxygen window layer. Fig. 4.6c shows that reduction of thickness of 2.5% O_2/Ar window layers leads to near elimination

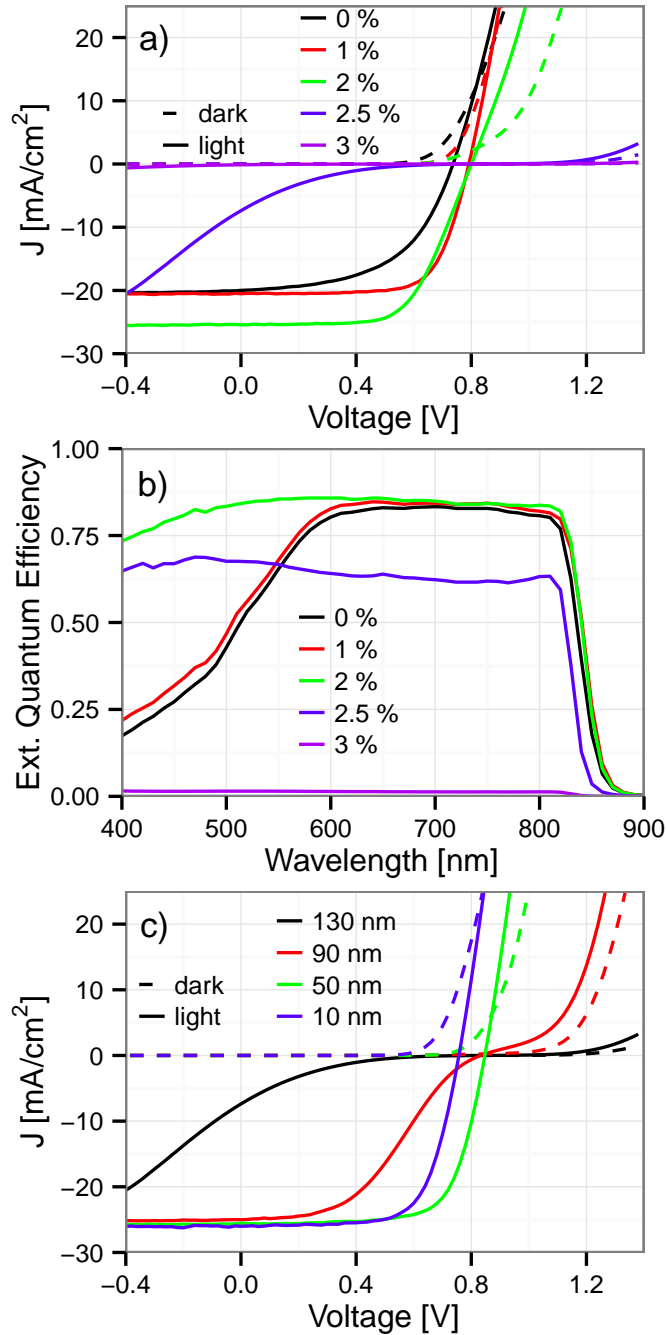


FIGURE 4.6. a) Devices with 130-nm window layers were fabricated with varying O₂/Ar. From 0% to 2% , short-circuit current, fill factor and open-circuit voltage improve. Above 2% O₂/Ar, a severe kink appears which reduces fill factor and short-circuit current. b) Quantum efficiency in the blue region shows a drastic improvement with higher oxygen, until collection is reduced due to the J-V kink. c) For films made with 2.5% O₂/Ar, the J-V kink can be reduced by reducing the window layer thickness.

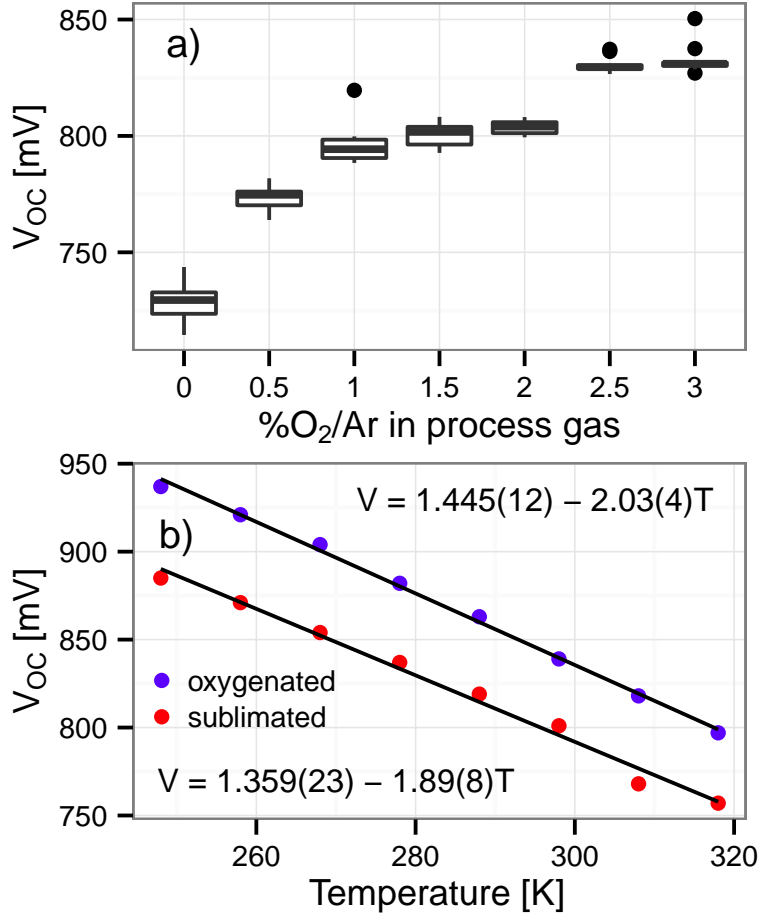


FIGURE 4.7. a) Devices (here with 130-nm window layers) show an increase in open-circuit voltage with oxygenation of CdS. b) An optimized device using oxygenated CdS has a significantly greater 0-K V_{OC} intercept than a device made with sublimated CdS and no significant difference in slope. Linear fits are shown with standard errors.

of the J-V kink while maintaining voltage and current. In this study window layers could be made as thin as 15 nm without loss of V_{OC} .

Open-circuit voltage continues to increase with higher oxygen as demonstrated in Fig. 4.7a. A commonly used expression for open-circuit voltage is shown in Equation 5. Ideality factor A and reference saturation current density J_{00} are indicative of recombination mechanism; if activation energy E_A is less than the absorber band gap, this could indicate a non-ideal band alignment [83]. The V_{OC} vs. T relationship can be extrapolated to 0 K in order to estimate the activation energy of the diode, while difference in slope could indicate changes in A and J_{00} .

$$(5) \quad qV_{OC} = E_A - AkT \ln \left(\frac{J_{00}}{J_{SC}} \right)$$

Current density-voltage measurements were performed with the device maintained at temperatures from 248 K to 318 K. These measurements, shown in Fig. 4.7b, indicate the E_A for the oxygenated films is approximately 1.45 eV which is roughly 0.1 eV higher than for devices made with sublimated CdS. A two-sided statistical test was performed to compare the parameters between the two linear fits [84]; the intercept is significantly larger ($p = 0.006$) while no significant difference exists between the slopes ($p = 0.14$). These results suggest that activation energy rather than a change in bulk recombination is responsible for the increased V_{OC} with oxygenated CdS versus sublimated CdS.

4.3.6. 1-D DEVICE MODELING. To model the effects of a changing conduction band offset at the window/absorber interface, 1-dimensional device modeling was performed in SCAPS [52]. Parameters were primarily taken from standard references [47] and are listed in Table 4.2. Neutral defects were used with a lifetime of 2 ns for the CdTe absorber. The window layer carrier concentration was reduced to 10^{16} cm^{-3} to account for the increased resistivity of oxygenated CdS and similar results are obtained for $n = 10^{15} \text{ cm}^{-3}$. Surface recombination velocity was set to 10^5 cm/s for electrons and holes at the window/CdTe interface. Absorption was ignored in the CdS layer and default absorption was used for the other layers. The electron affinity was modified in the model to create the desired window/absorber conduction band offset as seen in Fig. 4.8a. The bandgap was increased to keep the window layer valence band at the same position. The position of the window layer valence band is not important to the model since the valence band offset is already quite large, and optical effects of oxygenation were not modeled.

TABLE 4.2. 1-D modeling parameters used for SCAPS simulation of the conduction band offset effects.

Parameter	HRT	Window	CdTe
x [nm]	150	130	2500
E_G [eV]	3.6	varies	1.5
χ [eV]	4.5	varies	4.4
ϵ/ϵ_0	9	10	9.4
N_C [cm ⁻³]	$2.2 \cdot 10^{18}$	$2.2 \cdot 10^{18}$	$8.0 \cdot 10^{17}$
N_V [cm ⁻³]	$1.8 \cdot 10^{19}$	$1.8 \cdot 10^{19}$	$1.8 \cdot 10^{19}$
μ_e [cm ² /Vs]	1	100	320
μ_h [cm ² /Vs]	25	25	40
τ_n, τ_p [ns]	0.1	0.1	2
	HRT/Window	Window/CdTe	CdTe/Back
S_n, S_p [cm/s]	0	10^5	10^7

As seen in Fig. 4.8b curves are similar to experimental curves seen in Fig. 4.6. The effect of the conduction band offset on the J-V kink is clear. Series resistance starts to noticeably increase with a CBO of 0.3 eV, and the kink quickly becomes worse with further increases. Open-circuit voltage also increases slightly as the valence band offset increases, though the effect is smaller than for experimental devices. As the CBO varies from -0.1 eV to 0.4 eV, the V_{OC} increases from 824 to 842 mV. The highest CBO shown produced a very high V_{OC} which may be inaccurate due to the severe kink.

4.3.7. STABILITY. Devices made at different stages of the optimization were examined for degradation as shown in Fig. 4.9; each line shown represents an average of three cells. First, devices made with varying oxygenation were examined and oxygen content appears to correlate with decreased stability, primarily in fill factor, though films with lower oxygen have much lower initial efficiency. Second, devices made with 2.0% O₂/Ar (shown in Fig. 4.9b) were examined with varying window layer thickness. Finally, the copper dose was reduced using the previous high dose and two lower doses; the copper doses correspond to CuCl source temperatures of 210°C, 190 °C, and 170°C. These devices have very thin (less than 15 nm), 2.5% O₂/Ar window layers which are

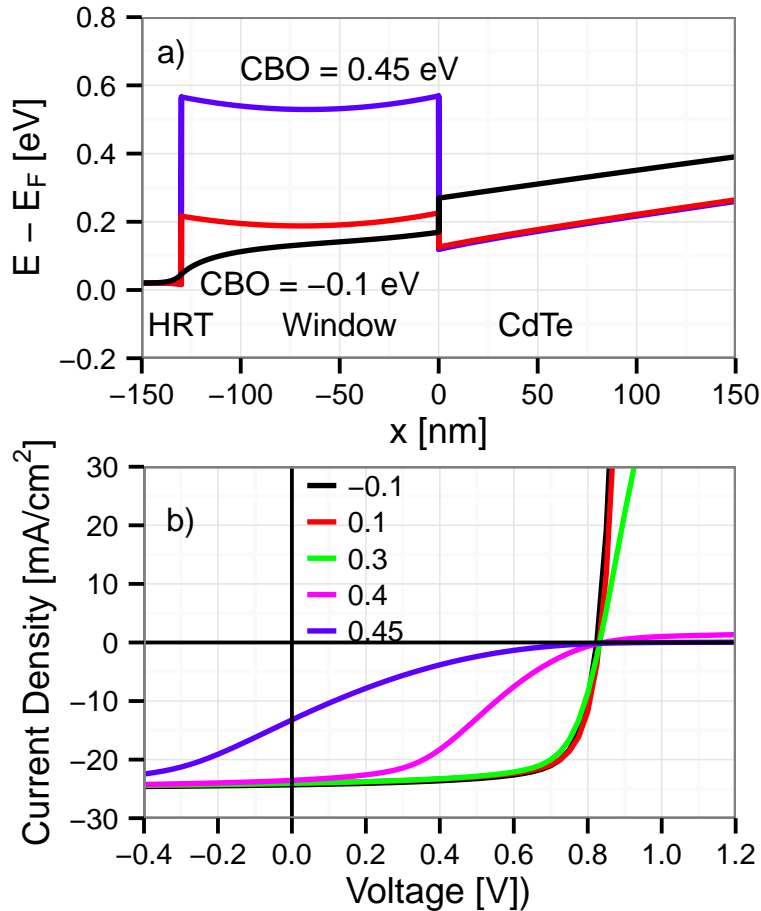


FIGURE 4.8. a) The band diagram of the front region of the solar cell is shown as the electron affinity of the window layer is varied. b) 1-dimensional modeling results when varying conduction band offset show similar behavior to experimental results when %O₂/Ar is varied.

very unstable and sensitive to copper. The “medium” dose has little difference in initial efficiency relative to the high dose, and is more stable. The “low” copper dose has lower initial V_{OC} and fill factor, but is most stable.

While very thin window layers made with high oxygen content have good initial efficiency, they suffer from very poor stability and do not recover from degradation. A thickness of 50 nm with a “medium” copper dose provides a balance of initial efficiency and stability. A finer study of oxygen content from 1.8% to 2.2% was performed using these parameters. The lowest oxygen content that provides high blue transmission (1.8% O₂/Ar) appears optimal. Since a simple carbon

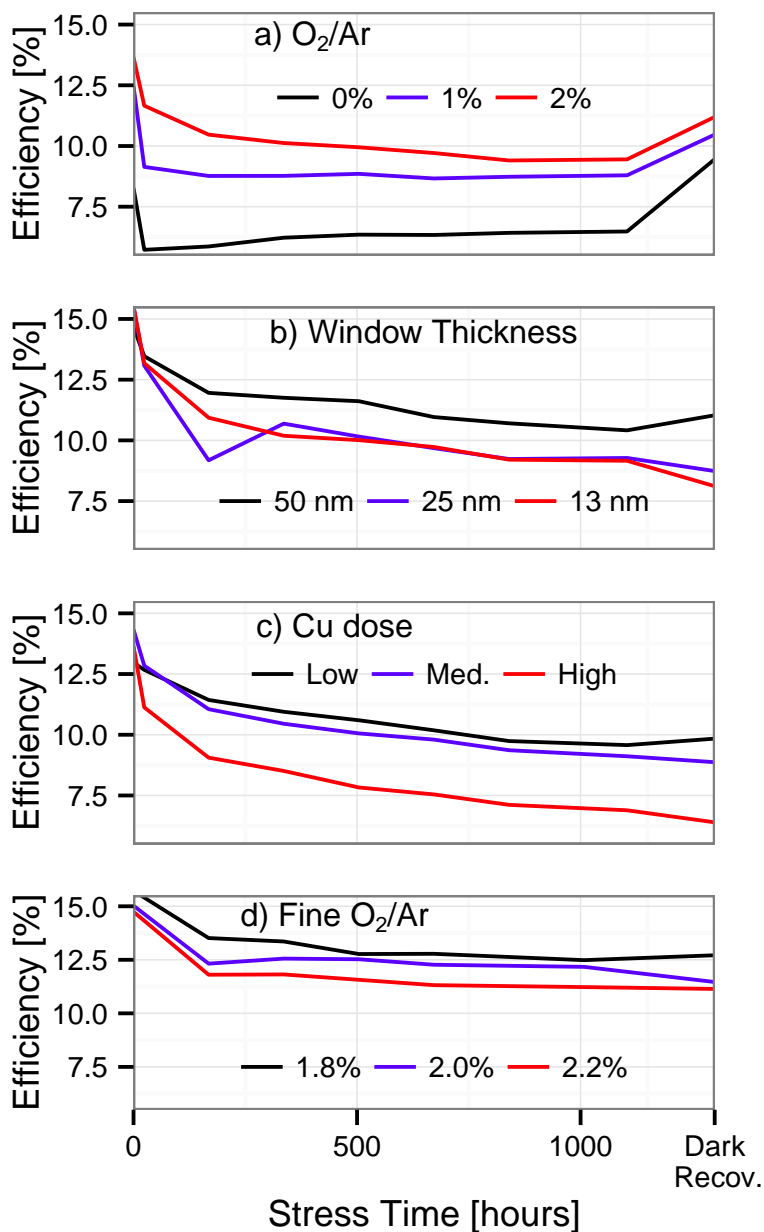


FIGURE 4.9. Accelerated lifetime testing results in a loss of efficiency. Devices that are stressed and allowed to recover respond differently based on a) window layer oxygen content, b) window layer thickness, and c) copper dose. d) Refinements based on preliminary results were used in a finer adjustment of window layer oxygen content.

paste is used to contact the CdTe, more advanced back contacts could lead to reduced copper migration and higher stability.

4.3.8. EFFICIENCY VERIFICATION. A cell made with optimized parameters that balance initial efficiency with stability was sent to NREL for efficiency verification. The cell shows an AM1.5G efficiency of 15.2%. This cell was measured using an aperture less than half the active area of the cell at a temperature of 30°C, which may account for differences in V_{OC} and fill factor from measurements performed by the authors. The J-V, quantum efficiency, and device parameters are shown in Fig. 4.10. The quantum efficiency reported by Wu *et al.* has a clear band edge due to the window layer at approximately 500 nm [71]. The cells reported here do not have such an observable band edge. For the 15.2% cell, the absorption edge seen from 300-400 nm is due to the commercial antireflective coating. The lower voltage and fill factor could be due to the lower temperature, high-throughput CdTe and CdCl₂ processes, as well as the paint back contact.

4.4. DISCUSSION

Devices with oxygenated window layers are much more sensitive to the presence of an optimized HRT layer than devices with sublimated CdS. With sublimated CdS, even with no HRT the open-circuit voltage and fill factor can be improved to reasonable values by using a thicker window layer. With oxygenated films even a thickness of 200 nm directly on a SnO₂:F TCO did not produce a V_{OC} of 800 mV, and the J-V kink is exacerbated by such thickness. With an optimized HRT, high V_{OC} can be obtained with very low thickness (less than 15 nm) and still shows little dependence on thickness. This phenomenon is believed to be due to the more ideal band alignment of the HRT/window interface because of the lower work function demonstrated by the HRT [45]. The reduced carrier concentration of the oxygenated window layer makes it impossible to correct an unfavorable band alignment by using larger thickness.

The effect of altering the conduction band offset of the window layer (called “buffer layer” for Cu(In,Ga)Se₂) has been explored for Cu(In,Ga)Se₂ thin-film solar cells. Minemoto *et al.* showed

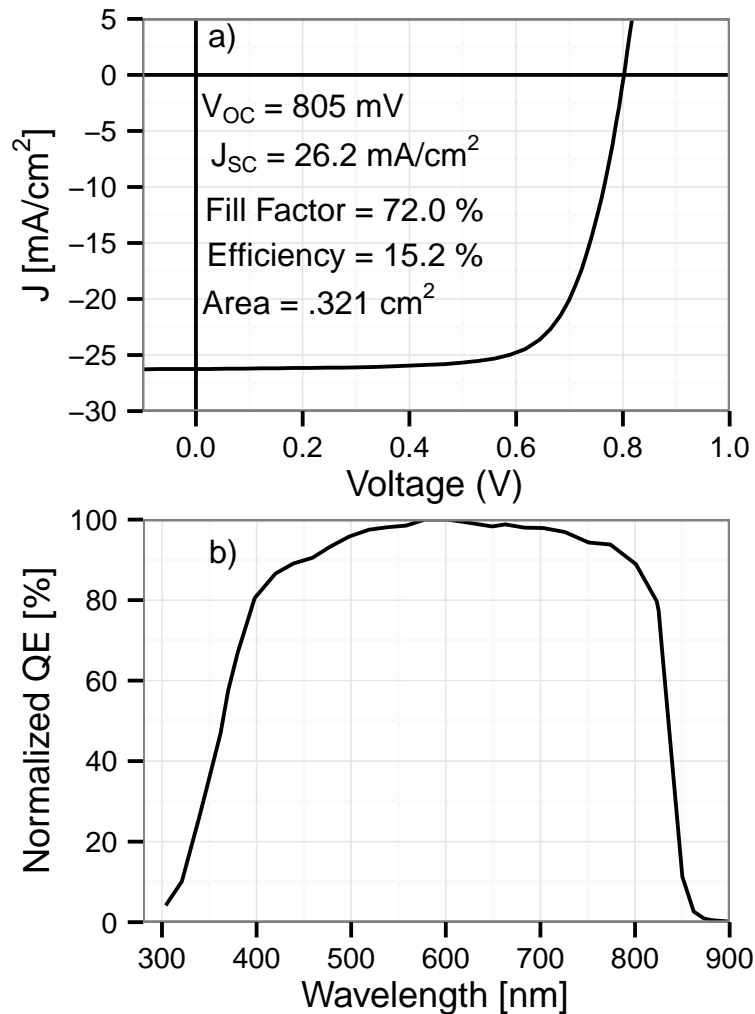


FIGURE 4.10. A device which represents a compromise of efficiency and stability was sent to NREL for efficiency verification; a) current-voltage and b) normalized quantum efficiency are shown. The cutoff in blue response is due to the commercial anti-reflection coating.

that interface defects could be more detrimental when the window layer electron affinity is higher than the absorber electron affinity, producing a negative conduction band offset, or cliff. Also, the activation energy of the diode is reduced by the magnitude of the cliff [83]. Adding a small “spike” by raising the window layer conduction band reduces these effects and improves device efficiency; if the spike is too large, barrier effects become detrimental to fill factor [85]. This was later shown experimentally using (Zn,Mg)O layers in Cu(In,Ga)Se₂ devices, which improved with an increase in relative magnesium concentration [86].

The reported conduction band offset between CdS and CdTe is close to zero, and the CdS conduction band may be 0.1 eV below the CdTe CBO (a “cliff”) [87, 88]. This is not ideal in the presence of defects at the interface, and Sites and Pan show via 1-D modeling that this effect can be significant even with low interface recombination velocities when the CdTe carrier concentration is low [19]. The conduction band offset for sputtered, oxygenated CdS appears to become more positive as oxygenation is increased. Using 1-dimensional modeling, this single change can explain both the J-V kink and the slight increase in open-circuit voltage. As the conduction band offset is increased from negative to positive, the activation energy of the diode can increase to near the band gap of the absorber. Above this, the conduction band of the window moves away from the Fermi level (pinned by the CdTe conduction band) and the concentration of electrons at the interface is reduced. In the presence of surface recombination this reduces the effective recombination velocity.

Another possible effect is the direct role of oxygen in passivating the CdTe interface. Oxygen in CdS has been shown to inhibit interdiffusion and improve devices at a few at.% [26]; these levels are present even for the films with no intentional oxygenation presented here. Device results from Fig. 4.7a showed that V_{OC} increases with oxygenation, then flattens out at approximately 800 mV for intermediate values, and again jumps when a J-V kink appears. Since oxygen at.% is very high (approximately 50%) even for intermediate oxygenation values due to the presence of SO_4 , this would likely be adequate for any passivation to occur. Rather, the V_{OC} phenomenon appears directly related to the band alignment at the window/CdTe interface, which is supported by modeling and temperature-dependent measurements.

4.5. CONCLUSION

Window layer absorption, a major cause of efficiency loss in CdS/CdTe solar cells, can be essentially eliminated using oxygenated CdS. This material is compatible with float-line deposited, SnO₂-based TCO and HRT layers. The bandgap of oxygenated CdS can be much greater than CdS, but increases suddenly at a critical level of oxygenation. Oxygenation also seems to provide more ideal, tunable band alignment at the front contact in conjunction with an optimized HRT layer that has resulted in devices with V_{OC} greater than 850 mV. In order to minimize current loss, achieve higher stability, and prevent adverse effects from a secondary barrier, the oxygen content and thickness of this layer must be chosen carefully.

CHAPTER 5

CONCLUSION

5.1. EVOLUTION OF FRONT CONTACT DESIGNS

The main focus of this work was to integrate new materials and structures into the front contact of working devices through the development of repeatable and controllable processes. This has been done in three separate stages. Figure 5.1 shows the evolution of device structures and the approximate maximum efficiency they produced. The first was to create a working HRT layer that could be deposited in a high-throughput process to enable a thinner layer of sublimated cadmium sulfide. Sputtered, oxygenated CdS was then incorporated, which requires an HRT for a device with good electronic quality but can be made transparent out to the absorption edge of the TCO layer. Based on the understanding and hypotheses related to front contact band alignment developed from these layers, (Mg,Zn)O was investigated as a tunable high-bandgap window layer. This material produces excellent devices without an additional HRT, which was a surprising result at the time given the necessity of the HRT with oxygenated CdS.

5.2. UNDERSTANDING OF THE FRONT CONTACT

At the outset of this work, the main understanding of the CdS window layer was as an n-type partner to the p-type CdTe absorber, which is needed to form a diode. It was not understood precisely why the TCO or any other given n-type material could not be an n-type partner, especially since the oft-cited value for its electron affinity implies that it should have favorable band alignment. The materials considered herein can be divided into five groups: 1) highly conductive fluorine-doped SnO₂, the TCO; 2) SnO₂-based alloy HRT layers which are less conductive; 3) sublimated CdS; 4) sputtered, oxygenated CdS; and 5) (Mg,Zn)O.

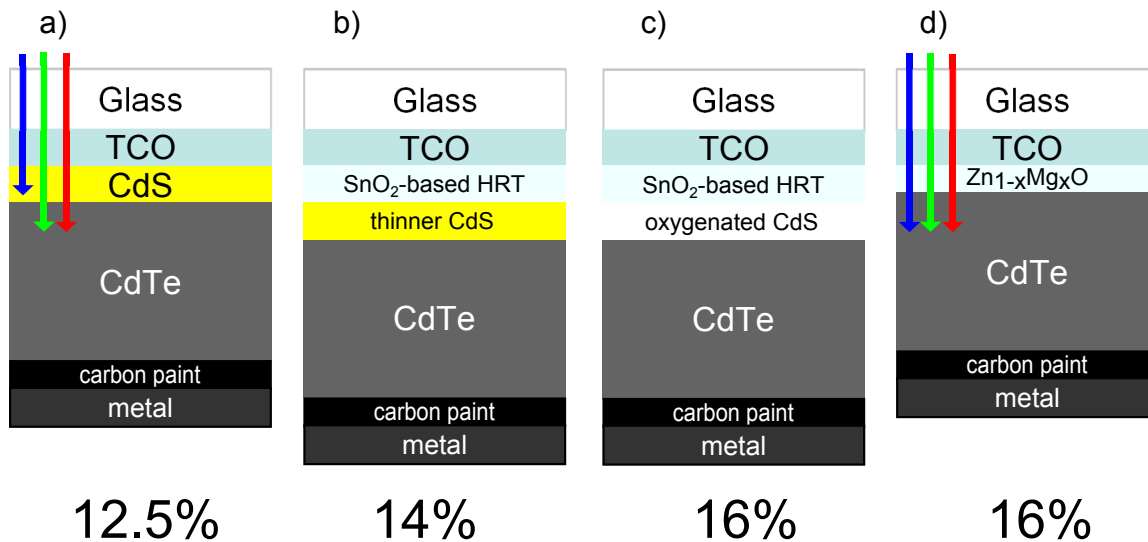


FIGURE 5.1. The evolution of the front contact has changed from a) a simple sublimated CdS layer between the TCO and CdTe, to b) an HRT layer with thinner CdS, to c) an HRT with sputtered, oxygenated CdS with near-complete transparency, to d) (Mg,Zn)O.

The FTO likely does not form a good contact for more than one reason. Pinning of the front CdTe Fermi level at the conduction band minimum would cause the overall barrier to interface recombination to be reduced. FTO has the least favorable band alignment of any of the SnO₂ materials examined by photoemission; this is likely due to charged surface states in addition to any bulk material properties. This appears to be partially corrected by some of the SnO₂-based HRT layers with intermediate carrier concentration. Further correction can be made by sublimated CdS, which has an intermediate carrier concentration and near-ideal band alignment with CdTe.

The oxygenated CdS has a very low carrier concentration, and requires an effective HRT in order to make strong diodes with maximal open-circuit voltage, fill factor, and efficiency. It can be tuned to have an appropriate conduction band offset, or an excessive positive offset which creates a pronounced kink in the J-V curve. (Mg,Zn)O is similar in many ways to oxygenated CdS – it has low absorption in the solar spectrum, its conduction band position (and bandgap) can be tuned by changing its composition, it has very low carrier concentration. These characteristics allow for fabrication of high-efficiency devices. A surprising result of this material is that it does not

require an HRT; the most logical explanation for this is that it passivates the charged defects at the TCO interface more effectively. It also has practical advantages over oxygenated CdS. It does not contain sulfates which are typically very sensitive to water and can decompose under the electron beam of a transmission electron microscope, it can be tuned by varying the MgO/ZnO ratio in the sputter target which is simpler and more repeatable than maintaining a small flow of reactive oxygen, particularly in a large industrial application, and it seems to have superior adhesion to the substrate. In all, this material appears to be the most promising advanced front contact for use in the future.

5.3. FUTURE DIRECTIONS

The roadmap of the thin-film photovoltaics program at CSU involves a series of steps shown in Figure 5.2. The first step, moving from the baseline device on the left to the middle diagram, involves this front contact effort and work on the back contact of the solar cell. As this work has accomplished the objective of a transparent front contact, future work could focus on further improvements to boost the transmission of the superstrate and front contact even higher: high-mobility TCO's, advanced antireflection coatings on both surfaces of the glass, and advanced glasses which could be ultra-thin, flexible, and tolerate higher temperature processing.

Further ahead, more complete current collection will enable the second advance of the roadmap, which is moving to multiple thin-film polycrystalline junctions in tandem. Tandem solar cells allow different materials to absorb different parts of the solar spectrum, collecting more energy from high-energy photons in the process. The top, high bandgap cell collects the most energy in this arrangement; therefore maximal transmission of high-energy photons as demonstrated in this project enables the possibility of benefitting from such a structure. The multi-junction will also require a

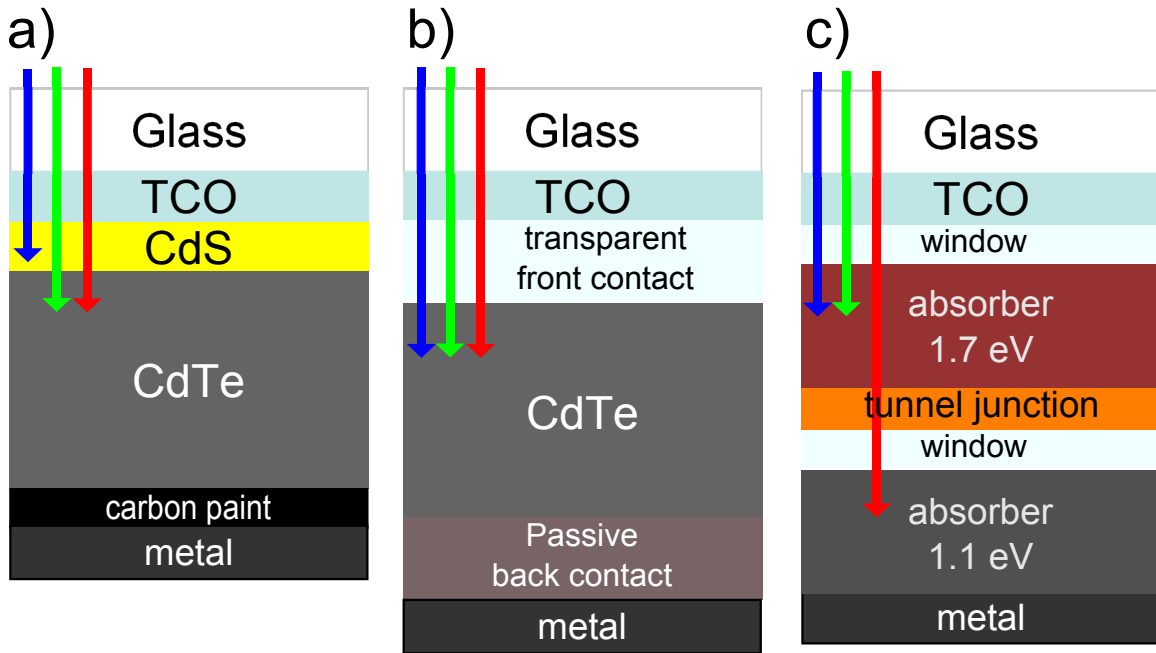


FIGURE 5.2. A future roadmap which involves going from a) the baseline device to b) a device with improved contact properties to c) a tandem multi-junction, thin-film cell for much higher efficiency.

full understanding of both front and back contacts of the cell, and it has been demonstrated here that contact materials can be tuned to match the absorber properties.

BIBLIOGRAPHY

- [1] T. Stocker, D. Qin, G.-K. Plattner, M. Tignor, S. K. Allen, J. Boschung, A. Nauels, Y. Xia, V. Bex, and P. M. Midgley, Eds., *Climate Change 2013: The Physical Science Basis. Contribution of Working Group I of the Fifth Assessment Report of the Intergovernmental Panel on Climate Change*. Cambridge, U.K. and New York: Cambridge University Press, 2013.
- [2] C. Field, V. Barros, D. Dokken, K. Mach, M. Mastrandrea, T. Bilir, M. Chatterjee, K. Ebi, Y. Estrada, R. Genova, B. Girma, E. Kissel, A. Levy, S. MacCracken, P. Mastrandrea, and L. White, Eds., *Climate Change 2014: Impacts, Adaptation, and Vulnerability, Part A: Global and Sectoral Aspects. Contribution of Working Group II to the Fifth Assessment Report of the Intergovernmental Panel on Climate Change*. Cambridge, U.K. and New York: Cambridge University Press, 2014, vol. 1.
- [3] O. Edenhofer, R. Pichs-Madruga, Y. Sokona, J. Minx, E. Farahani, S. Kadner, K. Seyboth, A. Adler, I. Baum, S. Brunner, P. Eikemeier, B. Kriemann, J. Savolainen, S. Schloemer, C. von Stechow, and T. Zwickel, Eds., *Climate Change 2014: Mitigation of Climate Change. Contribution of Working Group III to the Fifth Assessment Report of the Intergovernmental Panel on Climate Change*. Cambridge, U.K. and New York: Cambridge University Press Cambridge, 2014.
- [4] O. Morton, "Solar energy: A new day dawning?: Silicon valley sunrise," *Nature*, vol. 443, no. 7107, pp. 19–22, Sep. 2006.
- [5] J. Meldrum, S. Nettles-Anderson, G. Heath, and J. Macknick, "Life cycle water use for electricity generation: a review and harmonization of literature estimates," *Environmental Research Letters*, vol. 8, no. 1, p. 015031, Mar. 2013.

- [6] P. Denholm and R. M. Margolis, "Land-use requirements and the per-capita solar footprint for photovoltaic generation in the united states," *Energy Policy*, vol. 36, no. 9, pp. 3531–3543, Sep. 2008.
- [7] E. Drury, A. Lopez, P. Denholm, and R. Margolis, "Relative performance of tracking versus fixed tilt photovoltaic systems in the USA," *Progress in Photovoltaics: Research and Applications*, vol. 22, no. 12, pp. 1302–1315, Dec. 2014.
- [8] P. Denholm and R. M. Margolis, "Evaluating the limits of solar photovoltaics (PV) in traditional electric power systems," *Energy Policy*, vol. 35, no. 5, pp. 2852–2861, May 2007.
- [9] "Global market outlook for photovoltaics 2014-2018," European Photovoltaic Industry Association, Tech. Rep., 2014.
- [10] M. Bazilian, I. Onyeji, M. Liebreich, I. MacGill, J. Chase, J. Shah, D. Gielen, D. Arent, D. Landfear, and S. Zhengrong, "Re-considering the economics of photovoltaic power," *Renewable Energy*, vol. 53, pp. 329–338, May 2013.
- [11] "First Solar Annual Report," 2013. [Online]. Available: <http://investor.firstsolar.com/annuals.cfm>
- [12] S. Ringbeck and J. Sutterlueti, "BoS costs: status and optimization to reach industrial grid parity," *Progress in Photovoltaics: Research and Applications*, vol. 21, no. 6, pp. 1411–1428, 2013.
- [13] A. Goodrich, T. James, and M. Woodhouse, "Residential, commercial, and utility-scale photovoltaic (PV) system prices in the United States: Current drivers and cost reduction opportunities," National Renewable Energy Laboratory, Tech. Rep. NREL/TP-6A20-53347, Feb. 2012.
- [14] S. Chu and A. Majumdar, "Opportunities and challenges for a sustainable energy future," *Nature*, vol. 488, no. 7411, pp. 294–303, Aug. 2012.

- [15] S. Sze, *Physics of Semiconductor Devices*, 2nd ed. New York: John Wiley & Sons, 1981.
- [16] W. Shockley and H. J. Queisser, “Detailed Balance Limit of Efficiency of pn Junction Solar Cells,” *Journal of Applied Physics*, vol. 32, p. 510, 1961.
- [17] J. J. Loferski, “Theoretical considerations governing the choice of the optimum semiconductor for photovoltaic solar energy conversion,” *Journal of Applied Physics*, vol. 27, p. 777, 1956.
- [18] A. Martí and G. L. Araújo, “Limiting efficiencies for photovoltaic energy conversion in multi-gap systems,” *Solar Energy Materials and Solar Cells*, vol. 43, no. 2, pp. 203–222, Sep. 1996.
- [19] J. Sites and J. Pan, “Strategies to increase CdTe solar-cell voltage,” *Thin Solid Films*, vol. 515, no. 15, pp. 6099–6102, 2007.
- [20] S. Kurtin, T. C. McGill, and C. A. Mead, “Fundamental transition in the electronic nature of solids,” *Physical Review Letters*, vol. 22, no. 26, pp. 1433–1436, Jun. 1969.
- [21] R. Klenk, “Characterisation and modelling of chalcopyrite solar cells,” *Thin Solid Films*, vol. 387, no. 12, pp. 135–140, May 2001.
- [22] “Properties of soda-lime silica float glass,” Pilkington North America, Inc., Toledo, Ohio, Tech. Rep. ATS-129, 2013.
- [23] Y. Yan, X. Li, R. Dhere, M. Al-Jassim, K. Jones, M. Young, and M. Scott, “SiO₂ as barrier layer for Na out-diffusion from soda-lime glass,” in *2010 35th IEEE Photovoltaic Specialists Conference (PVSC)*, Jun. 2010, pp. 002 519–002 521.
- [24] M. Rubin, “Optical properties of soda lime silica glasses,” *Solar Energy Materials*, vol. 12, no. 4, pp. 275–288, Sep. 1985.
- [25] D. W. Niles, D. Rioux, and H. Höchst, “A photoemission investigation of the SnO₂/CdS interface: A front contact interface study of CdS/CdTe solar cells,” *Journal of Applied Physics*, vol. 73, no. 9, pp. 4586–4590, May 1993.

- [26] D. Albin, Y. Yan, and M. Al-Jassim, "The effect of oxygen on interface microstructure evolution in CdS/CdTe solar cells," *Progress in Photovoltaics: Research and Applications*, vol. 10, no. 5, pp. 309–322, 2002.
- [27] D. H. Rose, F. S. Hasoon, R. G. Dhere, D. S. Albin, R. M. Ribelin, X. S. Li, Y. Mahathongdy, T. A. Gessert, and P. Sheldon, "Fabrication procedures and process sensitivities for CdS/CdTe solar cells," *Progress in Photovoltaics Research and Applications*, vol. 7, no. 5, pp. 331–340, 1999.
- [28] M. Terheggen, H. Heinrich, G. Kostorz, A. Romeo, D. Bätzner, A. N. Tiwari, A. Bosio, and N. Romeo, "Structural and chemical interface characterization of CdTe solar cells by transmission electron microscopy," *Thin Solid Films*, vol. 431, pp. 262–266, 2003.
- [29] B. Korevaar, R. Shuba, A. Yakimov, H. Cao, J. Rojo, and T. Tolliver, "Initial and degraded performance of thin film CdTe solar cell devices as a function of copper at the back contact," *Thin Solid Films*, vol. 519, no. 21, pp. 7160–7163, Aug. 2011.
- [30] J. M. Kephart, R. M. Geisthardt, and W. S. Sampath, "Optimization of CdTe thin-film solar cell efficiency using a sputtered, oxygenated CdS window layer," *Progress in Photovoltaics: Research and Applications*, 2015.
- [31] P. Kobayakov, N. Schuh, K. Walters, V. Manivannan, and W. Sampath, "Continuous in-line processing of CdS/CdTe devices: Process control using XRF and efficient heating," in *2010 35th IEEE Photovoltaic Specialists Conference (PVSC)*, Jun. 2010, pp. 780–785.
- [32] D. M. Mattox, *Handbook of physical vapor deposition (PVD) processing*. Westwood, New Jersey USA: Noyes Publications, 1998.
- [33] "First solar achieves efficiency, durability milestones," Feb. 2015. [Online]. Available: <http://investor.firstsolar.com/releasedetail.cfm?ReleaseID=895118>

- [34] M. Topič, R. Geisthardt, and J. Sites, “Performance limits and status of single-junction solar cells with emphasis on CIGS,” *IEEE Journal of Photovoltaics*, vol. 5, no. 1, pp. 360–365, Jan. 2015.
- [35] J. Fritsche, A. Klein, and W. Jägermann, “Thin film solar cells: Materials science at interfaces,” *Advanced Engineering Materials*, vol. 7, no. 10, pp. 914–920, 2005.
- [36] X. Wu, J. C. Keane, R. G. Dhere, C. DeHart, D. S. Albin, A. Duda, T. A. Gessert, S. Asher, D. H. Levi, and P. Sheldon, “16.5%-efficient CdS/CdTe polycrystalline thin-film solar cell,” in *Proceedings of the 17th European Photovoltaic Solar Energy Conference*, 2001, pp. 995–1000.
- [37] A. D. Compaan, A. Gupta, J. Drayton, S.-H. Lee, and S. Wang, “14% sputtered thin-film solar cells based on CdTe,” *physica status solidi (b)*, vol. 241, no. 3, pp. 779–782, 2004.
- [38] J. D. Major, Y. Y. Proskuryakov, and K. Durose, “Impact of CdTe surface composition on doping and device performance in close Space sublimation deposited CdTe solar cells,” *Progress in Photovoltaics: Research and Applications*, vol. 21, no. 4, pp. 436–443, 2011.
- [39] B. E. McCandless and K. D. Dobson, “Processing options for CdTe thin film solar cells,” *Solar Energy*, vol. 77, no. 6, pp. 839–856, 2004.
- [40] T. Takamoto, T. Agui, H. Kurita, and M. Ohmori, “Improved junction formation procedure for low temperature deposited CdS/CdTe solar cells,” *Solar Energy Materials and Solar Cells*, vol. 49, no. 14, pp. 219–225, Dec. 1997.
- [41] X. Li, R. Ribelin, Y. Mahathongdy, D. Albin, R. Dhere, D. Rose, S. Asher, H. Moutinho, and P. Sheldon, “The effect of high-resistance SnO₂ on CdS/CdTe device performance,” in *AIP Conference Proceedings*, 1998, pp. 230–235.
- [42] C. S. Ferekides, R. Mamazza, U. Balasubramanian, and D. L. Morel, “Transparent conductors and buffer layers for CdTe solar cells,” *Thin Solid Films*, vol. 480, pp. 224–229, 2005.

- [43] X. Wu, S. Asher, D. H. Levi, D. E. King, Y. Yan, T. A. Gessert, and P. Sheldon, “Interdiffusion of CdS and Zn₂SnO₄ layers and its application in CdS/CdTe polycrystalline thin-film solar cells,” *Journal of Applied Physics*, vol. 89, no. 8, pp. 4564–4569, 2001.
- [44] M. Tashkandi and W. Sampath, “Eliminating pinholes in CSS deposited CdS films,” in *2012 38th IEEE Photovoltaic Specialists Conference (PVSC)*, Jun. 2012, pp. 000 143 –000 146.
- [45] J. M. Kephart, R. M. Geishardt, Z. Ma, J. McCamy, and W. S. Sampath, “Reduction of window layer optical losses in CdS/CdTe solar cells using a float-line manufacturable HRT layer,” in *2013 39th IEEE Photovoltaic Specialists Conference (PVSC)*, 2013, pp. 1653–1657.
- [46] B. Korevaar, A. Halverson, J. Cao, J. Choi, C. Collazo-Davila, and W. Huber, “High efficiency CdTe cells using manufacturable window layers and CdTe thickness,” *Thin Solid Films*, vol. 535, pp. 229–232, May 2013.
- [47] M. Gloeckler, A. L. Fahrenbruch, and J. R. Sites, “Numerical modeling of CIGS and CdTe solar cells: setting the baseline,” in *Photovoltaic Energy Conversion, 2003. Proceedings of 3rd World Conference on*, vol. 1. IEEE, 2003, pp. 491–494.
- [48] D. Mao, L. H. Feng, Y. Zhu, J. Tang, W. Song, R. Collins, D. L. Williamson, and J. U. Trefny, “Interdiffusion in polycrystalline thinfilm CdTe/CdS solar cells,” in *AIP Conference Proceedings*, vol. 353. AIP Publishing, Jan. 1996, pp. 352–359.
- [49] A. Kanevce and T. Gessert, “Optimizing CdTe solar cell performance: Impact of variations in minority-carrier lifetime and carrier density profile,” *Photovoltaics, IEEE Journal of*, vol. 1, no. 1, pp. 99–103, Jul. 2011.
- [50] A. Kanevce, D. Kuciauskas, T. A. Gessert, D. H. Levi, and D. S. Albin, “Impact of interface recombination on time resolved photoluminescence decays (TRPL) in CdTe solar cells (numerical simulation analysis),” in *2012 38th IEEE Photovoltaic Specialists Conference (PVSC)*, vol. 3, 2012, p. 8.

- [51] M. Helander, M. Greiner, Z. Wang, and Z. Lu, “Pitfalls in measuring work function using photoelectron spectroscopy,” *Applied Surface Science*, vol. 256, no. 8, pp. 2602–2605, Feb. 2010.
- [52] M. Burgelman, P. Nollet, and S. Degreve, “Modelling polycrystalline semiconductor solar cells,” *Thin Solid Films*, vol. 361362, pp. 527–532, Feb. 2000.
- [53] G. V. Rao, F. Säuberlich, and A. Klein, “Influence of Mg content on the band alignment at CdS/(Zn,Mg)O interfaces,” *Applied Physics Letters*, vol. 87, no. 3, pp. 032 101–032 101–3, Jul. 2005.
- [54] D. Hariskos, B. Fuchs, R. Menner, N. Naghavi, C. Hubert, D. Lincot, and M. Powalla, “The Zn(S,O,OH)/ZnMgO buffer in thin-film Cu(In,Ga)(Se,S)₂-based solar cells part II: Magnetron sputtering of the ZnMgO buffer layer for in-line co-evaporated Cu(In,Ga)Se₂ solar cells,” *Progress in Photovoltaics: Research and Applications*, vol. 17, no. 7, pp. 479–488, Nov. 2009.
- [55] T. Minemoto, T. Negami, S. Nishiwaki, H. Takakura, and Y. Hamakawa, “Preparation of Zn_{1-x}Mg_xO films by radio frequency magnetron sputtering,” *Thin Solid Films*, vol. 372, no. 12, pp. 173–176, Sep. 2000.
- [56] F. Erfurth, A. Grimm, J. Palm, T. P. Niesen, F. Reinert, L. Weinhardt, and E. Umbach, “Direct determination of the band alignment at the (Zn,Mg)O/CISSe interface,” *Applied Physics Letters*, vol. 98, no. 14, pp. 142 107–1–142 107–3, Apr. 2011.
- [57] A. Suryanarayana Reddy, P. Prathap, Y. P. V. Subbaiah, K. T. Ramakrishna Reddy, and J. Yi, “Growth and physical behaviour of Zn_{1-x}Mg_xO films,” *Thin Solid Films*, vol. 516, no. 20, pp. 7084–7087, Aug. 2008.

- [58] M. Gloeckler, C. R. Jenkins, and J. R. Sites, "Explanation of Light/Dark Superposition Failure in CIGS Solar Cells," in *Symposium B Compound Semiconductor Photovoltaics*, ser. MRS Online Proceedings Library, vol. 763, 2003.
- [59] J. Fritsche, S. Gunst, A. Thißen, R. Gegenwart, A. Klein, and W. Jägermann, "CdTe thin film solar cells: The CdS/SnO₂ front contact," in *Materials Research Society Symposium Proceedings*, vol. 668. Cambridge Univ Press, 2001, p. 5.
- [60] V. Krishnakumar, K. Ramamurthi, A. Klein, and W. Jägermann, "Band alignment of differently treated TCO/CdS interface," *Thin Solid Films*, vol. 517, no. 7, pp. 2558–2561, Feb. 2009.
- [61] A. Klein, C. Körber, A. Wachau, F. Säuberlich, Y. Gassenbauer, S. P. Harvey, D. E. Proffit, and T. O. Mason, "Transparent conducting oxides for photovoltaics: Manipulation of Fermi level, work function and energy band alignment," *Materials*, vol. 3, no. 11, pp. 4892–4914, Nov. 2010.
- [62] D. E. Swanson, R. M. Geisthardt, J. T. McGoffin, J. D. Williams, and J. R. Sites, "Improved CdTe solar-cell performance by plasma cleaning the TCO layer," *IEEE Journal of Photovoltaics*, vol. 3, no. 2, pp. 838–842, 2013.
- [63] M. G. Helander, M. T. Greiner, Z. B. Wang, W. M. Tang, and Z. H. Lu, "Work function of fluorine doped tin oxide," *Journal of Vacuum Science & Technology A: Vacuum, Surfaces, and Films*, vol. 29, no. 1, p. 011019, 2011.
- [64] J. R. Sites, "Quantification of losses in thin-film polycrystalline solar cells," *Solar Energy Materials & Solar Cells*, vol. 75, no. 1-2, pp. 243–251, 2003.
- [65] X. Li, R. Ribelin, Y. Mahathongdy, D. Albin, R. Dhere, D. Rose, S. Asher, H. Moutinho, and P. Sheldon, "The effect of high-resistance SnO₂ on CdS/CdTe device performance," *AIP Conference Proceedings*, vol. 462, no. 1, pp. 230–235, Mar. 1999.

- [66] E. Klampaftis, D. Ross, K. R. McIntosh, and B. S. Richards, “Enhancing the performance of solar cells via luminescent down-shifting of the incident spectrum: A review,” *Solar Energy Materials and Solar Cells*, vol. 93, no. 8, pp. 1182–1194, Aug. 2009.
- [67] S. D. Hodgson, W. S. M. Brooks, A. J. Clayton, G. Kartopu, V. Barrioz, and S. J. C. Irvine, “Enhancing blue photoresponse in CdTe photovoltaics by luminescent down-shifting using semiconductor quantum dot/PMMA films,” *Nano Energy*, vol. 2, no. 1, pp. 21–27, Jan. 2013.
- [68] J. Zhou, X. Wu, G. Teeter, B. To, Y. Yan, R. G. Dhere, and T. A. Gessert, “CBD $\text{Cd}_{1-x}\text{Zn}_x\text{S}$ thin films and their application in CdTe solar cells,” *physica status solidi (b)*, vol. 241, no. 3, pp. 775–778, 2004.
- [69] G. Kartopu, A. J. Clayton, W. S. M. Brooks, S. D. Hodgson, V. Barrioz, A. Maertens, D. A. Lamb, and S. J. C. Irvine, “Effect of window layer composition in $\text{Cd}_{1-x}\text{Zn}_x\text{S}/\text{CdTe}$ solar cells,” *Progress in Photovoltaics: Research and Applications*, 2012.
- [70] X. Wu, Y. Yan, R. G. Dhere, Y. Zhang, J. Zhou, C. Perkins, and B. To, “Nanostructured CdS:O film: preparation, properties, and application,” *physica status solidi (c)*, vol. 1, no. 4, pp. 1062–1066, 2004.
- [71] X. Wu, R. G. Dhere, Y. Yan, I. J. Romero, Y. Zhang, J. Zhou, C. DeHart, A. Duda, C. Perkins, and B. To, “High-efficiency polycrystalline CdTe thin-film solar cells with an oxygenated amorphous CdS (a-CdS:O) window layer,” in *Photovoltaic Specialists Conference, 2002. Conference Record of the Twenty-Ninth IEEE*. IEEE, 2003, pp. 531–534.
- [72] A. Gupta, K. Allada, S. H. Lee, and A. D. Compaan, “Oxygenated CdS window layer for sputtered CdS/CdTe solar cells,” in *Materials Research Society Symposium Proceedings*, vol. 763. Warrendale, Pa.; Materials Research Society; 1999, 2003, pp. 341–346.

- [73] Y. L. Soo, W. H. Sun, S. C. Weng, Y. S. Lin, S. L. Chang, L. Y. Jang, X. Wu, and Y. Yan, “Local environment surrounding S and Cd in CdS:O thin film photovoltaic materials probed by x-ray absorption fine structures,” *Applied Physics Letters*, vol. 89, p. 131908, 2006.
- [74] J. M. Kephart, R. Geisthardt, and W. S. Sampath, “Sputtered, oxygenated CdS window layers for higher current in CdS/CdTe thin film solar cells,” in *2012 38th IEEE Photovoltaic Specialists Conference (PVSC)*, Jun. 2012, pp. 854–858.
- [75] R. Asaba, K. Wakita, A. Kitano, Y. Shim, N. Mamedov, A. Bayramov, E. Huseynov, and I. Hasanov, “Structure and optical properties of CdS:O thin films,” *physica status solidi (c)*, vol. 10, no. 7-8, pp. 1098–1101, Aug. 2013.
- [76] D. Albin, R. Dhere, S. Glynn, and W. Metzger, “The direct correlation of CdTe solar cell stability with mobile ion charge generation during accelerated lifetime testing,” in *2009 34th IEEE Photovoltaic Specialists Conference (PVSC)*, Jun. 2009, pp. 001 903–001 908.
- [77] C. R. Corwine, A. O. Pudov, M. Gloeckler, S. H. Demtsu, and J. R. Sites, “Copper inclusion and migration from the back contact in CdTe solar cells,” *Solar Energy Materials and Solar Cells*, vol. 82, no. 4, pp. 481–489, 2004.
- [78] K. D. Dobson, I. Visoly-Fisher, G. Hodes, and D. Cahen, “Stabilizing CdTe/CdS solar cells with Cu-containing contacts to p-CdTe,” *Advanced Materials*, vol. 13, no. 19, pp. 1495–1499, Oct. 2001.
- [79] R. C. Powell, “Research leading to high-throughput manufacturing of thin-film CdTe PV modules,” National Renewable Energy Laboratory, NREL Subcontract Report SR-520-39669, First Solar SR-520-39669, 2006.

- [80] D. Hanks, J. Kephart, K. Horsley, M. Blum, M. Mezher, L. Weinhardt, Häming, R. Wilks, T. Hofmann, W. Yang, M. Bär, W. Sampath, and C. Heske, “Characterization of sulfur bonding in CdS:O buffer layers for CdTe-based thin-film solar cells,” *submitted to Advanced Energy Materials*, 2015.
- [81] R. S. Yadav, P. Mishra, R. Mishra, M. Kumar, and A. C. Pandey, “Growth mechanism and optical property of CdS nanoparticles synthesized using amino-acid histidine as chelating agent under sonochemical process,” *Ultrasonics sonochemistry*, vol. 17, no. 1, pp. 116–122, 2010.
- [82] M. P. Taylor, D. W. Readey, M. F. A. M. van Hest, C. W. Teplin, J. L. Alleman, M. S. Dabney, L. M. Gedvilas, B. M. Keyes, B. To, J. D. Perkins, and D. S. Ginley, “The remarkable thermal stability of amorphous In-Zn-O transparent conductors,” *Advanced Functional Materials*, vol. 18, no. 20, pp. 3169–3178, 2008.
- [83] H. Wilhelm, H.-W. Schock, and R. Scheer, “Interface recombination in heterojunction solar cells: Influence of buffer layer thickness,” *Journal of Applied Physics*, vol. 109, no. 8, p. 084514, Apr. 2011.
- [84] R. Paternoster, R. Brame, P. Mazerolle, and A. Piquero, “Using the correct statistical test for the equality of regression coefficients,” *Criminology*, vol. 36, no. 4, pp. 859–866, Nov. 1998.
- [85] T. Minemoto, T. Matsui, H. Takakura, Y. Hamakawa, T. Negami, Y. Hashimoto, T. Uenoyama, and M. Kitagawa, “Theoretical analysis of the effect of conduction band offset of window/CIS layers on performance of CIS solar cells using device simulation,” *Solar Energy Materials and Solar Cells*, vol. 67, no. 1–4, pp. 83–88, Mar. 2001.
- [86] T. Minemoto, Y. Hashimoto, T. Satoh, T. Negami, H. Takakura, and Y. Hamakawa, “Cu(In,Ga)Se₂ solar cells with controlled conduction band offset of window/Cu(In,Ga)Se₂ layers,” *Journal of Applied Physics*, vol. 89, no. 12, pp. 8327–8330, Jun. 2001.

- [87] J. Fritsche, T. Schulmeyer, D. Kraft, A. Thißen, A. Klein, and W. Jägermann, “Utilization of sputter depth profiling for the determination of band alignment at polycrystalline CdTe/CdS heterointerfaces,” *Applied Physics Letters*, vol. 81, p. 2297, 2002.
- [88] K. Nishi, H. Ohyama, T. Suzuki, T. Mitsuyu, and T. Tomimasu, “Evaluation of the CdS/CdTe interface using free-electron laser internal photoemission technique,” *Applied Physics Letters*, vol. 70, no. 26, pp. 3585–3587, Jun. 1997.
- [89] M. Kibel, “X-Ray Photoelectron Spectroscopy,” in *Surface Analysis Methods in Materials Science*, 2nd ed., D. O’Connor, B. Sexton, and R. S. C. Smart, Eds. Berlin, Heidelberg, and New York: Springer-Verlag, 2003, pp. 175–202.
- [90] C. Klauber and R. S. C. Smart, “Solid Surfaces, Their Structure and Composition,” in *Surface Analysis Methods in Materials Science*, 2nd ed., D. O’Connor, B. Sexton, and R. S. C. Smart, Eds. Berlin, Heidelberg, and New York: Springer-Verlag, 2003, pp. 3–70.
- [91] R. Leckey, “Ultraviolet Photoelectron Spectroscopy of Solids,” in *Surface Analysis Methods in Materials Science*, 2nd ed., D. O’Connor, B. Sexton, and R. S. C. Smart, Eds. Berlin, Heidelberg, and New York: Springer-Verlag, 2003, pp. 337–345.
- [92] J. Marra and J. A. M. Huethorst, “Physical principles of Marangoni drying,” *Langmuir*, vol. 7, no. 11, pp. 2748–2755, Nov. 1991.
- [93] A. F. M. Leenaars, J. A. M. Huethorst, and J. J. Van Oekel, “Marangoni drying: A new extremely clean drying process,” *Langmuir*, vol. 6, no. 11, pp. 1701–1703, Nov. 1990.

APPENDIX A

PHOTOELECTRON SPECTROSCOPY MEASUREMENTS

A.1. PRINCIPLE OF OPERATION

The photoelectric effect is the excitation of an electron in a material by a photon with sufficient energy to allow it to escape the material. The photon must have an energy greater than the work function of the material, which is typically a few electron volts (refer to Figure 1.3). Electrons in materials can occupy atomic states all the way from the lowest core electrons to the valence and conduction bands. When these electrons are excited by a photon with sufficient energy, they can be ejected from the material. Most of these electrons will be scattered by the material itself; some will escape elastically and their kinetic energy will be given by Equation 6, where $h\nu$ is the energy of the photon, E_B is the binding energy of the state which is being measured, and ϕ is a work function value which depends on the sample and spectrometer [89].

$$(6) \quad KE = h\nu - E_B - \phi$$

If the kinetic energy of these materials can be accurately measured, then with the proper calibration the binding energy of the state from which the electron came can be determined. This allows for a great deal of chemical and electronic information to be discerned. Electrons in the core states have energies characteristic of the atoms they came from; these energy levels are mostly independent of chemical bonding but not completely. As an example, two peaks that are close together could be identified as the 2p orbital of a specific metal, with one the metallic state and one from a surface oxide.

The electrons in lower core orbitals are bound tightly and require hundreds to thousands of eV to escape the material. Therefore, soft X-rays on the order of 1 keV are useful for probing these states. In typical laboratory systems, x-ray tubes using Al $K\alpha$ or Mg $K\alpha$ radiation are used. These have photon energies of 1486.6 eV and 1256.3 eV, respectively. The distance these x-rays can travel into a material depends on a number of factors including the angle of incoming light, the material, and the photon energy itself. An attenuation length of 50-100 eV is typical. The actual signal also depends on electrons being able to escape without losing energy via scattering; this distance, called the electron inelastic mean free path (IMFP), is closer to 2 nm and therefore makes photoelectron spectroscopy highly surface sensitive [90].

For valence states, a lower energy photon may be used. Helium produces $I\alpha$ and $II\alpha$ radiation which have photon energies of 21.21 eV and 40.81 eV. Lower energy electrons excited by these photons have even smaller IMFP's, about 0.5 nm. This makes ultraviolet photoelectron spectroscopy, or UPS, extremely sensitive to surface contamination, with even monolayers having a strong impact on experimental results [91].

A.2. SAMPLE PREPARATION

In order to prepare the cleanest possible samples, it is critical to begin with the cleanest possible substrates. A process was developed which first cleans the samples in isopropyl alcohol to partially remove organic residue, followed by ultrasonic cleaning in a solution of Micro-90, an alkaline surfactant. This is followed by a thorough rinse and ultrasonic cleaning in deionized water. To minimize residue from drying, a Marangoni drying process was implemented. In this process, ultrahigh purity nitrogen gas saturated with isopropyl alcohol flows over the surface of the water, while the water is slowly allowed to drain from the sonicator. The dissolution of isopropyl alcohol into the water creates a surface tension gradient which physically pulls the water away from the

substrate surface and dramatically reduces the thickness of water that is left to dry and contaminate the surface [92, 93].

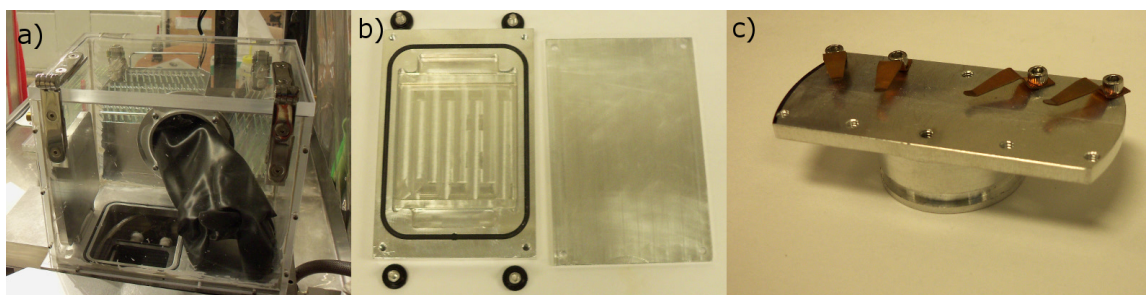


FIGURE A.1. Several tools are needed to prevent air exposure of samples for photoelectron spectroscopy measurements. a) A glove box was constructed which attaches to the ARDS load lock and allows samples to be extracted under nitrogen flow. b) An aluminum container with o-ring seal can be used to transfer the sample to the main glove box. c) The sample can be extracted and cut to size in the main glove box, where it is attached to the custom-made XPS sample holder.

Clean substrates were placed onto the end effector of the ARDS which was itself thoroughly cleaned. The glass was heated in the substrate heater of the ARDS under vacuum and allowed to cool in vacuum. Figure A.1 shows equipment used to minimize contamination of the sample. A small glove box was designed and constructed which fits on the extension of the ARDS load lock. The end effector can extend into this extension. The glove box is purged with ultrahigh purity nitrogen and sealed, and the load lock is clamped shut and vented with nitrogen, as the nitrogen vents into the glove box, a door can be opened and the sample can be extracted. The sample is then placed in a small machined aluminum container with a dovetail o-ring seal which was designed to hold a standard-size sample with minimum space.

This box is sealed with lid which is screwed tight and immediately transferred to the main glove box in the lab which is maintained below 1 ppm of oxygen and water. In this main glove box, the sample is cut to an appropriate size for mounting to the XPS sample holder (approximately 10 x 15 mm). This holder was constructed from aluminum with copper clips that screw tight so as to avoid the typical adhesive tape used for XPS samples at CSU. This sample is kept in the main glove

box until it must be transferred to the main campus for XPS measurement. Immediately prior to transport the sample is put in a sealed plastic container.

At the XPS system, the load lock is vented, the plastic container is opened, and the sample is transferred. The sample is exposed to air for approximately 10 seconds.

A.3. PHOTOELECTRON SPECTROSCOPY MEASUREMENTS

The kinetic energy is measured in the photoemission system at CSU via a hemispheric analyzer. This type of analyzer has two concentric metal hemispheres. The emitted electrons enter the detector tangentially and are deflected by a bias difference between the hemispheres. Typically, to keep the energy resolution of the measured electrons relatively constant, the electrons are retarded to a pass energy prior to entry. On the other side of the detector, the position at which the electrons arrive can be measured, allowing the kinetic energy to be inferred.

Of course, inferring the binding energy implies that the initial excitation energy is known accurately. X-rays emitted from a tube have a natural broadening; this can be reduced by a monochromator which diffracts photons of a very specific energy. For the x-ray analyses in this work Al $K\alpha$ radiation was used exclusively, which has a linewidth of 0.85 eV, but was monochromated to reduce this value. The ultraviolet radiation has the advantage of having a linewidth of only a few meV, which is crucial for measurements of work function, electron affinity, etc. in which 1 eV is a very large difference.

A.4. ULTRAVIOLET SOURCE INSTALLATION

The existing system used for photoelectron spectroscopy measurements had an x-ray source but no source of UV light. UV sources were compared and the PREVAC UVS40A2 was selected for installation onto the PHI 5800 system. A UV source consists of a chamber in which a helium

plasma is excited to emit the $I\alpha$ and $II\alpha$ radiation. Because all known materials are highly absorbing at this photon energy, a windowless arrangement must be used in which there is a direct line of sight from the plasma to the measurement sample. Because the sample must remain in ultra-high vacuum, a dual-stage pumping system with a long capillary limits the leak rate from the UV source to the main chamber. The first stage directly pumps on the plasma chamber. Here, an oil-based rotary vane mechanical pump was used with a zeolite trap to prevent backstreaming of oil into the system. In this plasma chamber there is an aperture at the front leading to a second volume. This volume is pumped with a turbomolecular pump. A small aperture at the end of a long tube in this system allows the light to be transmitted to the sample while minimizing leak rate to the main chamber. Typically, the system base pressure is near $1 \cdot 10^{-9}$ Torr, and rises to approximately $5 \cdot 10^{-8}$ Torr while helium is flowing. This is comparable to the effect of using the argon ion gun for sputter cleaning and depth profiling of the sample, and is low enough for measurement.

In order to accommodate all the requirements of the ultraviolet source, a pumping system, cooling water system, helium supply system, and power supply were installed along with the source in the XPS facility. These systems can be seen in Figure A.2. The pumping system is a rack which contains the mechanical first-stage pump as well as the backing pump for the turbomolecular pump, the turbomolecular pump (visible in figure) and controller. A UHV tube connects the second stage to the UV source along with a ultra-high vacuum isolation valve. A UHV valve also attaches the first-stage line and can isolate it when not in use to prevent contamination of the XPS environment. A z-axis bellows allows the capillary to be placed 25-50 mm from the sample during operation; when not in use, it can be retracted away to prevent damage. To operate the system, the first and second stages are opened to the pumping systems, and the leak valve (visible at top of UV source) is turned until the desired pressure is reached. A leak rate which creates a pressure of 13-14 mTorr measured at the mechanical pump is the minimum pressure needed to ignite a

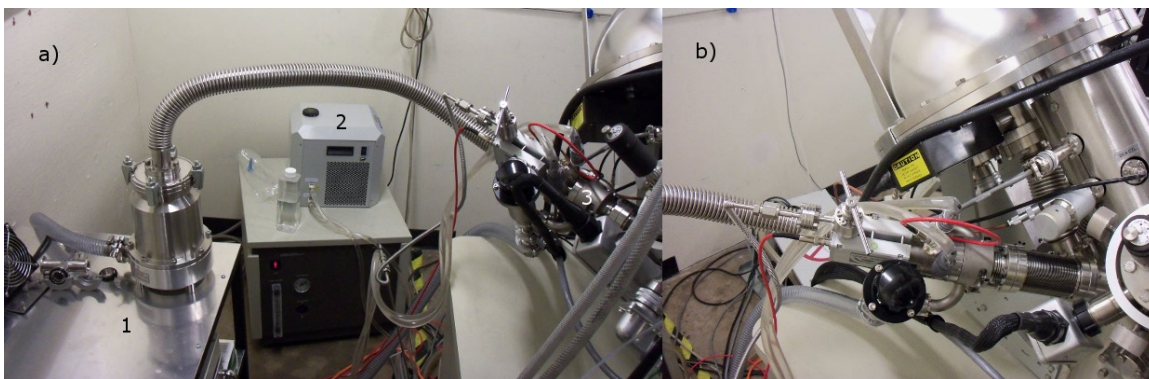


FIGURE A.2. a) The UV source system consists of 1: a pumping system with first-stage, foreline, and turbomolecular pumps; 2: A chiller with cooling lines, 3: a UV source with helium line and leak valve. b) An image of the UV source shows the leak valve on top with isolation valves and z-axis bellows.

plasma and this value was used for this work. The power supply was kept at 80 mA current which corresponded to a voltage of 0.52 kV.

Unlike with the x-ray source, the beam has a visible component and this could be used to help align the beam to measure roughly the same spot as the x-ray measurements. The beam size is approximately 2 mm so the beam was kept near the center of samples to prevent signals from adjacent materials.

A.5. DATA ANALYSIS

XPS spectra were typically analyzed for chemical composition in the PHI Multipak program. Initially a survey scan is performed to look for any unexpected elements beyond those in the material and adventitious carbon. Then, high-resolution scans of the peaks are performed and with Shirley background subtraction used to accurately calculate the area below each peak. The program uses known sensitivity factors to produce relative atomic concentrations of the elements.

In some cases, peaks were fit manually in the IGOR program. To normalize the SO_x^{2-} and S^{2-} peaks in Figure 4.1, the total area under both peaks was normalized to create an accurate comparison. Then the relative peak heights could be used to determine the relative composition.

To analyze UPS spectra, a program was written in the R programming language to import data and fit important values. Its output is shown in Figure A.3. This program converts the energy scale to kinetic energy from the binding energy scale produced by the program (which assumes a photon energy of 1486.6 eV). The peak at the low-KE portion of the spectrum, part b), is the secondary electron cutoff. The energy value of the cutoff is found by fitting three lines to the data and finding the middle of the segment of the center line between the two intersections. If the system energy calibration were exactly correct, this would give the workfunction of the material; however, precise calibration is not needed for this analysis since the Fermi level will provide a binding energy reference. Plot c) shows the valence band maximum region. The VBM energy location can be found by fitting lines to the two straight regions of the plot; for a material known to be n-type this should be below the Fermi level by approximately the bandgap energy. Finally, the Fermi level can be found and should have a kinetic energy comparable to the He I α photon energy. This can again be fit by three lines, with the midpoint of the center line segment as E_F . For non-degenerately doped materials the density of states at the Fermi level is zero or close to zero, so this signal may not appear. In this case a conductive material on the same sample holder is used as calibration.

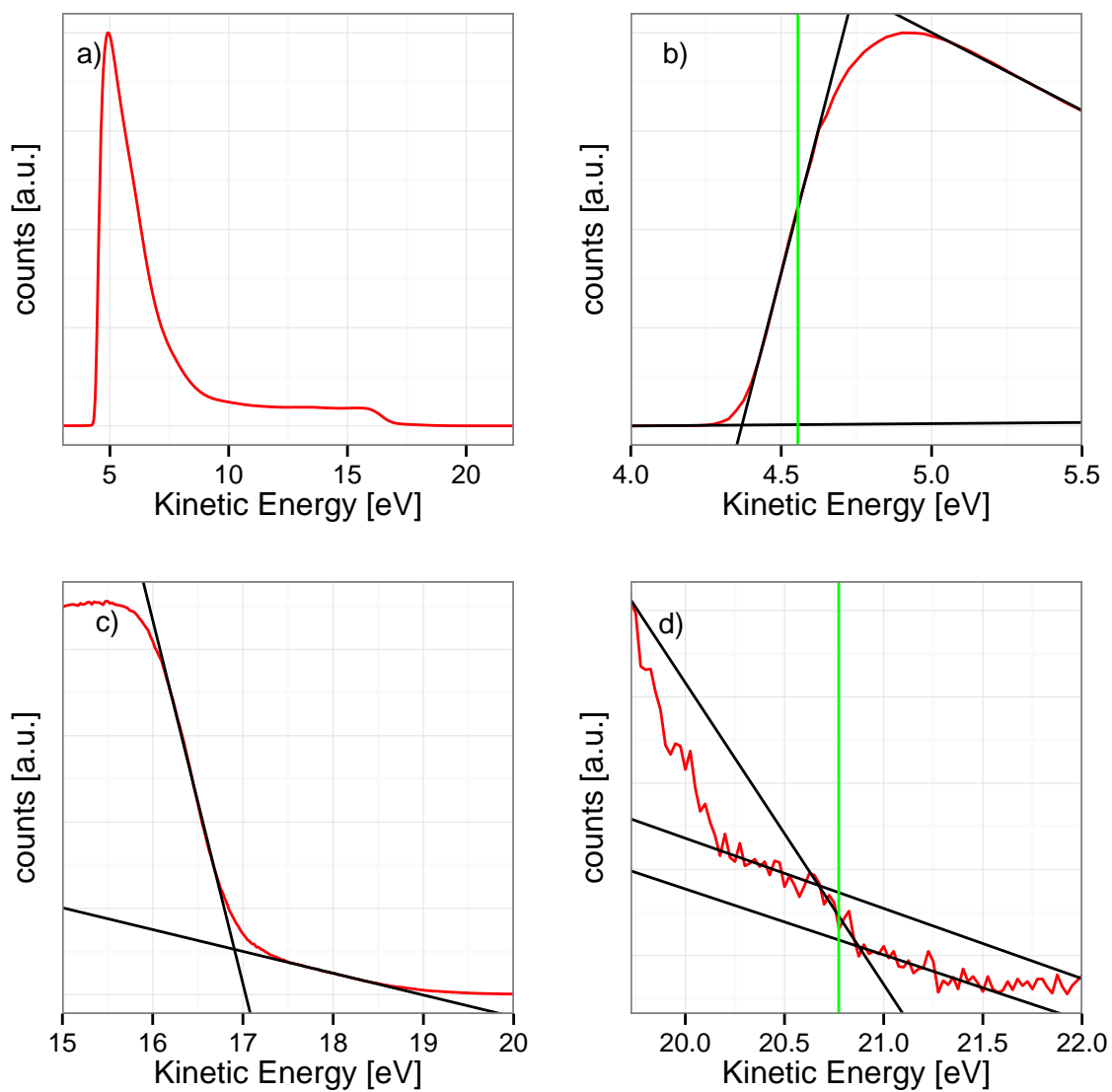


FIGURE A.3. a) The spectrum is calibrated to kinetic energy scale, and b) the secondary electron cutoff value, c) the valence band maximum, and d) the Fermi level are fit.